Title
Ceramic Composites in Extreme Environments: Experimentation and Modeling

Author
Angle, Jesse Philip

Publication Date
2014

Peer reviewed|Thesis/dissertation

UNIVERSITY OF CALIFORNIA,
IRVINE

Ceramic Composites in Extreme Environments: Experimentation and Modeling

DISSERTATION

submitted in partial satisfaction of the requirements
for the degree of

DOCTOR OF PHILOSOPHY

in Materials Science and Engineering

by

Jesse Philip Angle

Dissertation Committee:
Professor Martha L. Mecartney, Chair
Professor Daniel R. Mumm
Professor Timothy J. Rupert

2014

Dedication

To my parents,

For their encouragement and support.

And to my loving Seema,

For her endless insistence that I can
achieve anything I set my mind to.

And for correcting all of my bad speeling!!

Table of Contents

List of Figures

List of Tables

Acknowledgements

First and foremost, I would like to express my very great appreciation to Professor Martha Mecartney for her patient guidance, enthusiastic encouragement, and useful critiques of this research work. I've learned far more from her than words can express and will be forever indebted to her for the outstanding advisement she has given me over the years, and the years to come.

Special thanks should be given to Professor Daniel Mumm for his mentoring and assistance in making me the researcher I am, as well as Professor Timothy Rupert for his helpful comments and suggestions on my dissertation work.

My deepest gratitude goes to the great Dr. Peter E. D. Morgan. His impassioned discussions on the philosophy of science have provided me with a unique perspective on research, one that I will carry with me throughout my career.

To Dr. Chris Hoo, my first mentor, who has served as an inspiration to me over the past six years. None of this would have been possible without him. Thank you for everything, Chris.

Special thanks to my colleagues on the front lines in the Mecartney research group: Mai Ng, Chris Hoo, Danju Men, Jung-Yun Kim, Weicai Cao, Kenta Ohtaki, Kara Phillips, Austin Travis and Neshat Heravi; and in the Mumm research group: Anh Duong, Matt Weeks, Chuan Zheng, Matt Sullivan, Joe Horwath, Jessica Witt and Vineet Nair.

A grateful thank you to my army of undergrads for all their hard work: Marvin Chan, Kyle Dykman, Armando Perez-Selsky, Juan Lucio-Vega, Lucia Diaz, Pedro Cruz, Danielle Becerra, Merna Salama, Rochelle Parker, Patrick Ngo and Rea Reyes – now GET BACK TO WORK!

Thank you to the ChEMS department staff, Yi-San Chang-Yen, Beatrice Mei, Grace Chau, Janine Le, and Steve Weinstock for their outstanding work; and to our department Chair Albert Yee for his leadership and support.

I would also like to acknowledge my research collaborators: Dr. James Steppan and Patrick Thompson from EmiSense Technologies, Dr. Zhaojie Wang from the University of California, Riverside, Dr. Chris Dames from University of California, Berkeley, and Andrew T. Nelson from Los Alamos National Laboratory. Through their contributions, I've learned the value and enjoyment of scientific collaboration.

Lastly, thank you to the National Science Foundation and the Japan Society for the Promotion of Science for giving me the chance to live and work in Tokyo for the summer, and to learn from the extraordinary research group of Professor Yuichi Ikuhara at the University of Tokyo.

Curriculum Vitae

Jesse Philip Angle

EDUCATION

University of California, Irvine

Ph.D.	Materials Science and Engineering	2014
M.S.	Materials Science and Engineering	2010
B.S.	Mathematics Specialization in Applied and Computational Mathematics Minor: Materials Science and Engineering	2009

RESEARCH EXPERIENCE

University of Illinois, Urbana-Champaign, Urbana, IL Nov 2014 – Present
Postdoctoral Research Associate
Research Advisor: Professor Jessica A. Krogstad

University of California, Irvine, Irvine, CA Sept 2009 – Jun 2014
Graduate Student Researcher
Dissertation Advisor: Professor Martha L. Mecartney
Dissertation Title: *Ceramic Composites in Extreme Environments: Experimentation and Modeling*

University of Tokyo, Tokyo, Japan Jun 2013 – Aug 2013
National Science Foundation EAPSI Research Fellow
Research Advisor: Professor Yuichi Ikuhara

University of California, Irvine, Irvine, CA
Undergraduate Student Researcher
Advisor: Professor Martha L. Mecartney Sept 2008 – Jun 2009
Advisor: Professor Shuwang Li Sept 2007 – Jun 2008

PUBLICATIONS

Journal Article, Peer Reviewed
Angle J.P., Travis A.W., Lin Q., and Mecartney M.L. "Structural Analysis of CeMgAl11O19 (Magnetoplumbite)," (In preparation)

Angle J.P., Nelson A.T., Men D. and Mecartney M.L., "Thermal Measurements and Computational Simulations of Three-Phase (CeO2 - MgAl2O4 - CeMgAl11O19) and Four-Phase (3Y-TZP - Al2O3 - MgAl2O4 - LaPO4) Composites for Inert Matrix Nuclear Fuels," (In review - J. Nucl. Mater.)

Angle J.P., Steppan J.J., Thompson P.M. and Mecartney M.L., "Parameters Influencing Thermal Shock Resistance and Ionic Conductivity of 8 mol% Yttria-stabilized Zirconia (8YSZ) with Dispersed Second Phases of Alumina or Mullite," (In review - J. Eur. Ceram. Soc.)

Angle J.P., Morgan P.E.D. and Mecartney M.L., "Water Vapor Enhanced Diffusion in Alumina," *J. Am. Ceram. Soc.*, **96** {11} 3372–3374 (2013)

Angle J.P., Wang Z., Dames C. and Mecartney M.L., "Comparison of two-phase thermal conductivity models with experiments on dilute ceramic composites," *J. Am. Ceram. Soc.*, **96** {9} 2935–2942 (2013)

Conference Proceedings

Moodie A.L.R., **Angle J.P.**, Tackett E.C., Rupert T.J., Mecartney M.L. and Valdevit L., "Ceramic and hybrid micro-architected materials for high temperature applications," *Society for the Advancement of Material and Process Engineering (SAMPE)* Proceedings 2013, (2013)

Other Publications

Angle J.P., "Japan research experience—A study in science and attitude," *American Ceramic Society Bulletin*, June/July 2014 – Vol. 93 No. 5

PRESENTATIONS

Podium Presentations

Angle J.P., Morgan P.E.D. and Mecartney M.L., "Enhanced Diffusion of Oxygen in Alumina Exposed to Water Vapor", 38th International Conference & Exposition on Advanced Ceramics & Composites, Daytona Beach, Florida, January 2014.

Angle J.P., Selama M.E., Morgan P.E.D. and Mecartney M.L., "Synthesis and Characterization of $LaCrAl_{11}O_{19}$ (Magnetoplumbite)", 2013 American Institute of Chemical Engineers Annual Meeting, San Francisco 2013, California, November 2013.

Angle J.P., Selama M.E., Morgan P.E.D. and Mecartney M.L., "Synthesis and Characterization of $LaCrAl_{11}O_{19}$ (Magnetoplumbite)", Materials Science & Technology Conference & Exhibition, Montreal 2013, Quebec, Canada, October 2013.

Angle J.P., Morgan P.E.D. and Mecartney M.L., "Novel Approaches to Make Sr-Doped $LaPO_4$ (Monazite) for Proton Conductivity", Materials Science & Technology Conference & Exhibition, Pittsburgh, Pennsylvania, October 2012.

Angle J.P., Wang Z., Chan M.M., Dames C. and Mecartney M.L., "Thermal Shock, Microstructure, Ionic Conductivity, and OOF2 Modeling of 8YSZ", 36th International Conference & Exposition on Advanced Ceramics & Composites, Daytona Beach, Florida, January 2012.

Angle J.P., Ng M., Morgan P.E.D. and M.L. Mecartney, "Sr-Doped $LaPO_4$ (Monazite) for Proton Conductivity", 36th International Conference & Exposition on Advanced Ceramics & Composites, Daytona Beach, Florida, January 2012.

Angle J.P. and Mecartney M.L., "Thermal Shock Resistance of Yttria-Stabilized Zirconia with Second Phases", 35th International Conference & Exposition on Advanced Ceramics & Composites, Daytona Beach, Florida, January 2011.

Poster Presentations

Angle J.P., Morgan P.E.D. and Mecartney M.L., "Proton Assisted Diffusion in Oxides (Does Steam Damage Ceramics?)", Southern California Society for Microscopy and Microanalysis (SCSMM) Symposium, Irvine, California, February 2014.

Angle J.P., Morgan P.E.D. and Mecartney M.L., "Proton Assisted Diffusion in Oxides (Does Steam Damage Ceramics?)", 38th International Conference & Exposition on Advanced Ceramics & Composites, Daytona Beach, Florida, January 2014.

Angle J.P., Tochigi E., Hoo C.M., Ikuhara Y. and Mecartney M.L., "In-situ Transmission Electron Microscopy Indentation to Characterize Deformation in Ceramics", Japan Society for the Promotion of Science Summer Program 2013, The Graduate University for Advanced Studies (Sokendai), Japan, June 2013.

Angle J.P., Men D., Nelson A.T. and Mecartney M.L., "Thermal Measurements of 3- and 4-Phase Ceramic Composites using OOF2 Analysis", Gordon Research Conference on Solid State Studies in Ceramics, South Hadley, Massachusetts, August 2012.

Angle J.P., Men D., Nelson A.T. and Mecartney M.L., "Thermal Measurements of 3- and 4-Phase Ceramic Composites using OOF2 Analysis", International Congress on Ceramics, Chicago, Illinois, July 2012.

Angle J.P. and Mecartney M.L., "Thermal Shock Resistance of Yttria-Stabilized Zirconia with Second Phases", Gordon Research Conference on Solid State Studies in Ceramics, New London, New Hampshire, August 2010.

Angle J.P., Hoo C.M. and Mecartney M.L., "A Comparison of Conventional and Reactive Sintering in the Formation of Three-Phase Polycrystalline Ceramic Composites," Undergraduate Research Symposium, Irvine, California, May 2009.

AWARDS AND GRANTS

Second Place, Poster Competition, SCSMM,	2014
American Ceramics Society Graduate Excellence in Materials Science	2013
UC Irvine Associated Graduate Students Travel Grant (**$600**)	2013
UC Irvine Fletcher Jones Fellowship (**$18,800**)	2013 – 2014
National Science Foundation East Asia and Pacific Summer Institutes (NSF EAPSI) for U.S. Graduate Students Fellowship (**$12,000**)	2013
Third Place, Poster Competition, Materials Science & Technology Conference	2012
Gordon Research Conference Student Travel Award (**$500**)	2010, 2012
National Science Foundation Student Scholar Travel Grant (**$600**)	2012
Graduate Assistantship in Areas of National Need Fellowship (**$18,000**)	2010 – 2013
UC Irvine Center for Opportunities and Diversity in Engineering Fellowship (**$21,500**)	2009 – 2010
National Science and Mathematics to Retain Talent (SMART) Grant (**$4,000**)	2008 – 2009
UC Irvine Academic Scholarship (**$10,400**)	2008 – 2009
Deans Honor List	2008, 2009

JOURNAL REVIEWER

Journal of the American Ceramics Society

PROFESSIONAL AFFILIATIONS

American Ceramics Society
Materials Research Society
ASM International
American Institute of Chemical Engineers
Microscopy Society of America

ACADEMIC SERVICE AND OUTREACH

Graduate Student Representative, UC Irvine Graduate Studies Committee	2013 – 2014
Student Representative, American Ceramics Society, AACS Division	2013 – 2014
Student Delegate, American Ceramics Society President's Council of Student Advisors (PCSA)	2012 – 2014
Present and Founder, Materials Research Society UC Irvine Student Chapter	2012 – 2014
Representative, Environmental Health and Safety - Safety On Site	2010 – 2014
President, Chemical Engineering and Materials Science Graduate Student Association	2010 – 2012
Peer Mentor, Graduate InterConnect Peer Mentor Program	2011 – 2012
Tutor, Center for Opportunities and Diversity in Engineering Program	2009 – 2010

TEACHING AND MENTORING EXPERIENCE

University of California, Irvine, Irvine, CA
Teaching Assistant, Department of Chemical Engineering and Materials Science

- Introduction to Materials Science and Engineering — Winter 2012, Summer 2012
- Advanced Laboratory in Chemistry and Synthesis of Materials — Spring 2010

Santiago Canyon College, Orange, CA
Instructional Assistant, Department of Mathematics — Sept 2006 – Jun 2013

University of California, Irvine, Irvine, CA
Graduate Student Mentor — May 2010 – Jun 2014

- 11 undergraduate student researchers (5 have matriculated to graduate school)
- 8 graduate student researchers (3 M.S. & 7 Ph.D.)

INDUSTRY EXPERIENCE

Nanovea, Irvine, CA June 2009 – Oct 2009
Laboratory Technician

EmiSense Technologies, Irvine, CA Nov 2009 – Jun 2010
Research Assistant

TECHNICAL SKILLS

Characterization: Optical microscopy, Scanning electron microscopy (SEM), Focused ion beam (FIB), Transmission electron microscopy (TEM), X-ray diffraction (XRD), High temperature x-ray diffraction (HTXRD), Atomic force microscopy (AFM), Raman spectroscopy, Atomic absorption (AA) spectroscopy, Electrochemical impedance spectroscopy (EIS), Differential scanning calorimetry (DSC), Thermogravimetric analysis (TGA), Dynamic light scattering (DLS), Physical vapor deposition (PVD), Hardness testing, Fracture toughness testing, Tensile/compression/3-point testing.

Computers: Windows OS, Mac OS, Linux OS, Microsoft Office, Adobe Creative Studios, MATLAB, SolidWorks, ImageJ, CrystalMaker, ZView, OOF2, LabVIEW/NI hardware, HTML.

Ceramic Processing: Ball milling, Attrition milling, Cold isostatic press (CIP), High temperature furnaces, Mass flow systems, Slow speed saws, SEM/TEM sample preparation, Ion beam sputtering, Slip casting, Sol-gel process, Rotary evaporation.

Abstract of the Dissertation

Ceramic Composites in Extreme Environments: Experimentation and Modeling

By

Jesse Philip Angle

Doctor of Philosophy in Materials Science and Engineering

University of California, Irvine, 2014

Professor Martha L. Mecartney, Chair

Advanced ceramic materials are used in many fields of the technology sector. Ceramics are ideal materials for applications in extreme environments where stability under high temperatures, resistance to corrosion, and good mechanical strength are required. Ceramic composites offer novel solutions to circumvent issues and drawbacks seen in traditional single-phase materials by taking advantage of the unique properties offered by each constituent phase. A synergistic combination of properties and microstructural and morphological characteristics offer the potential for application specific tailoring, and expand the usefulness of the material by broadening its application spectrum. The goal of this research is to explore the use of ceramic composite systems for traditional single-phase components found in solid-state oxygen sensors and nuclear fuel. In both applications, ceramic-based components operate at elevated temperatures, are subjected to extreme thermal gradients, and can have compromised mechanical integrity due to the buildup of thermal stresses. These challenges may be significantly alleviated using a ceramic composite approach, where each constituent has its own unique morphology and attributes. Experimental and computational models are used in tandem in order to investigate the potential for advanced ceramic composite systems for applications in oxygen sensors and nuclear fuel. Lastly, the effect of water vapor in the high temperature environment is also evaluated.

Chapter 1: Introduction

1.1 Ceramic Composites

Ceramic materials have come a long way from their traditional use as clay pots and porcelain bathtubs. Revolutionary advances in the technology sector have been made possible by advanced ceramic materials, with applications in medicine (e.g. artificial bone and biodegradable splints), aerospace engineering (e.g. space shuttle tiles, combustion liners, and turbine blade coatings), and the electronics industry (e.g. high dielectric capacitors and integrated circuit packages). It has long been recognized that ceramics offer a unique set of properties compared to other materials like metals and polymers. These properties include: high melting points, high fracture toughness, and low electrical conductivity [1], which make ceramics the ideal material for applications in extreme environments where stability under high temperatures, resistance to corrosion, and good mechanical strength are required.

Typically subjected to extreme thermal environments, ceramic materials tend to experience increased susceptibility to fracture and failure as operating temperatures increase [2]. An example of this may be illustrated with zirconia based oxygen sensors, which are found in the exhaust steam of automobiles and operate at > 1173 K (900°C). Water droplets from exhaust gases can cause thermal shock and failure of the sensor [3], triggering the check engine light and requiring the vehicle's owner to replace the component. One potential solution to problems such as these is to improve the intrinsic properties of the ceramic components used in these systems by incorporating composite materials.

Ceramic composites offer a novel approach to circumvent major issues associated with traditional single phase materials by taking advantage of the unique properties offered by each constituent phase. The combination of the properties allow for significant modification of

microstructural and morphological characteristics, offer the potential for application specific tailoring, and expand the usefulness of the composite by broadening its application spectrum. Composite systems have already demonstrated their potential to improve material properties such as toughness and hardness [4-9], tensile strength [10-11], flexural strength and thermal shock resistance [11-15], creep and superplasticity [16-22], electrochemical properties [23-30] and thermal conductivity [3; 31-33]. With constantly increasing standards for improved quality and performance under extreme environments, ceramic composites make excellent candidates for the next generation of advanced materials.

Many of the ceramic composite systems already in use are based around the matrix-particulate model wherein dispersed ceramic particles, often referred to as fibers or whiskers, are housed within a continuous ceramic matrix phase. These ceramic matrix composite systems have been heavily studied [10-11; 34-35] and are still considered at the forefront of ceramic technology. An alternative approach to the ceramic matrix composites design is to incorporate a dense monolithic phase as each constituent, where each phase has its own unique morphology and grain structure.

Solid-state oxygen sensors and nuclear fuel rods are two potential applications where multiphase ceramic composites could outperform a traditional single phase component.. Although these applications are vastly different from one another, the ceramic materials and operating conditions they employ are very similar. Both use a single phase ceramic material with the fluorite structure (ZrO_2 in solid-state oxygen sensors and UO_2 in nuclear fuel). Additionally, both applications require elevated operating temperatures, >1073 K (800°C), and are subjected to extreme thermal gradients. A multiphase ceramic composite approach has been explored to

alleviate some of the problems associated with these applications, and is discussed in further detail below.

Ceramic composites may also play a role as testing platforms for the study of basic science-type phenomenon. For example, ceramic/metal composite systems have previously been used to study the influence of dopants such as Y^{3+} along Al_2O_3 grain boundaries [36]. A dense Al_2O_3 – Ni composite takes advantage of the reaction between Ni and Al_2O_3 to form $NiAl_2O_4$, which may be used as a maker for oxygen diffusion. This innovative ceramic/metal composite technique may be used to study the effects that different environments have on the grain boundary diffusion of oxygen, and is discussed in further detail below.

1.2 2-Phase Ceramic Composites for Solid-State Oxygen Sensors

The lifetime of solid-state oxygen sensors used for automotive applications is dramatically reduced when water from the exhaust steam comes in contact with the sensor's housing. A temperature gradient is imposed on the sensors, causing the outer region to become cooler while the inner region remains at an elevated temperature. This difference in temperature across the sensor produces a non-uniform thermal expansion of the ceramic electrolyte, ZrO_2, and creates internal cracks in areas of high stress concentration. Operation at temperatures exceeding 1173 K (900°C) can cause this interaction to result in the thermal shock of the oxygen sensor, which may lead to degradation in the mechanical strength and eventual failure of the sensor. This phenomenon is the most common failure mechanism found in these sensors. Improvement to the thermal shock resistance of the ceramic based electrolyte is believed to extend the performance, lifetime, and reliability of these sensors by reducing failure caused by thermal stresses.

A 2-phase ceramic composite with ZrO_2 as the majority phase (80 or 90 vol%), and Al_2O_3 or $3Al_2O_3{\cdot}2SiO_2$ as the minor phase is being explored to design an electrolyte with higher thermal shock resistance. Both Al_2O_3 and $3Al_2O_3{\cdot}2SiO_2$ can provide the ZrO_2 electrolyte with increased strength and thermal conductivity. These two material properties are necessary to enhance the electrolyte's ability to withstand the large thermal gradients that lead to thermal shock. Additionally, computational modeling of the ceramic composite will enable the evaluation of the heat flow profiles produced by the multiphase systems, as well as the ability to determine how adjustments to the microstructure can improve thermal transport. A combined experimental and computational approach will be employed to further study how the addition of second phases affect the thermal shock resistance of solid-state oxygen sensors.

1.3 3-Phase and 4-Phase Ceramic Composites for Nuclear Fuel

The low thermal conductivity of conventional nuclear fuel (i.e. enriched UO_2) causes high central temperatures, which may lead to the melting and cracking of the fuel bundle [37]. Additionally, UO_2 undergoes microstructural evolution as a result of radiation-induced defects and the accumulation and migration of fission products [38]. This accumulation of fission products within the dense fuel bundle induces swelling, which damages the surrounding fuel cladding. An innovative fuel design concept has been proposed that employs a composite fuel featuring a fissile phase (enriched UO_2) and additional inert phases [39]. These inert phases can offer (a) increased thermal conductivity; (b) accommodation of fission byproducts while they are being created; and (c) decreased structural degradation via the use of alternative interfaces as efficient sinks for point defects [40]. Inert matrix multiphase ceramic composite fuels have the potential for higher efficiency, longer service lifetimes (i.e. higher burn-up) and increased accident tolerance in future nuclear reactors. The most significant benefits to a ceramic composite fuel design will be: an increase in thermal conductivity, and the accommodation of fissile products. The incorporation of inert (non-fissile) ceramic phases with high thermal conductivity for improved thermal transport as well as multi-cation oxides with "open" crystal lattices for the uptake of fissile products, is necessary for an advanced fuel design.

A natural first step in the design of a composite fuel is the development of a computational materials screening tool to allow for the testing of many different "candidate materials." This allows for a strategic selection of inert phases without the need for sample fabrication. The thermal conductivity as a function of material selection and phase fraction can be modeled using object-oriented finite element analysis. This approach may take grain structure and morphology into consideration, as well as the thermal properties of UO_2.

1.4 A Ceramic/Metal Composite as a Test Platform for Determining the Grain Boundary Diffusion of $(OH)^-$

A range of effects has been observed in ceramic materials exposed to water vapor at high temperatures. Some of these effects include: accelerated reaction kinetics [41-42], increased coarsening and grain growth [43-45], faster sintering and densification [46-49], and enhanced creep rates [50]. Absorbed H_2O in the vapor phase can easily react with an oxide surface and form (OH)-, which can then react with the highly energized grain boundary of the ceramic and diffuse inward. It has been proposed that a proton from the (OH)- group can hop (or tunnel) from one oxygen to another. If the oxygen is blocked, the proton can hop/tunnel to another mobile oxygen. This phenomenon is illustrated in Figure 1.1.

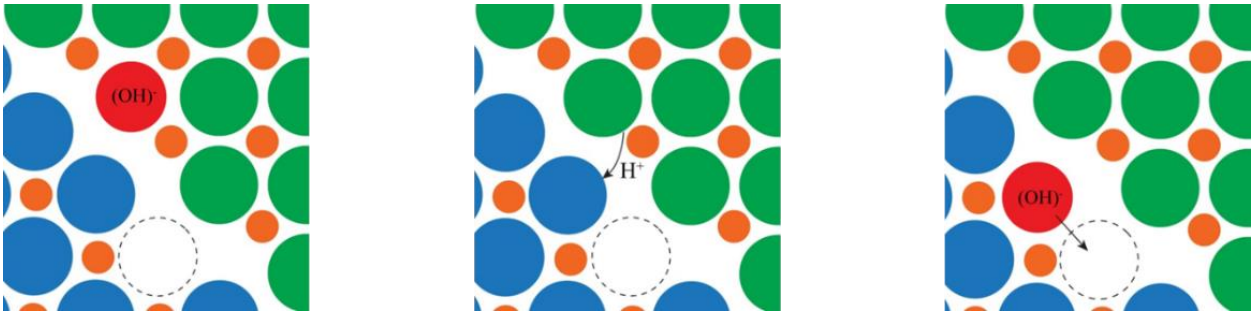

Figure 1.1 Proton hoping/tunneling at an oxide grain boundary.

Perhaps slightly counterintuitive is that the size of an (O^{2-}) anion in an oxide lattice shrinks by approximately 30% [51] when forming (OH)-, as shown in Figure 1.2. Additionally, this incorporated proton moves within the p-orbital of the oxygen ion, giving the (OH)- the ability to be more easily polarized [52]. It has been hypothesized in this work that because the (OH)- ions are smaller and more polarizable than the O^{2-}, this could lead to faster grain boundary diffusion of oxygen as (OH)- in oxide type ceramics.

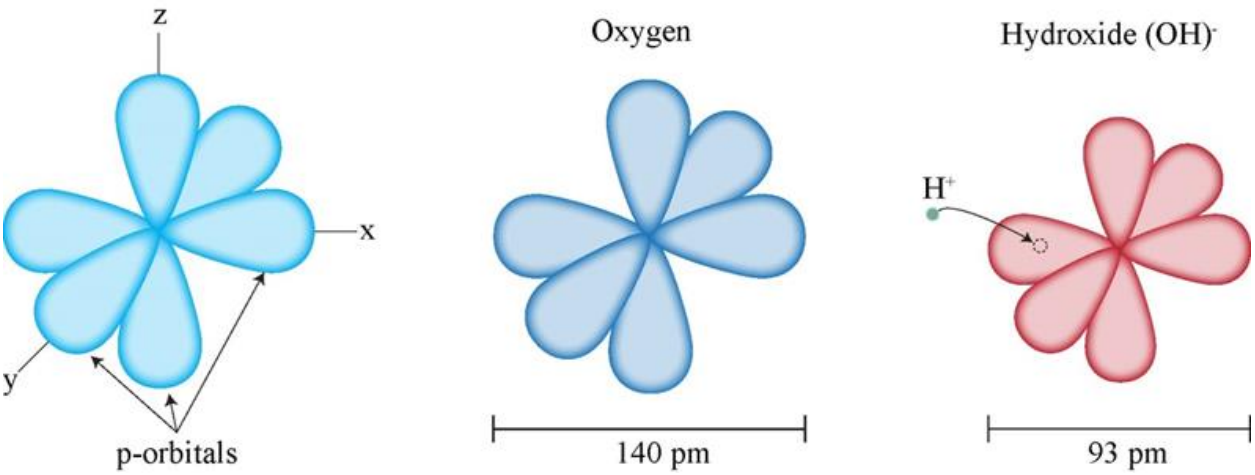

Figure 1.2 Relative size of oxygen and hydroxide ion.

The grain boundary transport of oxygen and the influence of dopants such as Y^{3+} along Al_2O_3 grain boundaries have been studied through the use of innovative ceramic composite techniques [36; 53]. Ni-particles located at the grain-boundaries of Al_2O_3 experience an oxidizing environment through the grain-boundary diffusion of oxygen ions. This in-diffusion of oxygen, in either O^{2-} or $(OH)^-$ form, can be measured by observing the formation of $NiAl_2O_4$, as outlined in Figure 1.3. A ceramic/metal composite system such as this can be used as a tool to study the reaction kinetics and activation energies associated with oxygen diffusion

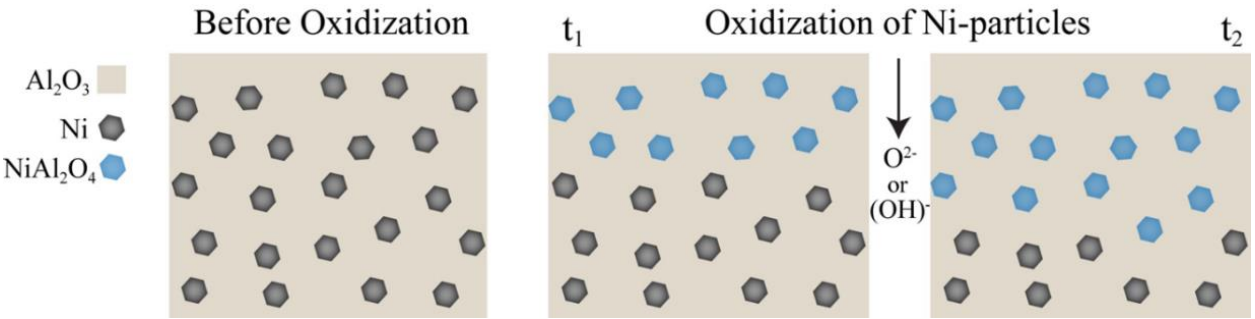

Figure 1.3 Schematic of oxygen diffusion from the free surface of the Al_2O_3 and oxidation of Ni to $NiAl_2O_4$, viewed as a cross-sectional slice.

Chapter 2: Experimental Procedures

2.1 Materials Processing

A multitude of ceramic powders were used in the fabrication of the composite systems studied herein. The selection of each starting powder was based on their specific thermal, electrical, mechanical or crystallographic properties, or a combination of properties. The selection methodologies for each composite system are discussed in more detail in later chapters. Table 2.1 lists the powders obtained from commercial vendors with the exception of $LaPO_4$, which was synthesized in the lab. In some cases, a combination of powders was added in specific ratios for the purpose of forming a new phase in-situ. An example of this is the formation of $CeMgAl_{11}O_{19}$ from CeO_2 and $MgAl_2O_4$ starting powders.

Table 2.1 Crystalline ceramic powders

Starting Powder	Vendor	Starting Particle Size (nm)	Crystal Structure
Alumina (α-Al_2O_3)	Baikowski	600 nm	Hexagonal
8 mol% Yttria-Stabilized Zirconia (8YSZ)	Tosoh	50 nm	Cubic
Mullite ($3Al_2O_3$•$2SiO_2$)	KCM Corp.	800 nm	Orthorhombic
Mg-Spinel ($MgAl_2O_4$)	Baikowski	200 nm	Cubic
CeO_2	Sigma-Aldrich	50 nm	Cubic
3Y-TZP	Tosoh	50 nm	Tetragonal
NiO	Alfar Aesar	200 nm	Cubic
Monazite ($LaPO_4$)	Lab Made [54]	200-400 nm	Monoclinic

Once the composition of a composite was determined and the starting powders weighted out, the powders were milled using a Union Process attritor mill. Typical milling slurry consisted of the starting powder mixture, 5 mm diameter zirconia media (Tosoh) or 5 mm diameter alumina media (Union Process), and isopropyl alcohol as a milling dispersant. A ratio of 1.3 L of slurry to 1.0 kg of media was used, keeping the total starting powder weight constant at 40g. Milling time ranged between 8 to 24 hours. After milling, slurries were separated from the media, dried using a hot plate at 120°C, and sieved into a fine powder with an average agglomerate size of < 80 um.

Processed powder was packed in silicon molds that were made in house, and then cold isostatically pressed (CIP) at 380MPa for 5-10 minutes. These pressed samples are referred to as "green bodies" or "green compacts" since they are still in a pre-sintered or natural state. A pristine green body will have a right cylinder geometry, allowing for an approximate green body density to be determined using the equations:

$$V_{rc}=\pi r^2 h \tag{2.1}$$

$$\rho_{gb}=\frac{M_{gb}}{V_{rc}} \tag{2.2}$$

where (r) is the radius of the cylinder, (h) is the height of the cylinder, (V_{rc}) is the right cylinder volume, (M_{gb}) is the green body mass and (ρ_{gb}) is the green body density. Typical relative green body densities range between 50-60% dense (calculations for relative densities are discussed in section 2.2.1) indicating the CIPing process is capable of taking loose power from an effective relative density of 0% to as high as 60%. This highly efficient powder compaction allows for the next phase in the process, the sintering phase, to increase the relative density into the 90-99% dense range.

Conventional sintering of green compacts took place in a high temperature bottom loading box furnace outfitted with resistive heating moly disilicide ($MoSi_2$) heating elements and controlled by a PID regulated Eurotherm 2406 controller. The green body specimens were first placed in alumina crucibles, and then covered with a small amount of loosely packed powder, known as a sintering bed, before being loaded into the furnace. Sintering ramp rates, hold times (also known as dwell times), and hold temperatures varied depending on the composition being studied. A typical sintering profile is depicted in Fig 2.1 where a one step, ramp up – hold – ramp down was used.

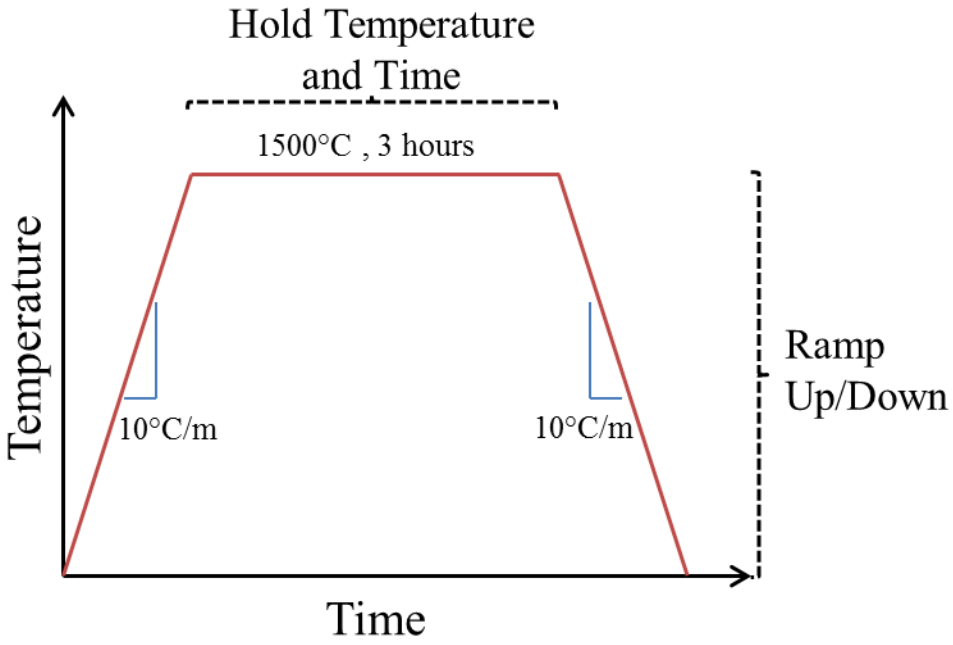

Figure 2.1 Sintering Profile for one-step process.

Other forms of sintering, such as sintering in different environments or using multi-step profiles, were used in specific experiments and are discussed in later chapters. Additionally, a range of sample geometries was explored to better assist the examination of material properties and to allow for more accurate materials characterization.

2.2 Materials Characterization

2.2.1 Density Measurements

The Archimedes displacement method was used to determine density. This classic method involves weighing the specimen in air (dry weight, M_{dry}) followed by submerging the specimen in water and measuring its weight (wet weight, M_{wet}). This method is founded on the principle that a sample submerged in a liquid of lower density will lead to a displacement of the liquid equal to the volume of the sample. The weight of the submerged sample is reduced by a buoyant force imposed on the sample by the volume displacement. From the Archimedes principle, the density of the sample can be determined using the relationship:

$$\rho_{solid}=\rho_{liquid}\frac{M_{dry}}{M_{dry}-M_{wet}} \tag{2.3}$$

where (ρ_{liquid}) is the density of pure water and is always assumed to be 1 g/cm^3, and (ρ_{solid}) is the bulk density of the sample.

To determine the relative density for a composite system, the theoretical density of each component must first be known in order to approximate the theoretical composite density. Table 2.2 gives the theoretical density of the starting ceramic materials discussed in Section 2.1.

Table 2.2 Theoretical densities

Starting Powder	Density (g/cm^3)	Reference*
Alumina (α-Al_2O_3)	3.984	[55]
8 mol% Yttria-Stabilized Zirconia (8YSZ)	5.959	JCPDS no. 30-1468
Mullite ($3Al_2O_3$•$2SiO_2$)	3.171	JCPDS no. 15-0776
Mg-Spinel ($MgAl_2O_4$)	3.579	JCPDS no. 21-1152
CeO_2	7.215	JCPDS no. 34-0394
3Y-TZP	6.242	JCPDS no. 60-0503
NiO	6.808	JCPDS no. 47-1049
Monazite ($LaPO_4$)	5.111	JCPDS no. 84-0600

*Joint Committee on Powder Diffraction Standards (JCPDS)

The density values found in Table 2.2 were used in conjunction with the volume fraction of each component in the composite system in order to determine the theoretical composite density

(ρ_{TCD}) using a simple linear mixing rule. For a two component system, the mixing rule equation is given as:

$$\rho_{TCD}=\rho_1 V_1+\rho_2 V_2 \tag{2.4}$$

where (ρ_1) and (ρ_2) are the theoretical densities found in Table 2.2, and (V_1) and (V_2) are the volume fractions for component 1 and 2 respectively. Using the measured density (ρ_{solid}) calculated from the Archimedes method and the theoretical composite density (ρ_{TCD}) approximated by Eq. 2.4, the relative density of the composite system can be found by the relation:

$$\frac{\rho_{solid}}{\rho_{TCD}}\times 100\% \tag{2.5}$$

Due to the nature of ceramic processing, and the limitations of conventional sintering techniques, a density of 99.0% and above is difficult to achieve. In reality, density values above 95.0% of theoretical values are considered relativity high.

2.2.2 X-Ray Diffraction

Standard x-ray diffraction (XRD) analysis was conducted with a Smart Lab X-ray Diffractometer (Rigaku, Tokyo, Japan), using Cu-kα radiation (wavelength 0.15406 nm) to verify phases and compositions. Scans consisted of 0.05° steps from 5° to 120° using Bragg-Brentano optical configuration. Patterns were indexed using the International Centre for Diffraction Data (ICDD) database. Table 2.2 includes the powder diffraction (PDF) card number for the majority of materials studied. These PDF cards give structural information about the material, along with the angle, peak intensity and diffracted plane (hkl).

2.2.3 Scanning Electron Microscopy

Scanning electron microscopy (SEM) was performed on a FEI Magellan 400 XHR and a FEI XL 30 FEG (FEI, Eindhoven, The Netherlands). An array of detectors was employed to collect information about specific compositions. The commonly used detectors are: secondary electrons (SE), Everhart-Thornley detector (ETD) and through-the-lens detector (TLD), and gather topological and morphological information about the specimen. A concentric backscatter (CBS) detector collected chemical information in the form of phase contrast through the detection of backscatter electrons (BSE). Specific elemental information was collected through the use of energy dispersive spectroscopy (EDS) analysis. To avoid the buildup of electrons on the surface of the specimen, known as sample charging, a thin film of iridium was deposited on the surface using an IBS/e Ion Beam Sputter Deposition System (South Bay Technology, San Clemente, CA).

2.2.4 Grain Size Analysis

Secondary electron images were used to determine the grain structure, or morphology, of the specimen, which then allowed for the grain size to be approximated. Fig. 2.2 shows a SEM micrograph of 8YSZ with the grains outlined. Using Image J (National Institute of Health) imaging software, a pixel length was defined from the SEM image scale bar and an area value was assigned to each grain. An equivalent circle diameter was calculated from the grain area using the following equation:

$$\mathrm{ECD}=\frac{2\sqrt{\mathrm{area}}}{\pi} \tag{2.6}$$

Since the ECD is measured for grain diameters in two dimensions, a multiplication factor of 1.74 (the mathematical relationship between a regular polyhedron and equiaxed grain diameter) was

used in order to obtain a ‘‘true’’ three dimensional grain size [56]. Approximately 400 grains were evaluated for each composition to determine the average grain size.

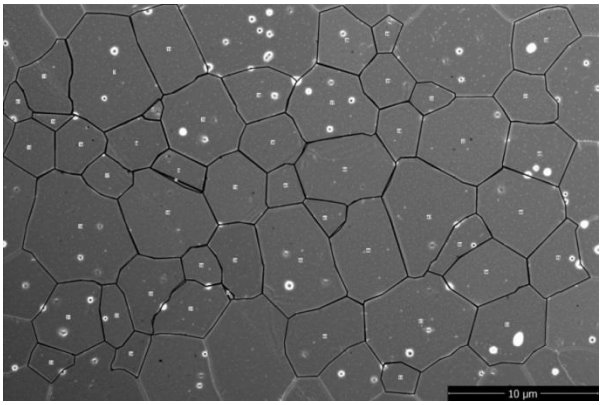

Figure 2.2 SEM image of 8YSZ with grains outlined for grain size analysis.

2.2.5 Transmission Electron Microscopy

Transmission electron microcopy (TEM) was conducted on a 200keV CM20 (FEI/Philips, Eindhoven, Netherlands). Bright field and dark field analysis was performed to obtain phase interface and grain boundary information. A diffraction pattern was used to assist in phase identification by matching zone axis and lattice spacing to known or predicted values.

2.2.6 Focus Ion Beam

Electron transparent specimens were made by focused ion beam (FIB) preparation using a Quanta 3D FEG Dual Beam (FEI, Eindhoven, Netherlands). Specimen preparation began with the deposition of a 2 μm (w) x 10 μm (l) x 3 μm (h) Pt protection pad on the site of interest. Two trenches were milled above and below the site, and a U-shape cut was made before lift-out. A probe was positioned so its tip touched the top of the Pt pad, and a small amount of Pt was used to attach the specimen to the probe. Next, the specimen was detached from the bulk sample and attached to a FIB-TEM copper grid. The specimen was further thinned to ~50-10 nm in thickness before being observed in the TEM.

2.3 Mechanical Behavior Testing

2.3.1 Hardness and Fracture Toughness

Hardness (H_v) and fracture toughness (K_{IC}) tests were conducted using a Zwick Z 3212 (Zwick GmbH, Ulm, Germany) micro hardness tester with a Vickers indenter. Specimens were polished to a 1 μm finish, and an 8 kg load was used to make each indentation. Eight indentations were taken at least 0.5 mm apart as to not influence one another. Hardness and fracture toughness were calculated using Eq. (2.7) and Eq. (2.8) [57], respectively:

$$H_v = 1.854\frac{P}{d^2} \tag{2.7}$$

$$K_{IC} = 0.0937\left(\frac{H_v P}{4r}\right)^{\frac{1}{2}} \tag{2.8}$$

where (H_v) is the Vicker hardness, (P) is the applied load, (d) is the diagonal indentation length, and (r) is the crack length.

2.3.2 3-Point Bend and Thermal Shock Testing

Flexural strength (σ_f) was measured by three-point bend test using a crosshead speed of 0.5 mm/min and a span length of 40 mm. Flexural strength is calculated using:

$$\sigma_f = \frac{3P_f L}{2tw^2} \tag{2.9}$$

where (L) is the span length, (t) is the sample thickness, (w) is the sample width, and (P_f) is the maximum load to fracture. A minimum of 10 samples was tested in ambient conditions to determine the room temperature flexural strength.

To determine the critical temperature difference, samples were held at various testing temperatures for 30 minutes before being quenched, as illustrated in Fig. 2.3. Five samples were tested at each quenching temperature. For each composition, the critical temperature difference

(ΔT_c) can be calculated as the temperature at which a 30% decrease in flexure strength is observed in accordance with ASTM C1525-02 (Determination of Thermal Shock Resistance for Advanced Ceramics by Water Quenching).

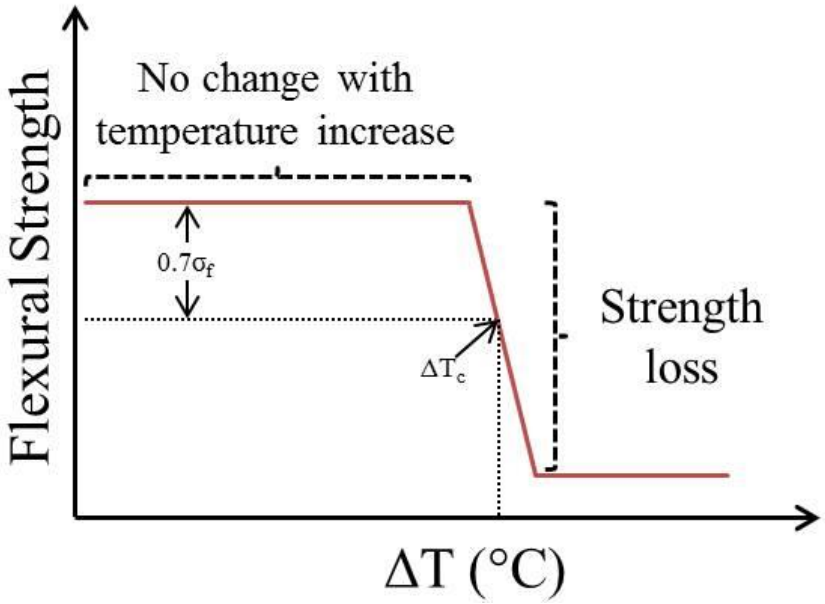

Figure 2.3 Illustration of how the critical temperature difference (ΔT_c) is determined.

2.4 Electrochemical Impedance Spectroscopy

Conductivity measurements were carried out after finishing each face of the specimen with 600-grit silicon carbide paper, applying platinum paste to each face, and firing to create porous platinum electrodes. Impedance spectra were obtained using a HP 4192A LF Impedance Analyzer (Hewlett Packard, Palo Alto, CA) in air, at frequencies over a range of 5 Hz–13 MHz with an applied voltage of 500 mV. A 30 minute dwell at each temperature was used for thermal stability prior to measurement and data collection.

Typical impedance spectra for polycrystalline ceramics consist of three-arcs corresponding to (in order of decreasing frequency or increasing Z) the grain interior, grain boundary, and electrodes; however due to testing limitations, only arcs for the grain interior and grain boundary components were observed. Beyond 823 K (550°C), the two arcs were not well defined and cannot be separated. Resistivities were estimated by determining the interceptions of the arcs and the real axis.

The specific grain boundary conductivity ($\sigma_{S.\ GB}$) is the average conductivity of a grain boundary [58] , and was calculated using:

$$\sigma_{S.\ GB} = \frac{\delta}{d}\sigma_{GB} \tag{2.10}$$

where (δ) is grain boundary width, (d) is grain size and (σ_{GB}) is grain boundary conductivity. This value is more representative than the total grain boundary conductivity, which depends on the concentration of grain boundaries in a material. The effective grain boundary width to grain size ratio (δ/d) can be estimated by the ratio of grain interior capacitance (C_{GI}) to grain boundary capacitance (C_{GB}). Assuming $\varepsilon_{GB} \sim \varepsilon_{GI}$ [59], this ratio may be determined using the following equation:

$$\frac{\delta}{d} = \frac{C_{GI}}{C_{GB}} \frac{\epsilon_{GB}}{\epsilon_{GI}} \tag{2.11}$$

Activation energies for the grain interior and grain boundaries were calculated by analyzing the temperature (T) dependence of the ionic conductivity (σ) using the Arrhenius equation:

$$\sigma = \frac{A}{T} \exp\left(\frac{-Q}{kT}\right) \tag{2.12}$$

where (k) is the Boltzmann constant and (Q) the activation energy.

2.5 Humid Environment Testing

A water vapor rich environment was needed to study to effects of hydroxide ions on the inward diffusion of oxygen. Humidified air was created by flowing ultra-pure zero grade dry air through an air diffuser that was immersed in a flask of pure water housed in a water bath. By adjusting the temperature of the water bath, and using a steam table (Fig. 2.4), the water vapor partial pressure can be held constant. A flow rate of 50-80 sccm was used.

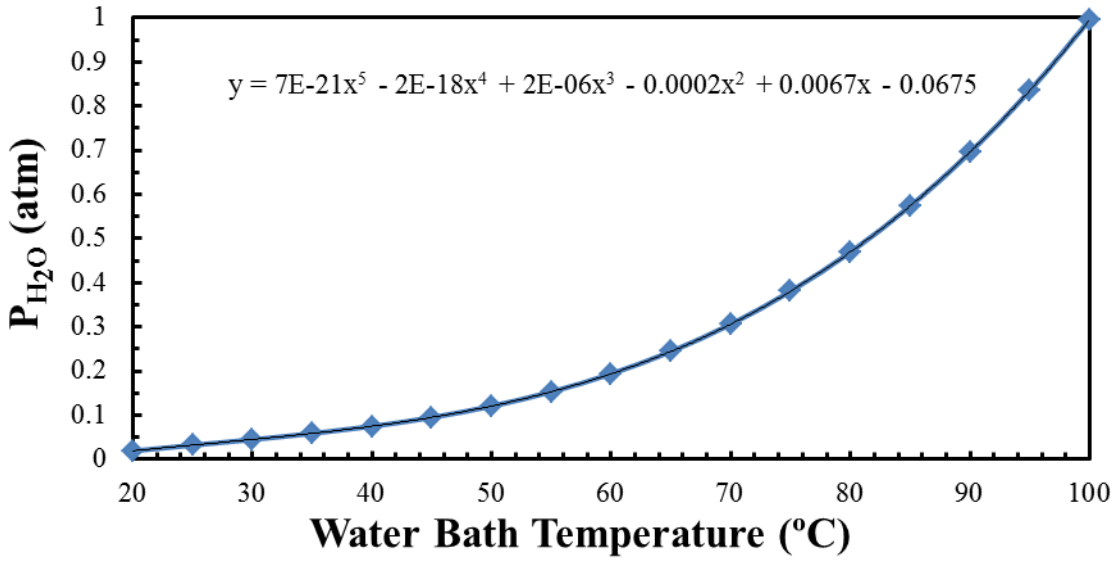

Figure 2.4 Standard steam table with high order polynomial.

The humidified air was then flowed into a sealed tube furnace once the water bath temperature stabilized. A computer controlled valve system was used to prevent inflow of humidified air after furnace operation. Mass flow controllers (MFC) were used to maintain a constant flow rate during furnace operation. Prior to the experiment, the furnace was held at 573 K (300°C). A 3τ residence time was required to flush the system. Fig. 2.5 gives an illustration of the overall testing system.

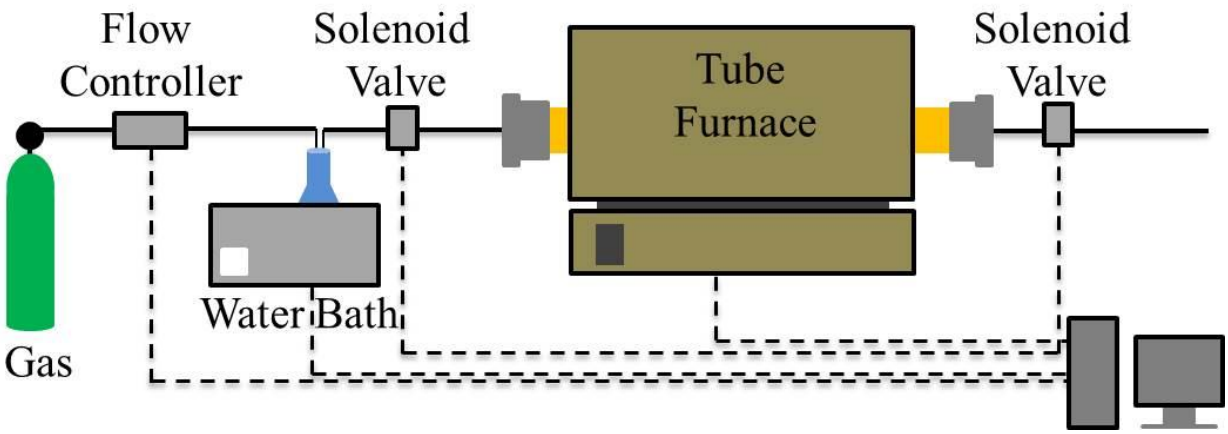

Figure 2.5 Schematic of humid environment flow system.

2.6 Object-Oriented Finite-Element Analysis (OOF2)

Object-oriented finite-element analysis version 2 (OOF2) [60-61], an open access software developed at the National Institute of Standards and Technology (NIST), was used the approximate the thermal conductivity of composites systems. OOF2 uses two-dimensional scanning electron microscopy (SEM) microstructures as the foundation for its calculations. A thermal gradient model was produced using OOF2 for each composition by converting dimensional SEM images to single-color images in post-processing. This enabled the creation of finite-element meshes adapted to the microstructure of the material. Each phase is represented by a single color value and assigned its appropriate material properties. A thermal gradient could be simulated in the vertical direction of the image by assigning the top boundary a fixed temperature value (T_1) and the bottom boundary a temperature value greater than the top (T_2), while keeping the sides adiabatic. Fig. 2.6 gives an illustration of the image parameters used in OOF2.

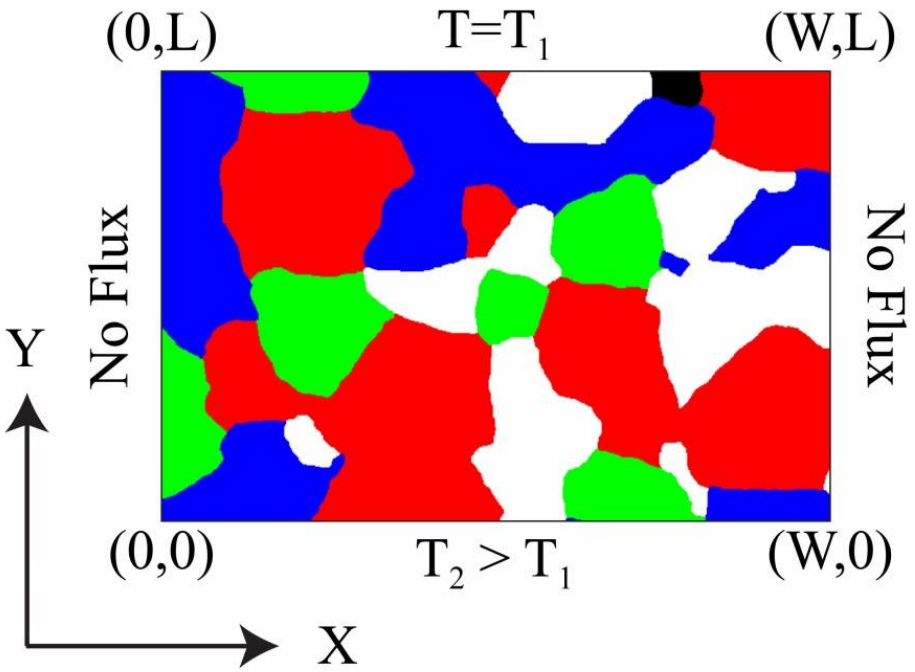

Figure 2.6 Boundary conditions used in OOF2 thermal analysis.

The resulting 2D heat flux is integrated along a boundary of the simulation and used to determine the effective thermal conductivity:

$$k_{eff} = \frac{L_y Q}{L_x\left(T_{bottom} - T_{top}\right)} \tag{2.13}$$

where k_{eff} is the effective thermal conductivity of the composite, Q (watts per meter of thickness in z) is the OOF2 heat flux integrated across the bottom boundary, L_y and L_x are the image dimensions, and T_{bottom} and T_{top} are the temperature values assigned to the bottom and top boundaries, respectively.

Chapter 3: Parameters Influencing Thermal Shock Resistance and Ionic Conductivity of 8 mol% Yttria-stabilized Zirconia (8YSZ) with Dispersed Second Phases of Alumina or Mullite

3.1 Abstract

Improved thermal shock resistance for cubic 8 mol% yttria-stabilized zirconia (8YSZ) used in fuel cells and oxygen sensors can be achieved by the addition of higher thermal conductivity second phases. This work compares 10-20 vol% alumina (α-Al_2O_3) and mullite ($3Al_2O_3 \cdot 2SiO_2$) additions that increase the thermal conductivity, reduce the grain size, and increase the strength and fracture toughness of 8YSZ. Improvements in thermal shock behavior correlate best with increased thermal conductivity. Second phase additions result in a smaller grain size that reduces the ionic conductivity, measured by electrochemical impedance spectroscopy, primarily through the creation of a higher density of blocking grain boundaries. The blocking effect correlates with decreasing grain size in 8YSZ but also is strongly influenced by the wetting behavior and distribution of intergranular phases, as shown in the case of mullite second phase additions. Significantly improved thermal shock resistivity by the addition of an appropriate dilute second phase of higher thermal conductivity, however, may compensate for a slightly lower ionic conductivity in certain applications such as oxygen sensors.

3.2 Introduction

Common applications for cubic 8 mol% yttria-stabilized zirconia (8YSZ) as a solid oxide electrolyte include not only high temperature fuel cells but also oxygen sensors [16; 24; 62-63]. Cubic 8YSZ-based oxygen sensors are present in almost every automobile and used widely in many industries [64]. Failure of the sensor due to thermal shock induced stresses of the electrolyte has been a common operational failure mode and is one of the primary causes for the "check engine" light appearance in automobiles. Exposure to extreme temperature changes such as cooling from water droplets present in exhaust gases, and the rapid heating of the sensor to operational temperatures, render the sensor susceptible to thermal shock, fracture and eventually failure. Failure upon rapid cooling for temperature differences as small as Δ100 K for cubic 6 mol% YSZ [65] and Δ150 K for single phase cubic 8YSZ [66] have been documented. The problem is that 8YSZ has both a low thermal conductivity and a high thermal expansion coefficient (Table 1). When exposed to rapid heating or cooling, extreme temperature gradients develop and the stresses due to thermal expansion can be high enough to initiate crack propagation from preexisting flaws [67].

Table 3.1 Single phase material properties at room temperatures.

	Young's Modulus, E (GPa)	Poisson's Ratio, ν	RT Thermal Conductivity, k (W/m-K)	Expansion Coefficient, α ($\times 10^{-6}$ K^{-1})
8YSZ	220 [68]	0.32 [68]	~2 [69-71]	10.5 [72]
α-Al_2O_3	416 [55]	0.23 [55]	~33[55]	4.6 [55]
Mullite	214 [73]	0.28 [73]	~6 [74]	4.5 [74]

The inclusion of a second phase with a relatively higher thermal conductivity, such as alumina or mullite (Table 3.1), can increase the effective thermal conductivity of a ceramic composite, allowing faster heat transfer from the interior to the exterior during quenching. This in turn reduces the extent of thermal gradients that cause the high thermal expansion stress.

Mullite has a lower thermal conductivity than alumina, but it better matches the elastic modulus and Poisson's ratio of 8YSZ, which may prove to be more beneficial for thermal shock.

There are advantages and disadvantages to adding in a second phase. Small amounts (<1 vol%) of alumina can increase the grain boundary conductivity for impure 8YSZ [25], as alumina helps scavage impurities from the grain boundary region. However, large amounts of alumina can decrease the total conductivity, as shown by Mori et al. [66], who also noted that the second phase of alumina increases thermal shock for 8YSZ. This paper compares the effectiveness of alumina and mullite additions to 8YSZ and presents data regarding mechanical properties, thermal shock resistance and ionic conductivity of the grain interior and grain boundaries as a function of grain size, data not previously reported for this range of materials. Sintering temperatures and times, along with sample preparation procedures were chosen to mimic those used by industry to best represent commercial 8YSZ-based oxygen sensors found in regular use.

3.3 Experimental Procedures

3.3.1 Powder Preparation

Ceramic powders of cubic 8 mol% yttria-stabilized zirconia powder (Tosoh, Tokyo, Japan, starting crystallite size of 30 nm) were combined with either high-purity alumina (α-Al_2O_3) powder (Baikowski Inter. Corp., Charlotte, NC, USA, starting crystallite size of 40 nm), or high-purity mullite ($3Al_2O_3 \cdot 2SiO_2$) powder (KCM Corporation, Tokyo, Japan, starting crystallite size of 40 nm). Appropriate amounts of starting materials were used to make the compositions in Table 3.2. A control sample of 8 mol% YSZ (8YSZ) was also made. Powders were attritor-milled for 8 hours with 5 mm zirconia balls (Tosoh, Tokyo, Japan) in isopropanol, dried overnight at 393 K (120°C), crushed with an agate mortar and pestle, and sieved.

Table 3.2 Composition of composites.

	Volume Fraction of 8YSZ	Volume Fraction of Alumina	Volume Fraction of Mullite
8YSZ+10%A	90	10	-
8YSZ+20%A	80	20	-
8YSZ+10%M	90	-	10
8YSZ+20%M	80	-	20

3.3.2 Sample Fabrication and Characterization

Rectangular green bodies with dimensions 10 mm x 25 mm x 60 mm were fabricated by uniaxially pressing a stainless steel die at 10 MPa for 5 minutes, then vacuum sealing the green body in an air tight bag, and cold isostatically pressing to 380 MPa for 5 minutes. To improve machinability, each green body was bisque fired at 1273 K (1000°C) for 1 hour, then cut using a precision diamond saw into the desired pre-sintered bend bar dimensions. Bars were placed in a rectangular alumina crucible; lightly packed in loose powder, and sintered at 1823 K (1550°C) for 2 hour in air. The resulting samples had the dimensions 3mm (±0.1 mm) x 4 mm (±0.1 mm) x

45 mm (±0.2 mm), in accordance with ASTM C1161-02 (Standard Test Method for Flexural Strength of Advanced Ceramics at Ambient Temperature) specimens size C. Faces were polished to a 16 μm finish and edges chamfered to reduce surface flaws caused by machining.

Small cylindrical samples were also fabricated for microstructural characterization and conductivity measurements using a similar procedure. Relative density was measured using the Archimedes displacement method in distilled water. X-ray diffraction (XRD) analysis was conducted with a Smart Lab X-ray Diffractometer (Rigaku, Tokyo, Japan) using Cu-k_α radiation (wavelength 0.15406 nm) to verify phases and compositions. Scans consisted of 0.05° steps from 20° to 90°. Scanning electron microscopy (SEM) was performed using a Magellan 400 XHR (FEI, Eindhoven, Netherlands). A thin film of iridium was deposited on the surface using an IBS/e Ion Beam Sputter Deposition System (South Bay Technology, San Clemente, CA) to prevent electrical charging during SEM analysis. Grain boundaries in SEM images were outlined using image analysis software ImageJ (National Institute of Health, Bethesda, Maryland, USA), and measured values for grain diameters in two dimensions multiplied by 1.74 (the mathematical relationship between a regular polyhedron and equiaxed grain diameter) in order to obtain a ‘‘true’’ three dimensional grain size [56]. Approximately 400 grains were evaluated for each composition to determine the average grain size. Transmission electron microcopy (TEM) was conducted on a 200keV CM20 (FEI/Philips, Eindhoven, Netherlands) with samples prepared by focused ion beam (FIB) preparation using a Quanta 3D FEG Dual Beam (FEI, Eindhoven, Netherlands).

3.3.3 Mechanical and Thermal Shock Measurements

Hardness (H_v) and fracture toughness (K_{IC}) tests were conducted using a Zwick Z 3212 (Zwick GmbH, Ulm, Germany) micro hardness tester with a Vickers indenter. Specimens were polished to a 1 µm finish, and an 8 kg load was used to make each indentation. Eight indentations were taken at least 0.5 mm apart as to not influence one another. Hardness and fracture toughness were calculated using Eq. (3.1) and Eq. (3.2) [57], respectively:

$$H_v = 1.854 \frac{P}{d^2} \tag{3.1}$$

$$K_{IC} = 0.0937 \left(\frac{H_v P}{4r}\right)^{\frac{1}{2}} \tag{3.2}$$

where (H_v) is the Vicker hardness, (P) is the applied load, (d) is the diagonal indentation length, and (r) is the crack length.

Flexural strength (σ_f) was measured by three-point bend test using a crosshead speed of 0.5 mm/min and a span length of 40 mm. Flexural strength was calculated using Eq. (3.3):

$$\sigma_f = \frac{3P_f L}{2tw^2} \tag{3.3}$$

where (L) is the span length, (t) is the sample thickness, (w) is the sample width, and (P_f) is the maximum load to fracture. A minimum of 10 samples was tested in ambient conditions to determine the room temperature flexural strength. To determine the critical temperature difference, samples were held at various testing temperatures for 30 minutes before being quenched. Five samples were tested at each quenching temperature. Thermal shock testing took place over the temperature range of 313 K (100°C) to 523 K (250°C) by rapidly quenching specimens into a large water bath held at 295 K (22°C) and testing their residual strength via three-point bending. For each composition, the critical temperature difference (ΔT_c) can be calculated as the temperature at which a 30% decrease in flexure strength is observed in

accordance with ASTM C1525-02 (Determination of Thermal Shock Resistance for Advanced Ceramics by Water Quenching).

3.3.4 Electrochemical Impedance Spectroscopy Analysis

Conductivity measurements were carried out after finishing each face of the specimen with 600-grit silicon carbide paper, applying platinum paste to each face, and firing for 30 minutes at 1273 K (1000°C) to create porous platinum electrodes. Impedance spectra were obtained using a HP 4192A LF Impedance Analyzer (Hewlett Packard, Palo Alto, CA) in air, at frequencies over a range of 5 Hz–13 MHz and temperatures from 573 K (300°C) to 823 K (550°C) with 25(K/°C) increments. An applied voltage of 500 mV was used. A 30 minute dwell at each temperature was used for thermal stability prior to measurement and data collection. Impedance spectra plotted in Nyquist representation was fitted to the equivalent circuit model (Figure 3.1) by using the software package ZView (Scribner Associates, Southern Pines, NC, USA).

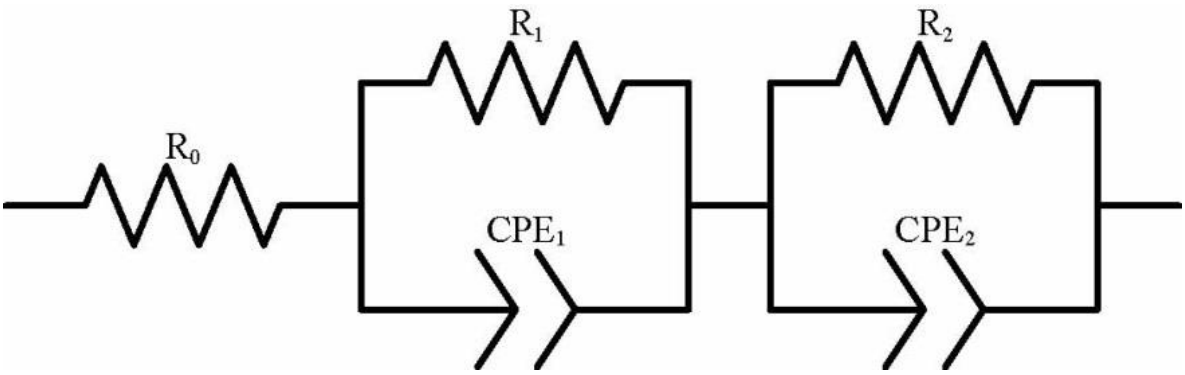

Figure 3.1 Equivalent circuit model used to fit impedance spectra where R_i represents resistor and CPE_i represents a constant phase element

3.4 Results and Discussion

3.4.1 Microstructure and Phase Characterization

X-ray diffraction analysis of all five compositions (Figure 3.2) show that no unintended crystalline phases form during sintering. Sintered materials are 98-99% dense (Table 3.3), a slightly higher density than 95-96% theoretical density for alumina-8YSZ composites data reported by Mori et al. [66].

Scanning electron microscope images (Figure 3.3) show a homogeneous distribution of the second phase additives throughout the 8YSZ microstructure. Higher amounts of the second phase are more effective in reducing the grain size due to grain boundary pinning, resulting in a reduction in the measured grain size of 8YSZ (Table 3.3). This effect is more prominent in the alumina composites in Figure 3.3(b-c), compared to the mullite composites in Figure 3.3(d-e), though both second phases had nominally the same starting crystallite size. The 8YSZ grain size differences could be due to differences in powder particle agglomeration or grain growth due to the formation of a liquid phase with rapid transport for the second phase mullite.

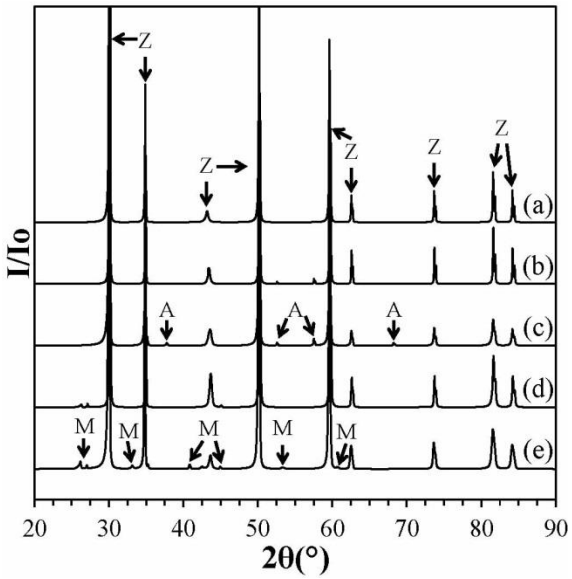

Figure 3.2 X-ray diffraction patterns for (a) 8YSZ, (b) 8YSZ+10%A, (c) 8YSZ+20%A, (d) 8YSZ+10%M and (e) 8YSZ+20%M. (Z=8YSZ, A=α-Al_2O_3, and M=mullite peaks).

Table 3.3 Theoretical density, measured relative density, and grain size.

	Theoretical density, ρ (g/cm^3)	Relative Density (%)	8YSZ Grain Size (μm)	Al_2O_3 Grain Size (μm)	Mullite Grain Size (μm)
8YSZ	6.0	98	9.2 ± 3.5	-	-
8YSZ+10%A	5.8	99	1.7 ± 0.8	0.9 ± 0.2	-
8YSZ+20%A	5.6	99	1.2 ± 0.9	0.8 ± 0.1	-
8YSZ+10%M	5.7	98	4.7 ± 1.6	-	1.8 ± 0.3
8YSZ+20%M	5.4	99	3.4 ± 1.2	-	2.0 ± 0.4

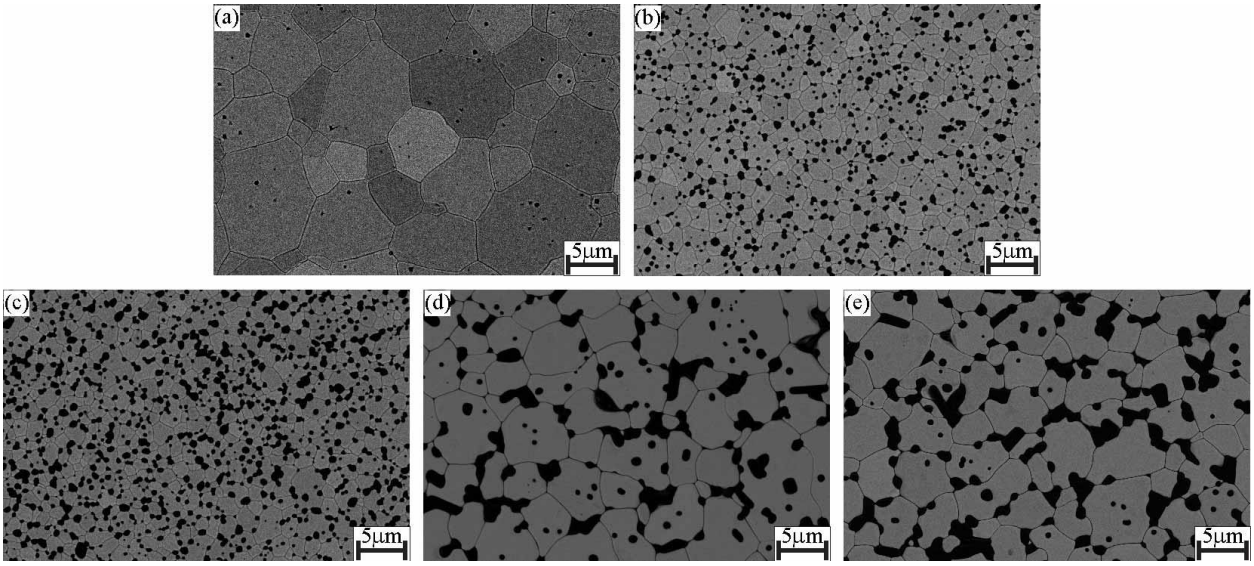

Figure 3.3 Backscatter electron image of 8YSZ (light phase) and the dispersed phase (dark phase, either alumina or mullite) for (a) 8YSZ, (b) 8YSZ+10%A, (c) 8YSZ+20%A, (d) 8YSZ+10%M and (e) 8YSZ+20%M.

In alumina composites, 8YSZ grain boundaries are sharply faceted at 8YSZ/Al_2O_3 interfaces and at triple grain junctions (Figure 3.4(a)). In contrast, the 8YSZ interface with mullite is rounded and grain boundary wetting of an intergranular phase located along the grain boundary in regions near mullite particles is evident (Figure 3.4(b)). The yttria-alumina-silica phase diagram includes a low melting point eutectic at 1644 K (1371°C) that could form during sintering [75] that could form from the aluminosilicate intergranular phase leaching out yttria preferentially from 8YSZ grains [76]. The low dihedral angle of the intergranular phase at grain

boundaries, presumably from a eutectic liquid that remains amorphous upon cooling to room temperature, can be seen to wet the grain boundaries in some regions as demonstrated by the dark field TEM image of Figure 3.4(c). The amorphous nature of the dark black wetting intergranular phases was determined by the lack of Bragg diffraction contrast upon tilting in the TEM and dark field imaging using diffuse scattering from the amorphous phase. The presence of an intergranular phase reduces the 8YSZ/8YSZ contact area for the 8YSZ+10%M and 8YSZ+20%M composites is expected to detrimentally reduce the ionic conductivity.

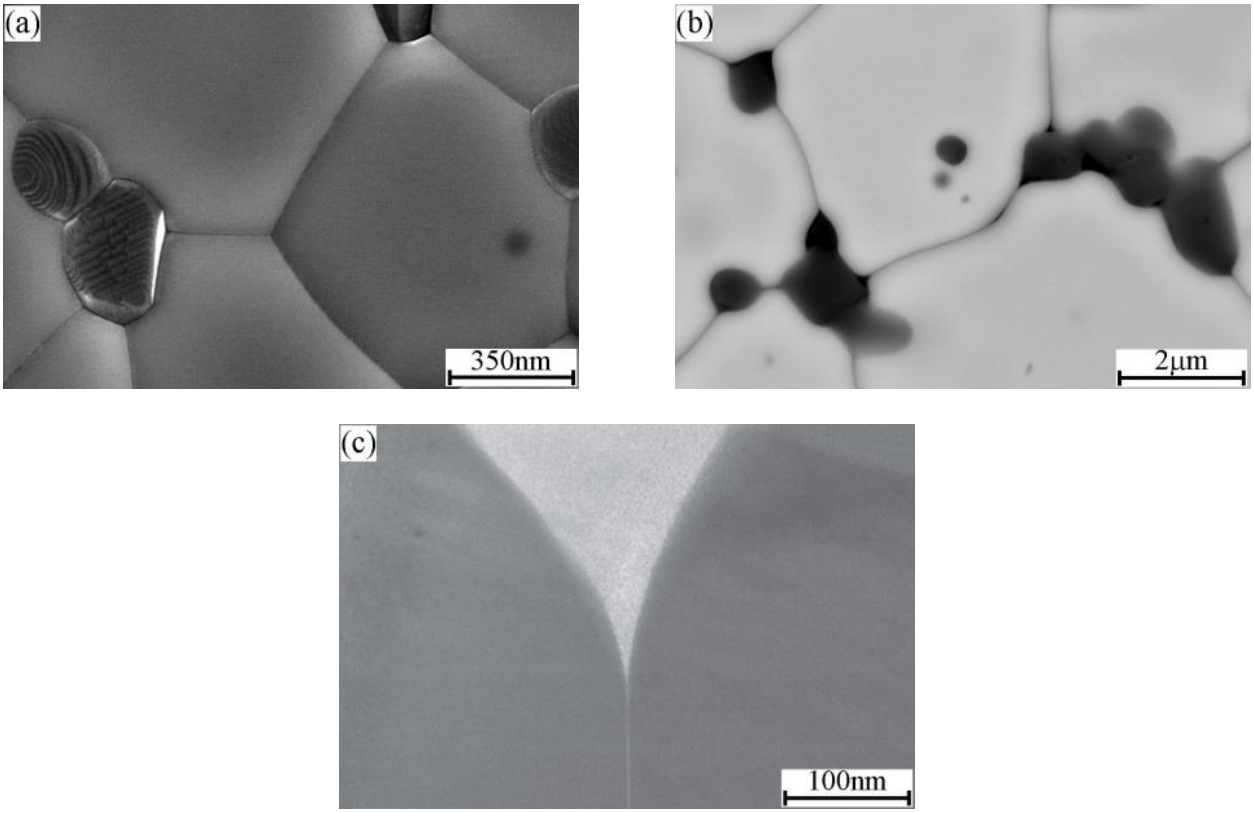

Figure 3.4 Grain boundary features of two phase samples. (a) 8YSZ+20% alumina SEM secondary electron imaging, shows sharply facetted grain boundaries and interfaces, (b) 8YSZ+20% mullite backscattered electron SEM image shows grey mullite particles and the presence of a black low dihedral angle intergranular phase at 8YSZ/mullite interfaces is typical of a glassy intergranular phase cooled from a liquid. (c) TEM dark field image of an amorphous intergranular pocket that wets the grain boundaries in 20% mullite/8YSZ samples.

3.4.2 Mechanical Behavior and Thermal Shock

Hardness and fracture toughness values for 8YSZ with additive are reported in Table 3.4. A 25% increase in hardness is observed in the 8YSZ+20%A and 8YSZ+20%M composites, while no significant change in hardness is seen with the addition of 10 vol% of either second phase. An 80% increase in fracture toughness of 8YSZ was observed in 10 vol% composites, while a 133% and 166% increase was seen in the 8YSZ+20%A and 8YSZ+20%M composites, respectively. The higher volume fraction of a second phase more effectively blocks crack propagation by deflection. These trends are similar to those reported in the literature for alumina/YSZ composites [77-78].

Table 3.4 Measured room temperature mechanical properties.

	Hardness, H_v (GPa)	Fracture Toughness, K_{IC} ($MPa \cdot m^{1/2}$)	Flexural Strength, σ_f (MPa)
8YSZ	15 ± 1.8	1.2 ± 0.1	197 ± 31
8YSZ+10%A	14 ± 1.0	2.2 ± 0.3	287 ± 19
8YSZ+20%A	20 ± 1.7	2.8 ± 0.2	317 ± 15
8YSZ+10%M	15 ± 1.7	2.3 ± 0.5	229 ± 18
8YSZ+20%M	19 ± 1.3	3.2 ± 0.5	263 ± 28

An 11% increase in the average room temperature flexural strength is observed for 10 vol% mullite additions but the standard deviations suggest that this increase may not be statistically significant. Composites with 20 vol% mullite and 10 vol% alumina have comparable increases to the average room temperature flexural strength of 28% and 31%, respectively. The elastic modulus of these two different second phase additive is significantly different, but also the distribution and grain size of the mullite particles is much larger than the alumina, which would also play a role as finer grain sizes produce higher strengths [79]. The 20 vol% alumina composites saw the largest increase the average room temperature flexural strength with a 47% increase over of pure 8YSZ, similar to that reported in the literature [66].

The predicted thermal shock resistance parameter (R) and heat flux resistance parameter (R') for each material system was calculated using the relationships [80-81]:

$$R = \sigma_f \frac{(1-\nu)}{E\alpha} \tag{3.4}$$

$$R' = kR \tag{3.5}$$

where (ν) is Possion's ratio, (E) is Young's modulus, (α) is coefficient of thermal expansion, and (k) is thermal conductivity. These parameters are used to predicted the temperature where a significant decrease in the strength will be observed (R) and the total allowable heat flux a specimen can withstand before crack initiation (R'). It should be noted that the (R) parameter, and subsequently (R'), cannot be correlated directly with the true thermal shock resistance [12; 82] and should not be used as the sole method for determining the thermal shock behavior of material systems.

Table 3.5 Experimental critical temperature difference (Figure 3.5), calculated thermal shock resistance parameter and maximum heat flux parameter.

	Measured Critical Temperature difference, ΔT_C (°C)	Calculated Thermal Shock Resistance, R (°C)	Calculated Maximum Heat Flux, R' (W/m)
8YSZ	122	61	122
8YSZ+10%A	154	83	220
8YSZ+20%A	185	92	319
8YSZ+10%M	129	72	161
8YSZ+20%M	150	89	222

Figure 3.5 shows the detailed results of the thermal shock tests for each material system. An increase in the critical temperature difference (ΔT_C) and thermal shock resistance is clearly seen for 8YSZ+10%A, 8YSZ+20%A and 8YSZ+20%M composites; with 8YSZ+20%A having an increase of 55% over the ΔT_C for 8YSZ. Calculated (R) and (R') parameters for each composite

are given in Table 3.5. A rule of mixtures was applied to data on the single phase mechanical properties in Table 3.1 (ν, E and α) to estimate values for the composites. The room temperature flexural strengths used to calculate R are from measured values in Table 3.4. Values of the room temperature thermal conductivity for each composite between 310-475 K (38-203°C) are given in Figure 3.6, data determined experimentally by the 3ω method (as reported elsewhere [3]) that show the increase in thermal conductivity with additions of higher thermal conductivity second phases. (These experimental values of thermal conductivity match well with Maxwell-Eucken models using the volume fraction of mullite in 8YSZ [3]).

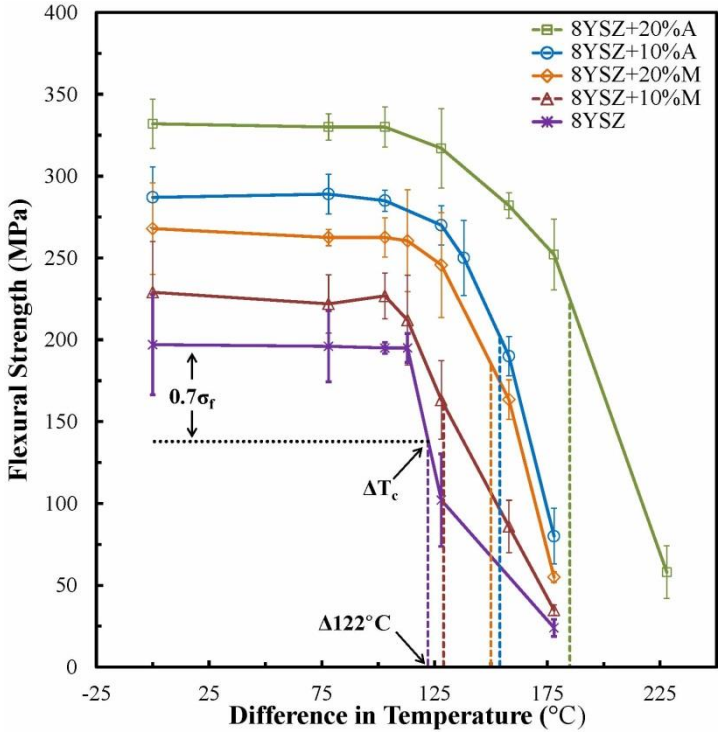

Figure 3.5 Thermal shock testing results of each composite system and 8YSZ control. Difference in temperature (x-axis) represents the difference between the water bath used to quench each sample and the furnace temperature. The 20% mullite/YSZ samples lost 30% of its initial strength at a relatively higher temperature than the 10% alumina/YSZ samples so has a higher value of thermal shock reported in Table 3.5.

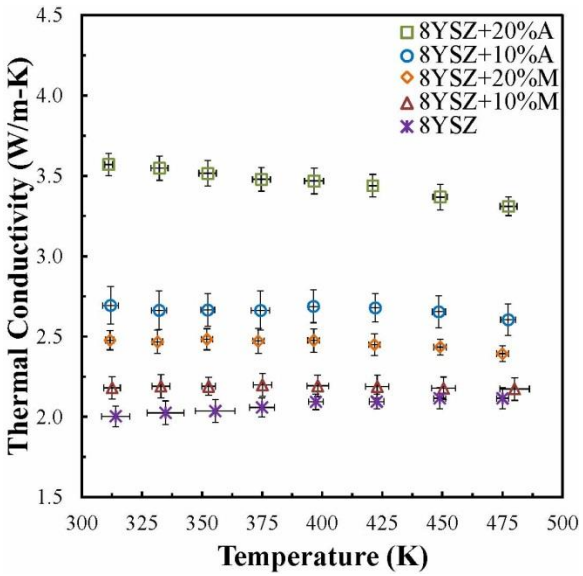

Figure 3.6 Thermal conductivity as a function of temperature for each composition measured by 3ω method [3].

The experimental data on thermal shock critical temperature difference (Table 3.5) fit the trends predicted by Eq. (3.4) and Eq. (3.5) and that is illustrated in Table 3.6. The predicted relative increases in the thermal shock resistance parameter (R) from Eq. (3.4) are close for few compositions. For 8YSZ with 20% alumina, the calculated R value predicts a 51% increase, compared to the 52% increase measured experimentally. However, for 8YSZ with 20% mullite, the predicted increase in thermal shock resistance is 46% with the actual increase 26%. (Using the "lower bound" model instead of the Voigt linear rule of mixtures for E gives even larger predicted increases for R). In contrast, there is a much better correlation of the measured increase is thermal conductivity and the measured increase in thermal shock in Table 3.6. This indicates that the increased strength from grain size reduction is not the primary factor for increased thermal shock resistance, but that thermal conductivity plays a significant role.

Table 3.6 The predicted thermal shock resistance (R) enhancement for each composition measured critical temperature difference increase in thermal shock (ΔT_C) normalized by ΔT_C for 8YSZ, and the thermal conductivity of each composite (k), normalized by 8YSZ (k_o).

	$\Delta T_C/\Delta T_{C\text{-}8YSZ}$	k/k_{8YSZ}	Predicted R/R_{8YSZ}
8YSZ+10%A	1.26	1.27	1.36
8YSZ+20%A	1.52	1.63	1.51
8YSZ+10%M	1.06	1.04	1.18
8YSZ+20%M	1.23	1.17	1.46

3.4.3 Impedance Analysis and Ionic Conductivity

Complex impedance spectra at 623 K (350°C) are shown in Figure 3.7 for each material system. Two distinct arcs are present and were fitted to an equivalent electrical circuit model shown in Figure 3.1. Typical impedance spectra for polycrystalline ceramics consist of three-arcs corresponding to (in order of decreasing frequency or increasing Z) the grain interior, grain boundary, and electrodes [83]; however due to testing limitations, only arcs for the grain interior and grain boundary components are observed. Beyond 823 K (550°C), the two arcs were not well defined and could not be separated. Resistivities are estimated by determining the interceptions of the arcs and the real axis. An increase in size of the high frequency arcs, associated with the grain interior component, indicates a decrease in conductivity in the grain interior. Likewise, an increase in the size of low frequency arcs, associated with the grain boundary component, shows a decrease in the grain boundary conductivity. For all materials, Figure 3.7 shows that additions of second phases to 8YSZ caused an increase are resistivity associated with grain boundaries and with the apparent bulk conductivity of the grains.

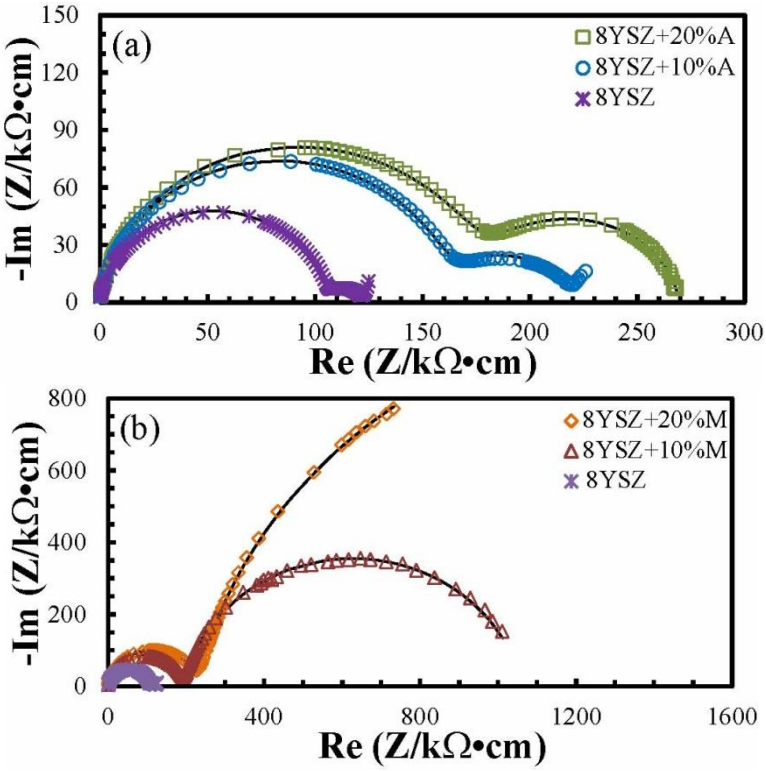

Figure 3.7 Impedance spectra at 623K (350°C) for (a) 8YSZ, 8YSZ+10%A and 8YSZ+20%A, and (b) 8YSZ, 8YSZ+10%M and 8YSZ+20%M. The impedance spectrum for 8YSZ was plotted on both graphs for comparison.

A table of representative grain interior and grain boundary conductivity at 573 K (300°C) for each composite as well as for the 8YSZ control is presented as Table 3.7. A 36% and 41% reduction in the grain interior ionic conductivity and a 73% and 85% reduction in the grain boundary conductivity are seen for 8YSZ+10%A and 8YSZ+20%A, respectively. Although alumina doping in small amounts (<1 vol%) can help scavenge impurities [25], additional amounts will degrade conductivity by replacing 8YSZ with a non-conducting phase and the true cross sectional area of 8YSZ is decreased.

Table 3.7 Grain interior, grain boundary, specific grain boundary (GB) and total conductivity measured at 573 K (300°C).

	Grain Interior Conductivity (Ω /cm)	Grain Boundary Conductivity (Ω /cm)	Specific GB Conductivity, (Ω /cm)	Total Conductivity (Ω/cm)
8YSZ	3.9×10^{-6}	2.3×10^{-5}	3.2×10^{-8}	2.7×10^{-6}
8YSZ+10%A	2.5×10^{-6}	6.3×10^{-6}	3.0×10^{-8}	8.8×10^{-6}
8YSZ+20%A	2.3×10^{-6}	3.4×10^{-6}	2.5×10^{-8}	5.7×10^{-6}
8YSZ+10%M	2.1×10^{-6}	3.6×10^{-7}	5.5×10^{-10}	2.5×10^{-6}
8YSZ+20%M	1.8×10^{-6}	1.3×10^{-7}	3.9×10^{-10}	1.9×10^{-6}

A 46% and 54% reduction in the grain interior ionic conductivities and a 98% and 99% reduction in the grain boundary conductivity were observed for 8YSZ+10%M and 8YSZ+20%M, respectively. The decrease in grain interior conductivity is attributed to the presence of a highly resistive second phase, and the decrease scales with increasing volume fraction of the inert second phase. Part of the reason for the higher decrease in grain interior conductivity for mullite containing sample with the same vol% second phase compared to alumina containing samples may also be due to the formation of an intergranular eutectic liquid scavaging yttria from grains for the case of mullite, forming an yttrium aluminosilicate glass that wets the grain boundary [76]. Decreased yttria content will result in a lowered ionic conductivity by decreasing the oxygen vacancy concentration, so the 8YSZ grains in the mullite composite would have a lower ionic conductivity compared to the same volume fraction of alumina, due to the intergranular phase observed in SEM and TEM images (Figure 3.4).

The reduction in grain size (Table 3.3) from grain boundary pinning by second phase particles results in an increase in the grain boundary surface area. There is an 81% and 87% decrease in 8YSZ grain size for 10 and 20 vol% alumina additions, respectively; and a 49% and 63% decrease in 8YSZ grain size for 10 and 20 vol% mullite additions, respectively. Since the grain boundary is intrinsically 100 to 1000 times less conductive then the grain interior in 8YSZ

[26], a smaller grain size also results in lowered ionic conductivity. This would be even further reduced if there is a blocking silicate phase segregated along grain boundaries, as in the case of 8YSZ+10%M and 8YSZ+20%M, the large decrease in grain boundary conductivity (Figure 3.7b) where such an intergranular silicate eutectic phases appears to have formed during sintering.

The specific grain boundary conductivity ($\sigma_{S.\ GB}$) is the average conductivity of a grain boundary [58], was and is calculated using:

$$\sigma_{S.\ GB} = \frac{\delta}{d}\sigma_{GB} \tag{3.6}$$

where (δ) is grain boundary width, (d) is grain size (Table 3.3) and (σ_{GB}) is grain boundary conductivity. This value is more representative than the total grain boundary conductivity which depends on the concentration of grain boundaries in a material. The specific grain boundary conductivity at 573 K (300°C) for each composite is also summarized in Table 3.7. This shows that alumina additions barely decrease the specific grain boundary conductivity of an average grain boundary by only 6% and 22% reduction for 8YSZ+10%A and 8YSZ+20%A respectively, and the higher density of grain boundaries is primarily responsible for the reduction in total conductivity. A much larger 99% and 98% reduction was measured for 8YSZ+10%M and 8YSZ+20%M respectively. This correlates well with the segregation of a thin intergranular film observed grain boundaries in the samples with mullite additives compared to the cleaner grain boundaries in with alumina additions. By normalizing for grain size, it is seen that the mullite grain boundaries are all approximately an order of magnitude lower in conductivity.

The effective grain boundary width to grain size ratio (δ/d) can be estimated by the ratio of grain interior capacitance (C_{GI}) to grain boundary capacitance (C_{GB}) and assuming $\varepsilon_{GB} \sim \varepsilon_{GI}$ [59] and is given in Table 3.8 using the following equation.

$$\frac{\delta}{d} = \frac{C_{GI}}{C_{GB}} \frac{\epsilon_{GB}}{\epsilon_{GI}} \tag{3.7}$$

The effective gain boundary width for 8YSZ was 7.2 nm and actually slightly decreased with small additions of alumina, perhaps due to the scavenging effect reported by others [25; 84-86]. A very significant increase in effective grain boundary width was found for 8YSZ+20%M, most likely related to the segregation of the intergranular phase giving a larger effective electrical grain boundary width. One caveat for the interpretation of such data is that the approximation that $\varepsilon_{GB} \sim \varepsilon_{GI}$ may not be correct when there is a uniform intergranular film along grain boundaries of a significantly different composition than the grains.

Table 3.8 Calculated values of effective electrical grain boundary widths.

	Grain Boundary Width, δ (nm)
8YSZ	7.2
8YSZ+10%A	6.4
8YSZ+20%A	9.2
8YSZ+10%M	8.3
8YSZ+20%M	12.3

Activation energies for the grain interior and grain boundaries were calculated by analyzing the temperature (T) dependence of the ionic conductivity (σ) using the Arrhenius equation:

$$\sigma = \frac{A}{T} \exp\left(\frac{-Q}{kT}\right) \tag{3.8}$$

where (k) is the Boltzmann constant and (Q) the activation energy. Figure 3.8 includes Arrhenius plots of total conductivity for each composite from 573 K (300°C) to 823 K (550°C). A drop in the total conductivity is seen for each composite. The high density of grain boundaries reduces the total conductivity in the alumina-containing samples due the much smaller grain size, while the mullite-containing 8YSZ has an even lower conductivity due to much lower conductivity of the average grain boundaries from silicate segregation. This effect is particularly easy to see in

the plots of Specific Grain Boundary Conductivity. The grain interior conductivity drop can be attributed to a smaller cross sectional area of 8YSZ due to the presence of inert second phase particles that do not conduct but it does not correlate directly with the volume fraction of the second phase.

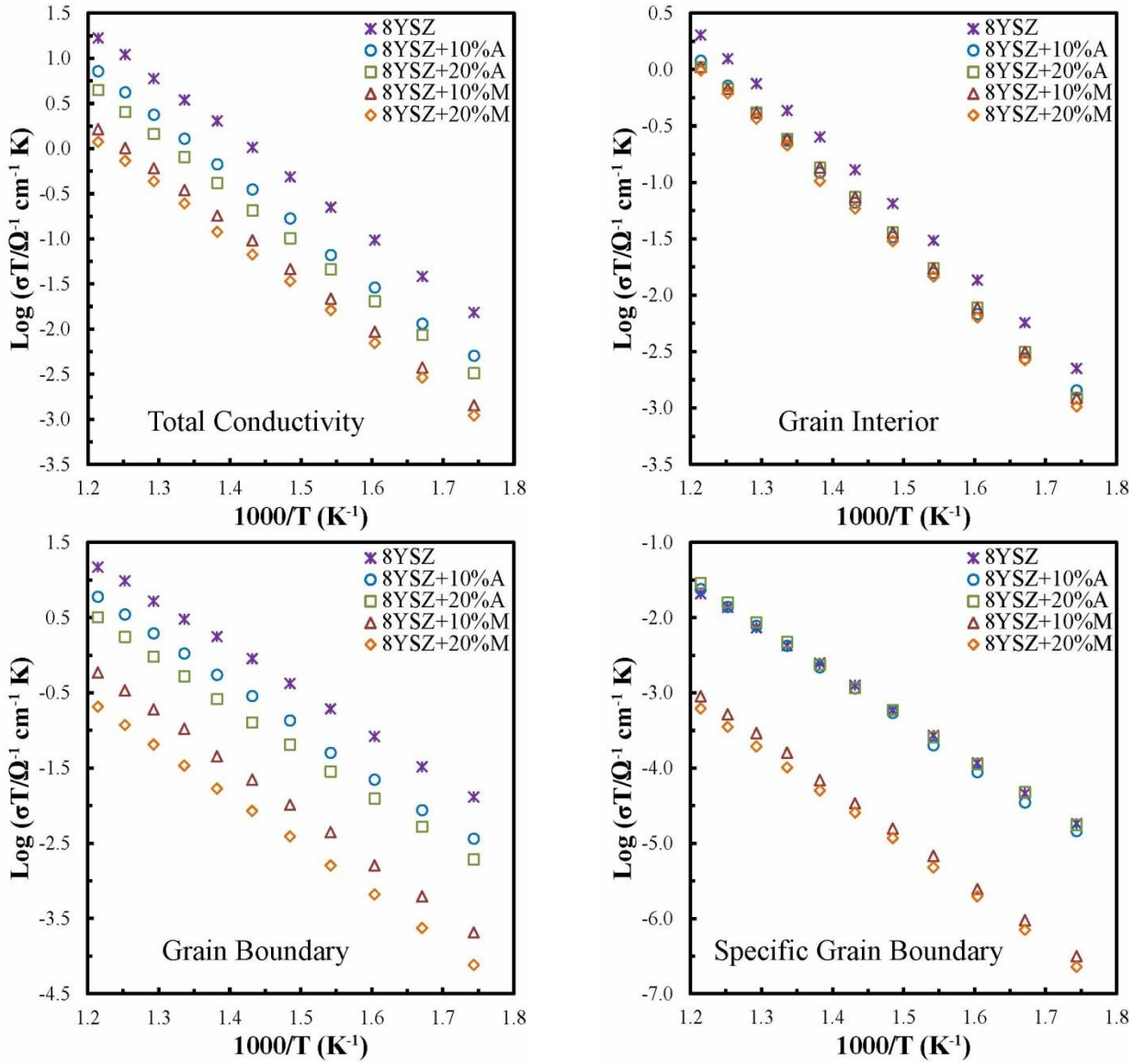

Figure 3.8 Arrhenius plots of conductivity. The Grain Boundary Conductivity is the total contribution from all grain boundaries while the Specific Grain Boundary Conductivity gives the average value per grain boundary.

Values for the activation energy of each composition are reported in Table 3.9 and are in close agreement with the commonly reported value of ~1.1 eV for yttria-stabilized zirconia [58; 83; 87-88]. No significant differences in the grain interior (also termed the bulk, volume, or lattice) activation energy are observed (Table 3.9) between the different materials. An almost imperceptible 2% and 4% increase in the grain boundary activation energy is calculated for 8YSZ+10%A and 8YSZ+20%A respectively. While alumina inhibits the conductivity through the reduction in grain size producing more blocking grain boundaries and the alumina phase does not conduct due to high resistivity, the mechanisms for ionic conduction remain the same as those in single phase 8YSZ. The addition of mullite, in contrast resulted in a 16% average increase in the grain boundary activation energy. This may indicate an additional blocking effect at the grain boundary. Silicate phase segregation at the grain boundary is known to cause such blocking effects [25; 58; 87; 89] and segregation of a thin intergranular silicate layer would certainly contribute.

Table 3.9 Grain interior, grain boundary and total activation energies for each material system.

	Grain Interior Activation Energy (eV)	Grain Boundary Activation Energy (eV)	Total Activation Energy (eV)
8YSZ	1.05	1.10	1.09
8YSZ+10%A	1.06	1.12	1.12
8YSZ+20%A	1.06	1.14	1.14
8YSZ+10%M	1.05	1.23	1.10
8YSZ+20%M	1.06	1.22	1.13

3.5 Conclusions

An increase in the hardness, fracture toughness and room temperature flexural strength with small amounts of alumina or mullite to 8YSZ can be attributed to the decrease in grain size and crack deflection through second phase blocking. Alumina was the most effective at reducing the grain size, while the mullite phase promoted the formation of an intergranular liquid phase during sintering that partially wet the grain boundaries at room temperature. The critical temperature difference found through thermal shock testing for each composite was significantly improved over 8YSZ. Of all compositions studied, the addition of 20 vol% alumina had the greatest effect on the thermal shock resistance of 8YSZ, achieving an increase of 55%. Increases in thermal shock correlates with higher thermal conductivity of the composites and not with the increase in the thermal shock resistance parameter. This suggests that a better parameter to consider for optimizing ceramics systems for improved thermal shock resistance is an increase in thermal conductivity (obtained here by the addition of higher thermal conductivity second phases) rather than focusing on the improvement of the material properties included in the thermal shock resistance parameter alone. Electrochemical impedance measurements showed that all additives between 10-20 vol% appeared to decrease the conductivity in the grain interior, but this is an artifact resulting from the large volume of a non-conductive phase. Specific grain boundaries in 8YSZ with alumina were just as conductive as in nominally pure 8YSZ. However, the finer grain size due to pinning the grain boundaries by alumina nanoparticles and the resultant much higher density of blocking grain boundaries lowered the total ionic conductivity. The addition of 10 and 20 vol% mullite reduced conductivity the greatest and increased the activation energy, even though the grain size was larger than alumina containing samples, due to the formation of an intergranular silicate phase that wets and segregates along grain boundaries.

In summary, using second phases to increase thermal shock resistance and fracture strength for electrochemical devices made of 8YSZ is a potentially effective strategy that can be employed, if a decrease in the ionic conductivity can be tolerated for the potential application. Careful selection of second phases that will not form a low melting point eutectic is required.

3.6 Specific Acknowledgments

Co-authors of this work include: James J. Steppan and Patrick M. Thompson from EmiSense Technologies, and Martha L. Mecartney from the University of California, Irvine. This research was supported in part by a UC Discovery Grant with matching funding from EmiSense Technologies LLC (formerly Innovate! Technology). The authors acknowledge the use of the Laboratory for Electron and X-ray Instrumentation (LEXI) at UC Irvine, using instrumentation funded in part by the National Science Foundation Center for Chemistry at the Space-Time Limit (CHE-082913). A U.S. Department of Education Graduate Assistance in Areas of National Need (GAANN) Fellowship provided additional graduate student support for JPA.

Chapter 4: Comparison of Two-Phase Thermal Conductivity Models with Experiments on Dilute Ceramic Composites

4.1 Abstract

Thermal shock resistance of cubic 8 mol% yttria stabilized zirconia (YSZ) can be increased by the addition of dilute second phases. This paper addresses how these dilute second phases affect the thermal conductivity for two-phase ceramic composites of 8 mol% YSZ with 10-20 vol% alumina (Al_2O_3) or 10-20 vol% mullite ($3Al_2O_3 \cdot 2SiO_2$). Thermal conductivity measurements from 310 K (37°C) to 475 K (202°C) were made using the 3ω method and compared to results from 3D analytical models and a 2D computational microstructure-based model (Object Oriented Finite Element Analysis, OOF2). The linear Rule of Mixtures was the least accurate and significantly overestimated the measured thermal conductivity at low temperatures, with errors in some cases exceeding 100%. Calculations using the Bruggeman and OOF2 models were both much better, and the deviation of less than $\pm$2.5% across all compositions and temperatures is within the range of experimental and modeling uncertainty. The Maxwell Garnett equation was a close third in accuracy ($\pm$8%). A sensitivity analysis for each model quantifies how small perturbations in the thermal conductivity of the dispersed second phase influence the effective thermal conductivity of the composite, and reveals that the linear Rule of Mixtures model is physically unrealistic and oversensitive to the thermal conductivity of the dispersed phase

4.2 Introduction

The effect of second phases on sintering, mechanical properties, and ionic conductivity of cubic 8 mol% yttria stabilized zirconia (8 mol% YSZ) has been of strong interest [25-26; 89-90] as commercial applications for cubic 8 mol% YSZ include solid oxide electrolytes for oxygen sensors and fuel cells [16; 24; 62-63]. Yet while thermal shock is one of the most common operational failure modes for 8 mol% YSZ oxygen sensors, relatively little work has been conducted on how second phases in YSZ affect thermal shock. Thermal shock and failure occur during rapid cooling for temperature differences as small as 100 K for single phase 6 mol% cubic YSZ [65] and 150 K for single phase 8 mol% cubic YSZ [66].

Dilute second phase additions of alumina in 8 mol% YSZ can increase the thermal shock resistance [66]. Dilute solutions are those in which the second phase is below the percolation limit. One effect of adding a second phase with a higher thermal conductivity, such as alumina in YSZ [91], is an increase in the effective thermal conductivity, with faster heat transfer from the interior to the exterior during quenching. Faster heat transfer reduces thermal gradients that cause residual stress due to thermal expansion. These thermal stresses are primarily responsible for crack propagation from preexisting flaws during thermal shock. In order to understand how second phases affect heat transport in 8 mol% YSZ in the temperature range where thermal shock occurs, an analysis of the thermal conductivity and its dependence on the microstructure, amount of second phases, and distribution of the second phase should be conducted, and is the focus of this paper.

Experimental characterization of the thermal conductivity for ceramics and ceramic composites is usually performed using the laser flash method over a range of temperatures, typically 373-1273 K (100-1000°C) [92]. At temperatures below approximately 473 K (200°C),

alternative techniques such as the 3ω method can also be employed [93-95]. Since YSZ has low electrical and thermal conductivity, it is a good candidate for the 3ω method, which requires only small temperature fluctuations for sensitive measurements.

Microstructure-based finite element modeling can be applied to approximate the thermal conductivity of composites and is especially useful because of its capability to account for size, shape, and distribution of second phase particles. Object-oriented finite-element analysis version 2 (OOF2) [60-61], open access software developed at the National Institute of Standards and Technology (NIST), can be used effectively for this purpose. OOF2 uses two-dimensional scanning electron microscopy (SEM) microstructures as the foundation for calculations, and has been applied to successfully characterize the thermal behavior with respect to porosity in **t'** 4 mol% YSZ thermal barrier coatings [96] and Cu-SiC composites [97], the latter with a honeycomb structure that allows two-dimensional modeling to be an appropriate approximation of three dimensions.

This paper evaluates four theoretical methods (OOF2 simulations, Maxwell Garnett, Bruggeman, and linear Rule of Mixtures approximation) used to predict the effective thermal conductivity of composite materials. The analytical models, Maxwell Garnett, Bruggeman, and linear Rule of Mixtures, only require knowledge of the three dimensional volume fraction of each phase and the respective thermal conductivities, but do not take into consideration microstructural details. In contrast, while the OOF2 simulations are fundamentally two-dimensional, they benefit from using real microstructural geometries of each phase when determining the effective thermal conductivity.

The linear Rule of Mixtures is simple but most appropriately used when each phase is contiguous and aligned parallel to the direction of heat flow [33]. It is sometimes used for two-

phase systems, randomly dispersed with respect to the heat flow, due to mathematical convenience for approximating the effective thermal conductivity (k_{eff}) based on the volume fraction of each phase. In the linear Rule of Mixtures, Eq. (4.1), k_1 is the thermal conductivity of Phase 1, k_2 is the thermal conductivity of Phase 2, and V_1 and V_2 are the respective volume fractions of the two phases.

$$k_{eff} = k_1 V_1 + k_2 V_2 \quad (4.1)$$

The inverse Rule of Mixtures is appropriate when each phase is contiguous and aligned perpendicular to the direction of heat flow [33].

$$\frac{1}{k_{eff}} = \frac{V_1}{k_1} + \frac{V_2}{k_2} \quad (4.2)$$

When the second phase is a low volume fraction and randomly dispersed, more appropriate equations are available for calculating effective material properties of composites, including the Maxwell Garnett and Bruggeman models [98-100]. Maxwell Garnett assumes the dispersed phase can be represented as spheres far enough apart to have negligible thermal interactions between particles [101]. Bruggeman uses the assumption that both of the components are randomly dispersed with no assumed shape, and is most accurate when one phase is below the percolation limit [102]. Both of these models have been applied to determine the effective thermal conductivity in 2-phase ceramic composites [31-32; 103-108]. (There are more complex expressions that can be employed when the dispersed phase has a specific geometric shape such as platelets, cylinders, etc., and when intergranular phases or delamination provides high interfacial resistance [109].) In both models, k_1 and V_1 are the thermal conductivity and volume fraction of the continuous phase (8 mol% YSZ in this case), respectively, and k_2 and V_2 are the thermal conductivity and volume fraction of the dispersed phase, respectively. The two-

component Maxwell Garnett model used to calculate the effective thermal conductivity of a two phase composite is given by Eq. (4.3).

$$k_{eff} = k_1 \left(\frac{k_2(1+2V_2)-k_1(2V_2-2)}{k_1(2+V_2)+k_2(1-V_2)} \right) \tag{4.3}$$

The two-component, three dimensional Bruggeman model used to calculate effective thermal conductivity is given by Eq. (4.4).

$$V_1 \left(\frac{k_1-k_{eff}}{k_1+2k_{eff}} \right) + V_2 \left(\frac{k_2-k_{eff}}{k_2+2k_{eff}} \right) = 0 \tag{4.4}$$

In this study, the thermal conductivity of 8 mol% YSZ with alumina (Al_2O_3) or mullite ($3Al_2O_3 \cdot 2SiO_2$) second phase additions is measured experimentally using the 3ω method for the temperature range for thermal shock of 8 mol% YSZ. The computational finite element approach of OOF2 and the three equation-based analytical models are used to approximate the effective thermal conductivity of two-phase ceramic composites and compared to the experimental 3ω measurements. A sensitivity analysis is performed on all four theoretical models to determine the effects of small perturbations in the thermal conductivity of the second phase on the effective thermal conductivity of the composites.

4.3 Experimental Procedures

4.3.1 Sample Preparation and Characterization

Ceramic powders of 8 mol% YSZ yttria-stabilized zirconia powder (Tosoh, Japan, crystallite size of 30 nm), high-purity α-alumina powder (Baikowski Inter. Corp., Charlotte, NC, crystallite size of 40 nm), or high-purity mullite powder (KCM Corporation, Japan, crystallite size of 40 nm) were attritor milled then formed into cylinders by cold isostatic pressing. Five compositions were made: 1) 8 mol% YSZ, 2) 8 mol% YSZ + 10 vol% alumina , 3) 8 mol% YSZ + 20 vol% alumina, 4) 8 mol% YSZ + 10 vol% mullite, and 5) 8 mol% YSZ + 20 vol% mullite. All were sintered at 1823 K (1550°C) for 2 hours. Density was measured by the Archimedes method.

X-ray diffraction (XRD) (Rigaku SmartLab X-ray Diffractometer) used Cu k_α radiation (wavelength 0.15406 nm) and scans from 20° to 90° in 0.05° steps. Scanning electron microscopy (SEM) was performed using a Philips XL 30 FEG. A thin film of iridium was deposited on the surface (South Bay Technology IBS/e Ion Beam Sputter Deposition System, San Clemente, CA) to prevent electrical charging during SEM analysis. Grain sizes were determined by ImageJ (National Institute of Health) with values for grain diameters in two dimensions multiplied by 1.74, the mathematical relationship between a regular polyhedron and equiaxed grain diameter, to obtain a ‘‘true’’ three dimensional grain size [56].

4.3.2 3ω Method

Each sample was polished to a finish of 0.06 µm. A gold heater line was patterned directly onto polished surfaces by photolithography and a liftoff method, with typical heater dimensions 10 µm width, 250 nm thickness, and 0.5 mm length between the inner voltage probes (Figure 4.1). A 10 nm layer of chromium was used to improve adhesion between the gold and sample.

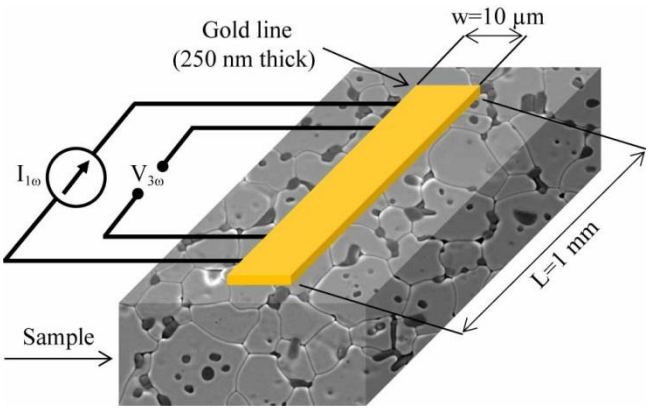

Figure 4.1 Schematic of a typical 3ω measurement setup. Not to scale. Typical sample thickness is 3 mm.

In the standard 3ω method the oscillating temperature field varies over a length scale known as the "thermal wavelength", defined as $\lambda=\sqrt{(D/2\omega)}$, where D is the thermal diffusivity and ω is the angular frequency of the heating current [94]. The approximate range of λ in this study is estimated as $8.7\mu m<\lambda<47\mu m$, based on the range of measurement frequencies ($890Hz>\omega/2\pi>30Hz$) and the diffusivity of conventional YSZ ($D\approx 8.4\times10^{-7}$ m^2/s) [110]. Since these λ values are much larger than the estimated phonon mean free paths in these materials (well below 100 nm), the continuum treatment of the standard 3ω method is justified [111].

Furthermore, the large heater length ensures that the measurement is an average over numerous grains. To ensure the stability of the heater line's electrical resistance, the samples were annealed at 500 K (227°C) after microfabrication and before measurements. Then 3ω data were collected from 310 K (37°C) to 475 K (202°C), waiting 30 minutes between every temperature point to ensure thermal stability. During the experiment, the 3ω method also causes a small steady-state temperature increase of the heater line above the bulk sample temperature, with a typical value $T_{Heater} \approx T_{Bulk\ Sample} + 5\ K$. To reflect this data are plotted at $T_{avg} = (T_{Heater} + T_{Bulk\ Sample})/2$ and error bars reflect this difference between T_{Heater} and T_{avg} as well as the inherent temperature uncertainty of typically 0.5%.

4.3.3 OOF2 Simulations

A thermal gradient model was produced using OOF2 for each composition. Two-dimensional SEM images are converted to two-color images in order to create finite-element meshes adapted to the microstructure of the material. Each phase is represented by a single color value and assigned input values for thermal conductivity as a function of temperature from experimental results on single-phase materials [55; 112-113].

A thermal gradient is simulated in the vertical direction of the image by assigning the top boundary a fixed temperature value and the bottom boundary a value 10 K higher, keeping the other two sides adiabatic. The heat equation is solved by the conjugate gradient method, resulting in an x and y heat flux component assigned to each node of the mesh. OOF2 removes the third dimension by setting the out-of-plane (z) heat flux components to zero, analogous to plane-stress analysis used in fracture mechanics. The resulting 2D heat flux is integrated across the top to determine the effective thermal conductivity:

$$k_{eff} = \frac{L_y Q}{L_x\left(T_{bottom} - T_{top}\right)} \tag{4.5}$$

where k_{eff} is the effective thermal conductivity of the composite, Q (watts per meter of thickness in z) is the OOF2 heat flux integrated across the bottom boundary, L_y and L_x are the image dimensions, and T_{bottom} and T_{top} are the temperature values assigned to the bottom and top boundaries. By simulating a thermal gradient across an image, k_{eff} is calculated at various temperatures from 298-473 K (25-200°C). Three representative SEM micrographs were used for each composition to calculate the average effective thermal conductivity. Typical variability between each simulation for the same composition was less than 1%.

4.3.4 Dimensionless Sensitivity Analysis

The dimensionless sensitivity parameter, S_{ki}, is the fractional change in k_{eff} when the thermal conductivity of a specific phase (i=continuous or dispersed) is perturbed while the other held constant. For example, if a 1% change in k_2 leads to a corresponding 1% change in k_{eff}, then the dimensionless sensitivity parameter is $S_{k_2} = 1$, meaning k_{eff} is fully sensitive to k_2. Likewise, if $S_{k_2} = 0.3$, then a 1% change in k_2 would cause a 0.3% change in k_{eff}. Mathematically, the sensitivity of k_{eff} to changes in the thermal conductivity of the dispersed phase (k_2) is

$$S_{k_2} = \frac{k_2}{k_{eff}} \left.\frac{\partial k_{eff}}{\partial k_2}\right|_{k_1} \tag{4. 6}$$

Likewise, by exchanging k_2 for k_1, the sensitivity of k_{eff} to the continuous phase can also be determined. It is easily shown that this sensitivity analysis follows a "sum rule", namely $S_{k_1}+S_{k_2}=1$.

For the three analytical models described above, expressions for S_{k_2} are derived and given as,

$$S_{k_2,\text{Rule of Mixtures}} = \frac{k_2}{k_{eff}} V_2 \tag{4.7}$$

$$S_{k_2,\text{Maxwell Garnett}} = \frac{k_2 V_2}{k_{eff}} \left(\frac{3k_1}{k_1(2+V_2)+k_2(1-V_2)}\right)^2 \tag{4.8}$$

$$S_{k_2,\text{Bruggeman}} = \frac{k_2}{k_{eff}} \left(\frac{k_1 + k_{eff}(3V_2-1)}{4k_{eff} + k_1(3V_2-2) - k_2(3V_2-1)}\right) \tag{4.9}$$

4.4 Results and Discussion

4.4.1 Microstructure and Phase Characterization

Samples are 98-99% dense (Table 4.1), with the second phase fairly homogeneously distributed throughout the 8 mol% YSZ microstructure (Figure 4.2). The second phase limits the grain growth of 8 mol% YSZ due to grain boundary pinning and results in a reduction in grain size (Table 4.1).

Table 4.1 Theoretical density, relative density, and grain size of 8 mol% YSZ with and without second phase additions of alumina and mullite.

	Theoretical Density (g/cm3)*	Relative Density (%)	Grain Size (μm)
8 mol% YSZ	6.0	98	9.2
8 mol% YSZ + 10 vol% Al2O3	5.8	99	1.7
8 mol% YSZ + 20 vol% Al2O3	5.6	99	1.2
8 mol% YSZ + 10 vol% Mullite	5.7	98	4.7
8 mol% YSZ + 20 vol% Mullite	5.4	99	3.4

*For composites, theoretical density is calculated by a rule of mixtures using density values of pure phases.

Higher amounts of the second phase are more effective in reducing the grain size. The larger reduction in grain size in the alumina composite compared to the mullite composite (Figure 4.2) could be due to differences in either powder particle agglomeration or grain growth and transport rates of the second phase. However, the final grain sizes are much larger than nanoscale dimensions where the high density of grain boundaries would significantly decrease thermal conductivity [114]. XRD of all compositions show no additional phase formation during sintering (Figure 4.3).

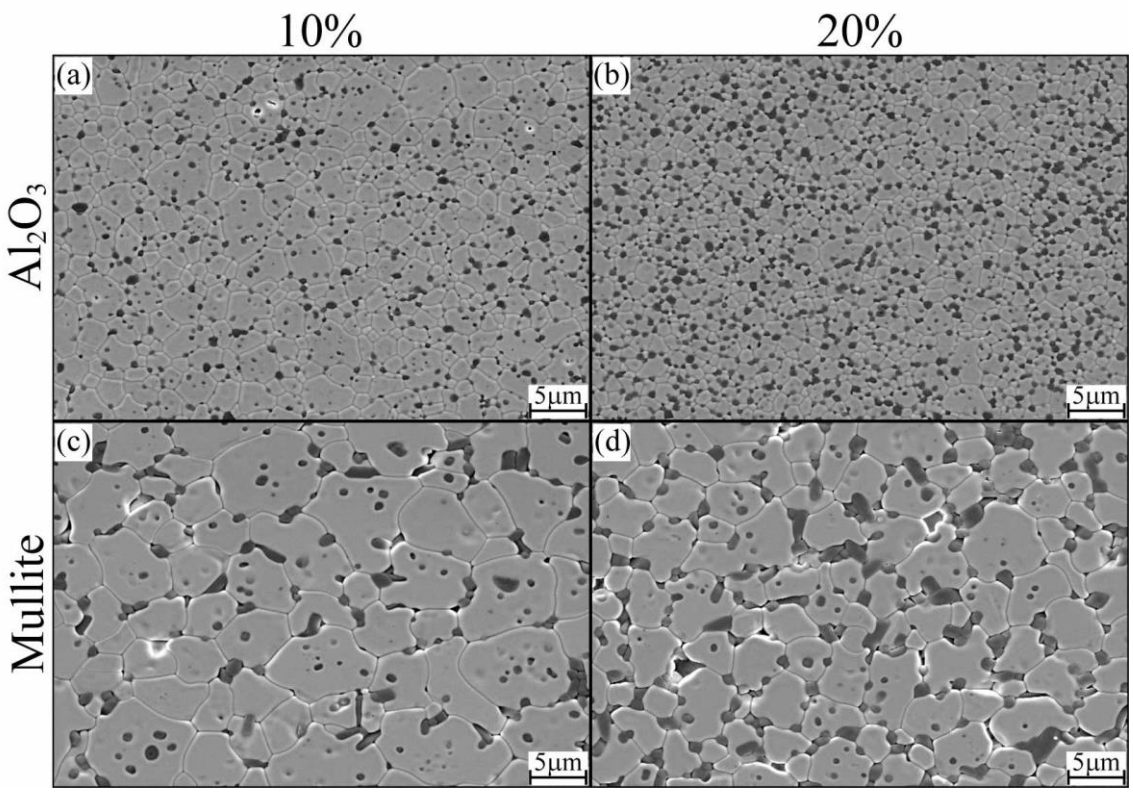

Figure 4.2 SEM micrographs of 8 mol% YSZ (light phase) and dispersed phase (dark phase, alumina or mullite) for (a) 10 vol% Al_2O_3, (b) 20 vol% Al_2O_3, (c) 10 vol% Mullite, and (d) 20 vol% Mullite

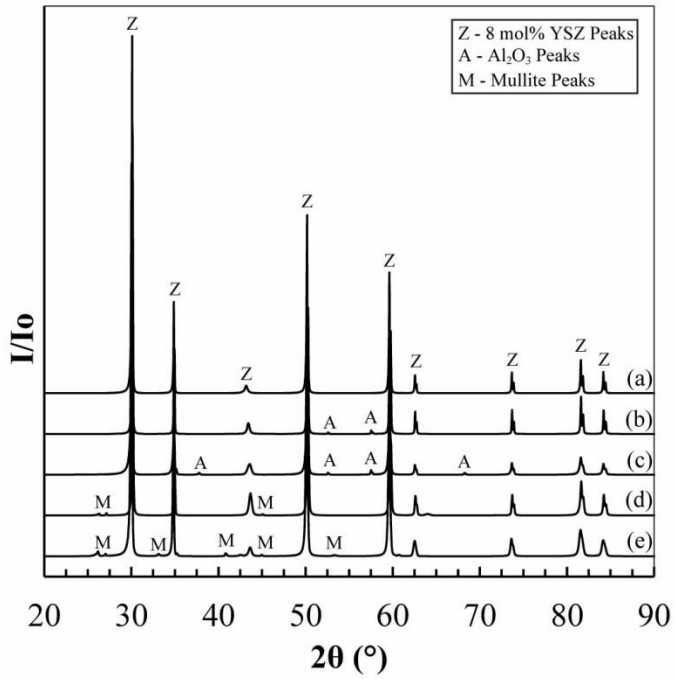

Figure 4.3 X-ray diffraction of samples (a) 8 mol% YSZ, (b) + 10 vol% Al_2O_3, (c) + 20 vol% Al_2O_3, (d) + 10 vol% Mullite, and (e) + 20 vol% Mullite.

4.4.2 Thermal Conductivity Measurements

The 3ω thermal conductivity of most composites decreases slightly as testing temperature is increased (Figure 4.4). 20 vol% alumina has the largest thermal conductivity compared to single phase 8 mol% YSZ, followed by 10 vol% alumina, 20 vol% mullite, and 10 vol% mullite, with 10 vol% mullite only slightly higher than single phase 8 mol% YSZ (Figure 4.4). The large increase in thermal conductivity for alumina-containing composites is due to the relatively high thermal conductivity, $k_{alumina,\ RT} \approx 33$ W/m-K [55] compared to 8 mol% YSZ, $k_{8\ mol\%\ YSZ,\ RT} \approx 1.8 - 2.4$ W/m-K [69-71], while the smaller increase in thermal conductivity in mullite composites can be attributed to mullite having a much lower thermal conductivity than alumina, $k_{mullite,\ RT} \approx 6$ W/m-K [112]. The thermal conductivity of single phase 8 mol% YSZ increases slightly from room temperature to approximately 573 K (300°C), where it plateaus, and agrees with published data within 8% deviation [70-71] . Interestingly, 10% mullite in 8 mol% YSZ results in almost constant thermal conductivity over the temperature range studied, as the decreasing mullite thermal conductivity effectively counteracts the increasing 8 mol% YSZ conductivity.

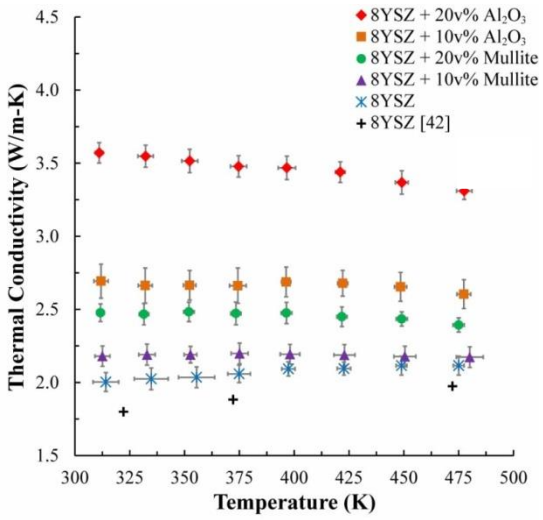

Figure 4.4 Measurements of thermal conductivity with experimental uncertainty for single phase 8YSZ and composites using 3ω method. 8YSZ data from [71] included for comparison.

A representative OOF2 meshed microstructure of 8 mol% YSZ + 20 vol% alumina is constructed using a combination of triangular and rectangular finite elements, with a larger density of elements located at the interface between two phases (Figure 4.5). Further refinement of the mesh did not change the convergence of the solution. To calculate the effective thermal conductivity for each composite, the heat flux vector is calculated at each node. A heat flux map is generated by taking the scalar magnitude of this vector and illustrates how the second phase creates preferred pathways for heat flow in the direction of the applied temperature gradient, seen in the representative microstructure with an overlaid heat flux map (Figure 4.6).

Figure 4.7 and 4.8 compare measured thermal conductivity values for 8 mol% YSZ with 10 and 20 vol% second phases with the four theoretical methods (OOF2 simulations, Maxwell Garnett model, Bruggeman model, and linear Rule of Mixtures approximation). The linear Rule of Mixtures exceeded 100% error in some cases, as this approximation overemphasizes the higher thermal conductivity dispersed phase. In these samples this problem is worst at low temperatures because the contrast between k_1 and k_2 is greatest there (both alumina and mullite have a strongly temperature dependent conductivity in this regime, scaling approximately as T^{-1}).

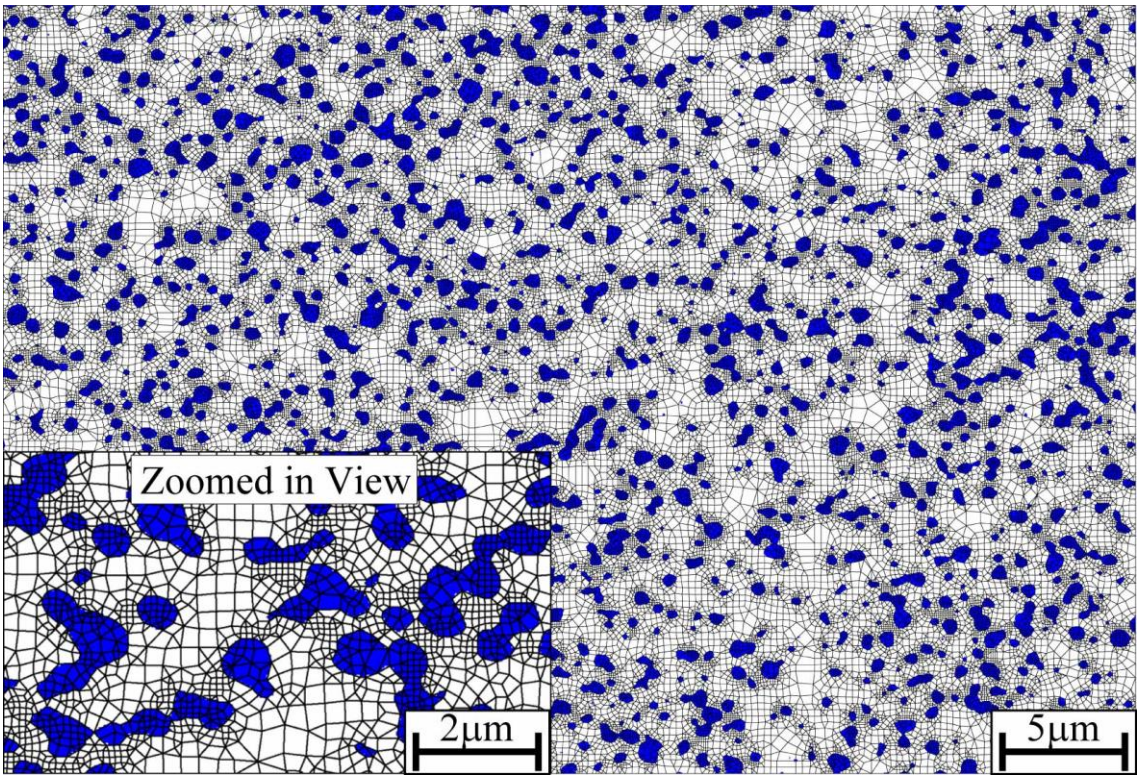

Figure 4.5 OOF2 meshing for 8 mol% YSZ (white) + 20 vol% Al2O3 (blue). Image correlates to Figure 4.2b. A finer mesh and higher node density along the phase interface can be seen in the zoomed in view.

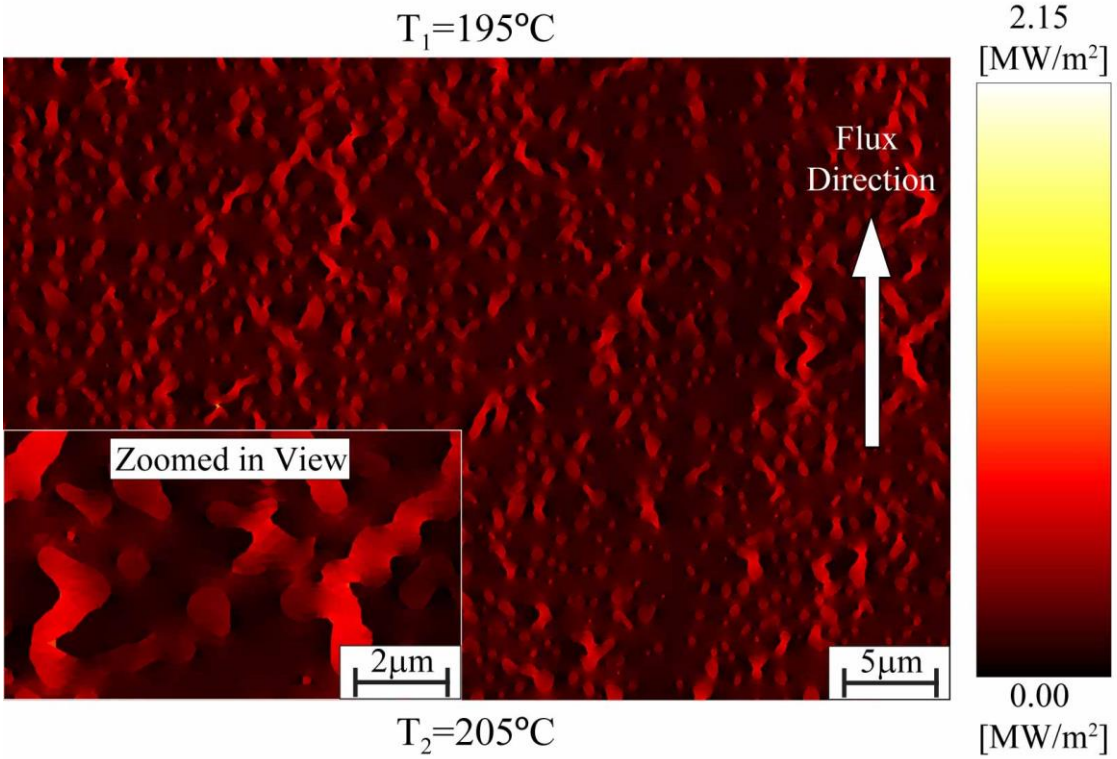

Figure 4.6 Heat flux map of 20 vol% alumina corresponding to Figure 4.5, produced by OOF2 simulation. Thermal gradient is imposed from bottom to top, keeping sides adiabatic.

The other three models are within ±8% error or less for each composite. Among these three models, for the 10 and 20 vol% alumina composites the Maxwell Garnett calculations have the worst agreement with the experimental values, ±8% error for 20 vol% alumina and ±5% error for 10 vol% alumina. OOF2 simulations are found to provide only ±2% error compared to experimental values for the 10 vol% alumina composite (Figure 4.7a). Both OOF2 and Bruggeman produce similar values for the 20 vol% alumina (Figure 4.7b); OOF2 gave an under approximation and Bruggeman an over approximation but both models were within ±2% error. As seen in Figure 4.8, OOF2 simulations resulted in thermal conductivity values closest to experiments for both 8 mol% YSZ + 10 and 20 vol% mullite composites with only ±1.25% and ±0.5% error, respectively.

Maxwell Garnett and Bruggeman calculations give higher k_{eff} values than OOF2 for mullite composites. The power of the OOF2 simulations is that real microstructures are used, although this is also one of the challenges since SEM images must be obtained, whereas the Maxwell Garnett and Bruggeman models assume simpler distributions and simpler grain shapes. A caveat with OOF2 is that one must ensure that the variability in the real microstructure is accurately represented, hence the use of multiple images from different sections of the material. Also it must be remembered that OOF2 simulations are fundamentally two dimensional, and this may underestimate the true three-dimensional thermal conductivity (see Section 4.4.3). In the present study, allowing for the uncertainty in model inputs (estimated as ±4%), the OOF2 and Bruggeman results both fall within the uncertainty of the experimental results.

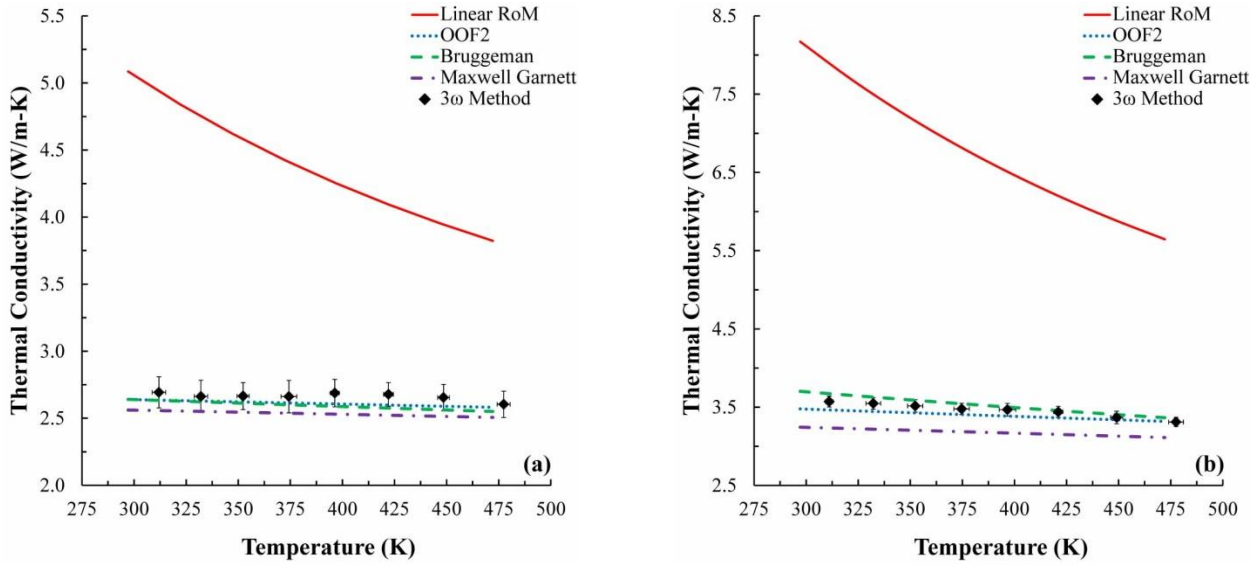

Figure 4.7 Comparison of different models with experimental data (3ω method) for thermal conductivity of (a) 8 mol% YSZ + 10 vol% Al2O3 and (b) 8 mol% YSZ + 20 vol% Al2O3. (Lines: modeled and simulated results. Points: experimental results. Rule of Mixture abbreviated as RoM)

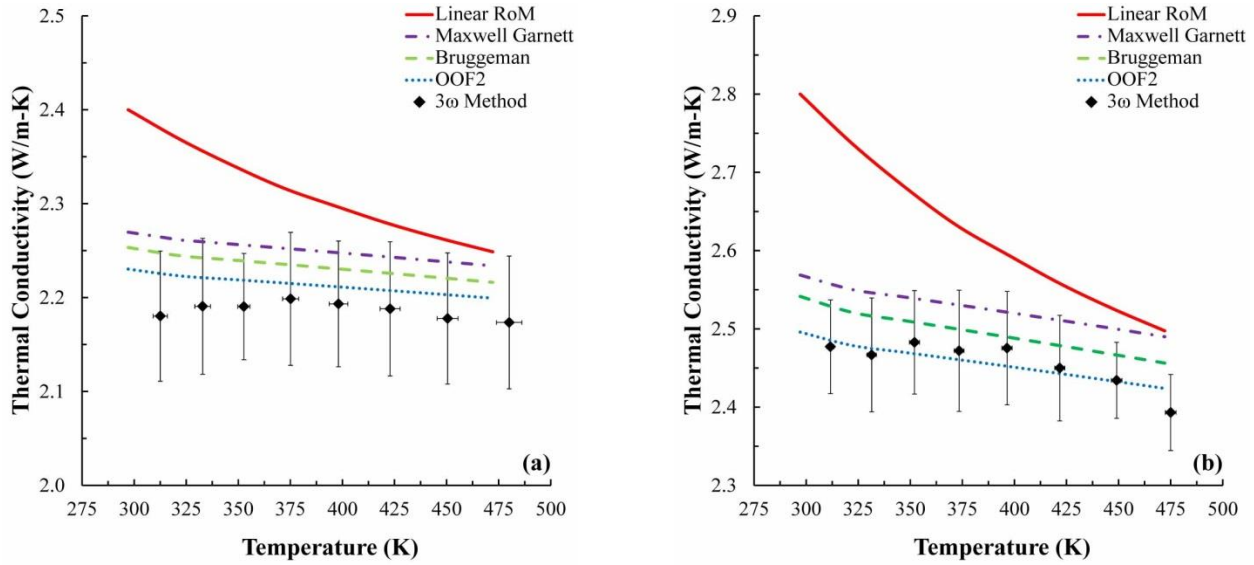

Figure 4.8 Comparison of models to 3ω thermal conductivity for (a) 8 mol% YSZ + 10 vol% mullite and (b) 8 mol% YSZ + 20 vol% mullite. (Lines: modeled and simulated results. Points: experimental results.) Thermal conductivity scale expanded compared to Figure 4.4 and 4.7.

4.4.3 2D Approximations of a 3D Material

It is noteworthy that the OOF2 calculations are so close to the experimental thermal conductivity in Figure 4.7 and 4.8 despite OOF2 being a two-dimensional approach. If the heat flux vectors in a real three-dimensional (3D) system are dominated by flow in a two-dimensional (2D) plane, then an OOF2 analysis of the effective conductivity of this plane will give a very accurate representation of the real 3D conductivity. In terms of Figure 4.2, 4.5, and 4.6, this would require that all the heat flows in the XY plane, with no local heat fluxes in the Z direction. However, in these samples, the dispersed particles are randomly distributed and approximately equiaxed, and local heat fluxes will have a significantly 3D nature.

To quantify potential errors for approximating a 3D microstructure with a 2D calculation, we can use the known 3D and 2D forms of the Bruggeman model [115]. Recognizing that in the alumina-YSZ composite $k_2/k_1 > 10$, it is a reasonable first approximation and also conservative (worst-case) bound to set $k_2/k_1 \rightarrow \infty$, leading to the simplified Bruggeman expressions:

$$\text{3D:} \quad \frac{k_{eff,3D}}{k_1} = \frac{1}{1-3V_2} \quad , \quad \text{2D:} \quad \frac{k_{eff,2D}}{k_1} = \frac{1}{1-2V_2}. \tag{4.10}$$

The 2D expression is traditionally given in terms of an area fraction (e.g., A_2), which here we replace by the volume fraction V_2. This is appropriate because a physically equivalent 3D system can be obtained by extrusion of the same 2D (XY) inclusion geometry uniformly along the third dimension (Z).

The error ratio between the two expressions is:

$$\frac{k_{eff,\,3D}}{k_{eff,\,2D}} = \frac{1-2V_2}{1-3V_2}. \tag{4.11}$$

Although the specific form of Eq. (4.11) arose from Bruggeman, the qualitative conclusion that $k_{eff,3D} > k_{eff,2D}$ for the same volume fraction can also be reached by comparing 2D and 3D bounding analyses following Elrod [116]. A similar trend is also expected from an argument that

reducing the dimensionality is equivalent to imposing additional constraints that also reduce k_{eff} [115]. Thus, regardless of the theory used we conclude that a 2D calculation based on a planar section of a 3D microstructure will underestimate the true 3D conductivity. For the alumina-YSZ composites of the present work, the 3D/2D errors such as estimated from Eq. (4.11) are likely to be no more than a few tens of percent, with smaller errors as the k_2/k_1 ratio becomes closer to unity (e.g. at higher temperatures and for the mullite-YSZ composites). Figure 4.9 shows how the linear Rule of Mixtures and the inverse Rule of Mixtures serve as upper and lower bounds for thermal conductivity.

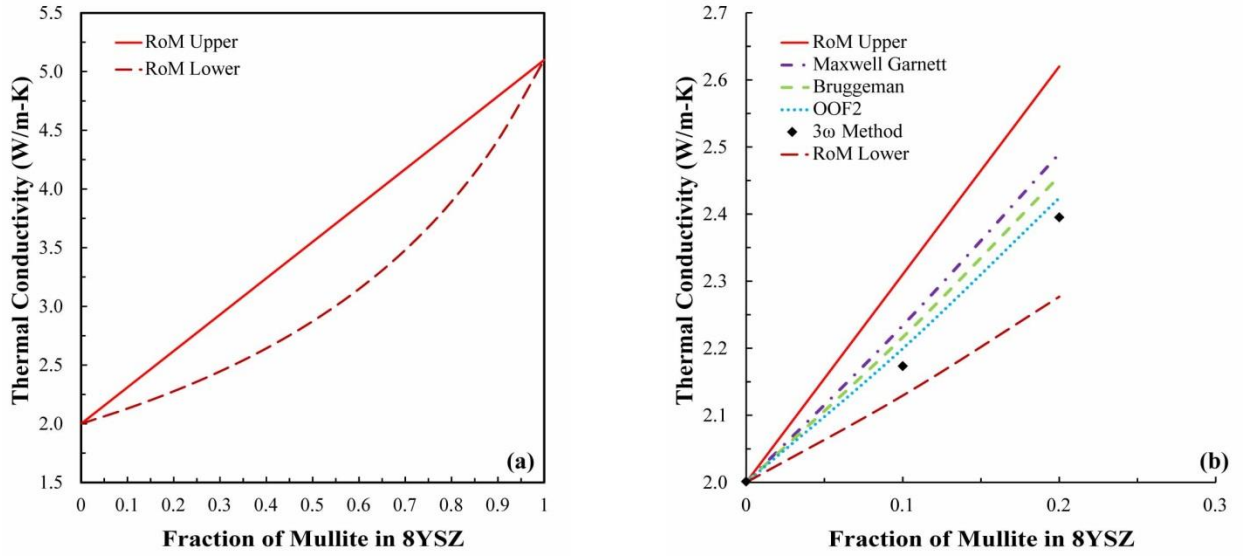

Figure 4.9(a) Linear Rule of Mixtures (upper bound) and inverse Rule of Mixtures (lower bound) for 8YSZ and mullite composites at 200°C. (b) Comparison with experimental thermal measurements (3ω method), analytical models and OOF2.

4.4.4 Sensitivity

Figure 4.10 shows the dimensionless sensitivity of k_{eff} to k_2 for each analytical model and OOF2 simulations. The sensitivity parameter S_{k_2} is calculated for each temperature and the average values with standard deviations are reported in Figure 4.10. The sensitivity of OOF2 is determined numerically, by increasing the thermal conductivity of the dispersed phase by 5% and calculating the percent increase in k_{eff} relative to the 5% increase.

All four calculations of Figure 4.10 exhibit the same trend that S_{k_2} increases with volume fraction V_2 (for fixed k_2). This is expected because the smaller the V_2, the less the influence k_2 has on k_{eff}. Comparing the alumina and mullite results in Figure 4.10, the Maxwell Garnett model, Bruggeman model, and OOF2 simulations also all show that S_{k_2} decreases with increasing k_2 (for fixed V_2). In contrast, the linear Rule of Mixtures model shows an opposite trend of S_{k_2} increasing with k_2, which we now show is non-physical and thus highlights another shortcoming of the linear Rule of Mixtures approximation.

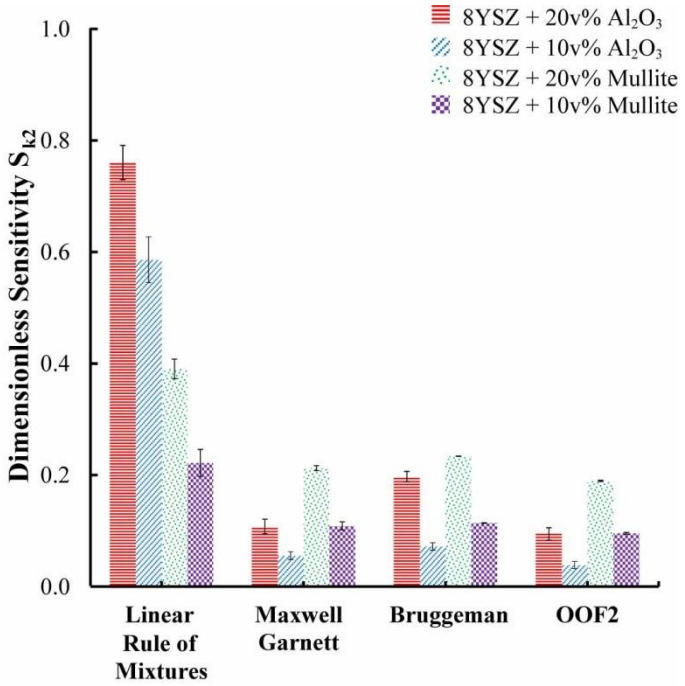

Figure 4.10 Average values with standard deviations for the dimensionless sensitivity parameter $\mathbf{S_{k_2}}$ for each analytical model and OOF2.

The physical argument is as follows. Since the particles are dispersed and isolated, clearly k_{eff} must saturate to a finite value even in the limit that $k_2 \rightarrow \infty$. Therefore, for any fixed V_2, k_{eff} should be most sensitive to k_2 when k_2 and k_1 are of similar magnitudes, while (for a dispersed particle system) S_{k_2} should fall off to zero for both $k_2 >> k_1$ and $k_2 << k_1$. In the present work, k_2 is

already larger than k_1, thus explaining why Figure 4.10 should show smaller sensitivity to alumina ($k_2/k_1 \approx 16$) than to mullite ($k_2/k_1 \approx 3$). On the other hand, the linear Rule of Mixtures model from Eqn. 1 is formally equivalent to conductors in parallel, so in the limit $k_2 \rightarrow \infty$ it wrongly gives $k_{eff} = V_2 k_2$ and $S_{k_2} \rightarrow 1$.

To illustrate the impacts of sensitivity on error propagation in the model calculations, we suppose that the uncertainty in the model inputs k_1 and k_2 is around 5%. For the 20 vol% alumina sample, Figure 4.10 shows that S_{k_2}, for the three preferred models is around 0.15. This means that a 5% uncertainty in k_2 contributes to only around 0.75% uncertainty in k_{eff}. Similarly, using the sum rule stated above we get $S_{k_1} = 0.85$, showing that a 5% uncertainty in k_1 contributes 4.25% uncertainty in k_{eff}. These two error sources are assumed uncorrelated, so their contributions are added in quadrature to obtain a total uncertainty in the calculated k_{eff} of $\sqrt{(0.75\%)^2+(4.25\%)^2}=4.3\%$. This is clearly dominated by the uncertainty in the k_1 of the 8 mol% YSZ matrix.

The sensitivity calculations also quantify the potential for further increasing k_{eff} by using inclusions of even higher k_2. For example, at V_2 = 20 vol%, replacing alumina by another material with 33% higher thermal conductivity ($k_2 \approx$ 43 W/m-K rather than 33 W/m-K) would only increase k_{eff} further by around 5%. In the extreme limit $k_2 \rightarrow \infty$, for V_2 = 20% the models show that $k_{eff}/k_{8\ mol\%\ YSZ}$ will be at most 2.5 (Bruggeman) or 1.75 (Maxwell Garnett), which shows there still may be some room for improvement compared to the present results ($k_{eff,alumina}/k_{8\ mol\%\ YSZ} \approx 1.6$).

4.4.5 Porosity Effects

The effect of porosity on the effective thermal conductivity of bulk ceramics has been considered in a number of previous works [71; 95; 113] but not considered in this study, as the samples contained minimal porosity (approximately 1% - 2%: Table 4.1). In the limit of small porosity, most standard expressions take the form $k_{eff}=k_{Fully\ Dense}\times(1-c\phi)$, where ϕ is the porosity and c is a numerical factor. Kingery et al. [113] used c=1, Klemens [117] obtained c=4/3, and the Maxwell Garnett Eq. (4.3) and Bruggeman Eq. (4.4) expressions above correspond to c= 3/2. Therefore, the present samples with $\phi \approx 2\%$ are expected to have a porosity effect on the thermal conductivity of no more than 3%, which will not significantly impact the results.

4.5 Conclusions

Thermal conductivity measurements over a temperature range 310 K (37°C) to 475 K (202°C) using the 3ω method show how second phase additions of ceramics with a higher thermal conductivity increase the thermal conductivity of 8YSZ. An 80% increase of thermal conductivity is observed for additions of 20 vol% alumina to 8YSZ in the measured temperature range. Comparison of the Maxwell Garnett, Bruggeman, and linear Rule of Mixtures models with 3ω measurements show the linear Rule of Mixtures is the most divergent from experimentation when predicting thermal conductivity of dilute two-phase composites. Error in the linear Rule of Mixtures model exceeded 100% in some cases, while the other two models were within 8% (Maxwell Garnett) and 2.5% (Bruggeman) of measurements. OOF2 simulations provided a good approximation (1.5 %) to the measured thermal conductivity. OOF2 has the advantage of incorporating the real microstructure morphology, although OOF2's two-dimensional nature may cause it to underestimate the real three-dimensional thermal conductivity. A dimensionless sensitivity analysis quantified a second shortcoming of the linear Rule of Mixtures, it is far too sensitive to variations in the thermal conductivity of the dispersed phase (k_2). On the other hand, the sensitivity of the three other calculations agree that the overall uncertainty in k_{eff} is determined primarily by the uncertainty in the matrix k_1, especially for the alumina composites with $k_2 >> k_1$.

4.6 Specific Acknowledgments

Co-authors of this work include: Zhaojie Wang from the University of California, Riverside, Chris Dames from University of California, Berkeley, and Martha L. Mecartney from the University of California, Irvine. This research was supported in part by a UC Discovery Grant. Dr. Stephen A. Langer at NIST is thanked for his assistance in using OOF2 simulations.

Chapter 5: Thermal Measurements and Computational Simulations of Three-Phase (CeO_2 - $MgAl_2O_4$ - $CeMgAl_{11}O_{19}$) and Four-Phase (3Y-TZP - Al_2O_3 - $MgAl_2O_4$ - $LaPO_4$) Composites as Surrogate Inert Matrix Nuclear Fuel

5.1 Abstract

This study investigates the temperature dependence thermal conductivity of multiphase ceramic composites for simulated inert matrix nuclear fuel. Fine grained composites were made of ceria, spinel, and Ce-magnetoplumbite (CeO_2 - $MgAl_2O_4$ - $CeMgAl_{11}O_{19}$) or yttria stabilized tetragonal zirconia, alumina, spinel, and monazite (3Y-TZP - Al_2O_3 - $MgAl_2O_4$ - $LaPO_4$). CeO_2 and 3Y-TZP are used as surrogates for UO_2 due to their similar structures and low thermal conductivities. After sintering in air for 3 hours at 1873 K (1600°C), laser flash analysis, dilatometry, and differential scanning calorimetry were used to determine the thermal diffusivity, coefficient of thermal expansion, and specific heat capacity, respectively, from room temperature to 1273 K (1000°C). Using these measurements, the experimental thermal conductivity of each composite was then calculated. Finally, Object Oriented Finite Element Analysis Version 2 (OOF2) was employed to simulate the composite thermal conductivity based on microstructural evaluation. A discrepancy between the experimental and simulated thermal conductivities is observed in the low temperature range of 373-673 K (100-400°C); however, there is less than a 3% deviation between the experimental and computational data above 673 K (400°C) for both compositions. Through OOF2, the surrogate phase was replaced with UO_2, creating a four-phase composite, which showed a 12-16% increase in thermal conductivity compared to single phase UO_2, within the range of 673-1273 K (400-1000°C). This approach is potentially viable for the high-throughput evaluation of composite fuel systems.

5.2 Introduction

The demanding operating conditions experienced by conventional uranium dioxide (UO_2) nuclear fuel can cause drastic microstructural changes and fracture during reactor operation [118]. Temperatures exceeding 1600 K (1326°C) caused by the low thermal conductivity of UO_2 (around 3 W/ m ·K at 1273 K (1000°C)) [37], create steep thermal gradients. These high temperatures induce restructuring exasperated by accumulation of fission gas bubbles and precipitation of solid fission products during burnup [119]. The development of complex microstructures not only challenges reactor performance modeling due to the conservatisms necessary in prediction of transport properties for such a complex system, but also can limit the permissible total burnup if swelling or mechanical degradation results.

To alleviate these problems, a fuel design where fissile and non-fissile phases are incorporated into a composite fuel is considered. Non-fissile phases can offer (i) increased thermal conductivity for the overall composite, (ii) crystalline phases that can accommodate fission by-products after their creation and (iii) decreased microstructural evolution by providing alternative interfaces that are more efficient sinks for point defects. Here, the fissile phase does not need to be the majority phase of the composite, although there will be a minimum fissile volume required that is governed by both the maximum feasible enrichment as well as the neutronic impact of the non-fissile phases.

Previous research has successfully demonstrated a two-phase fuel concept through the fabrication of a composite with a minority of nuclear fuel surrogate particles dispersed in an inert host matrix [39]. More recently, MgO – $Nd_2Zr_2O_7$ composites for inert matrix fuel were studied to evaluate the effects that phase content has on the thermophysical properties of the composite system [120]. Other pathways to improve thermal conductivity for inert matrix nuclear fuel have

also been studied using three phases, but with extremely large grains similar to those occurring naturally in rocks and minerals [121-122]. A key factor is that each phase must coexist without the formation of intermediate phases, and rock-like three-phase ceramic composite systems with fluorite, spinel, and corundum structures are reported to be compatible with both PuO_2 [121] and UO_2 [122-123] under irradiation.

In the present work, a 4-phase composite system consisting of 3Y-TZP (3 mol.% Y_2O_3 stabilized ZrO_2), Al_2O_3, $MgAl_2O_4$ and $LaPO_4$ and a 3-phase composite system consisting of CeO_2, $MgAl_2O_4$ and $CeMgAl_{11}O_{19}$ are fabricated. The 4-phase composition is the same as used in the work of Men *et al.* [124], where no amorphization was observed after Xe and Au ion irradiation of the composite. 3Y-TZP acts as a nuclear fuel surrogate (similar fluorite structure and low thermal conductivity), non-fissile phases such as Al_2O_3 and $MgAl_2O_4$ improve thermal stability at elevated temperatures, and $LaPO_4$ (monazite) is used for its capability to incorporate a wide variety of the radionuclides into a single-phase structure. The stability of monazite with corundum, spinel, and zirconia fluorite phases can be observed from geological deposits [125]. In the second ceramic composite, CeO_2 is used as an alternate surrogate for UO_2 (it also has the fluorite structure and low thermal conductivity), and spinel is included as the high thermal conductivity phase. The magnetoplumbite $CeMgAl_{11}O_{19}$ phase is an example of a potential evolution when phases are not stable with respect to one another at high temperatures, as it is produced by an undesirable reaction between initial starting compounds of corundum (α-Al_2O_3), spinel, and CeO_2. The relatively high thermal conductivity values of alumina and spinel compared to the other constituent phases and UO_2 can clearly been seen in Figure 5.1 [55; 71; 92; 126-127]. Since data on the thermal conductivity $CeMgAl_{11}O_{19}$ was unavailable at the time of this study, the temperature dependent thermal conductivity of $LaMgAl_{11}O_{19}$ was used instead.

The goals of this paper are to i) compare the temperature dependent thermal conductivities of each composite, ii) validate these experimental measurements with those generated by microstructural finite element analysis, and iii) simulate the incorporation of UO_2 for applications in composite nuclear fuel.

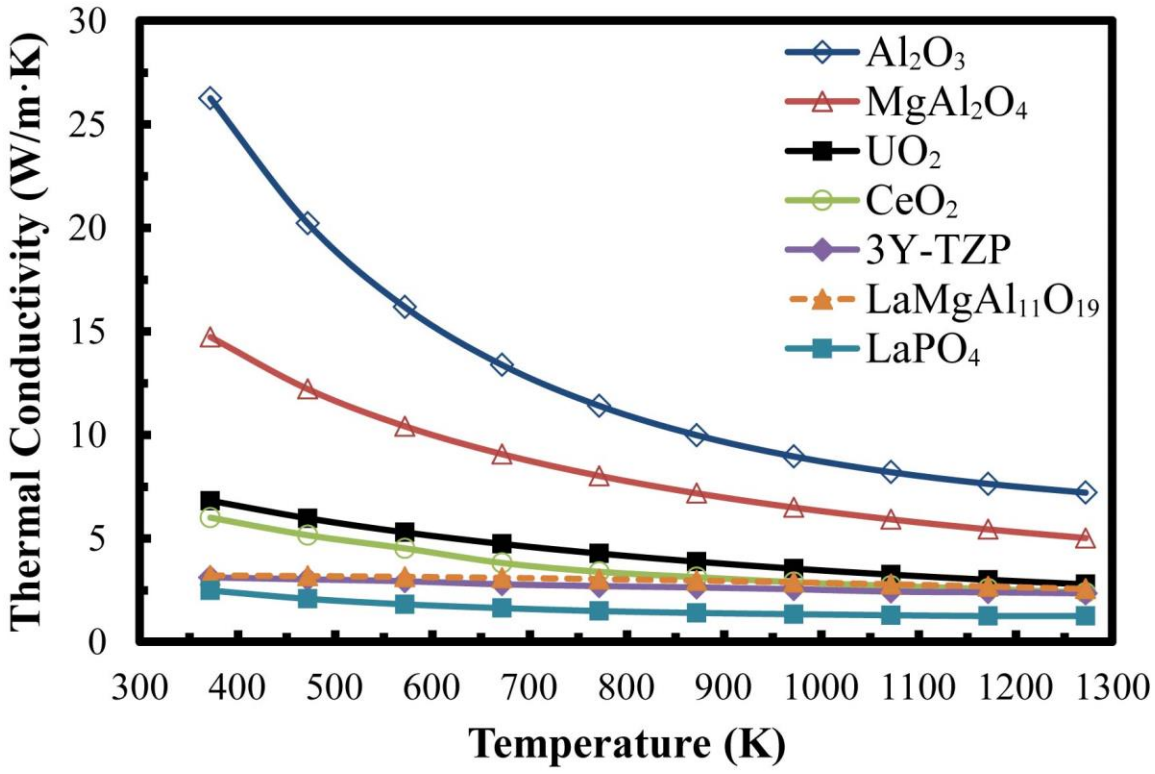

Figure 5.1 Temperature dependent single phase thermal conductivity values taken from literature for each component in both C-SMp and 3Y-ASM. (Al_2O_3[55] , $MgAl_2O_4$[126], UO_2[37], CeO_2{Andy's work}, 3Y-TZP[71], $LaMgAl_{11}O_{19}$[127] and $LaPO_4$[92])

5.3 Experimental Procedures

5.3.1 Sample Preparation and Characterization

Three-phase ceramic composites with the composition CeO_2-$MgAl_2O_4$-$CeMgAl_{11}O_{19}$ (abbreviated: C-SMp) were created by using starting powders of α-Al_2O_3 (Baikowski Inter. Corp., Charlotte, NC, crystallite size of 600 nm), $MgAl_2O_4$ (Baikowski Inter. Corp., Charlotte, NC, crystallite size of 200 nm), and CeO_2 (Sigma-Aldrich Co., St. Louis, Missouri crystallite size of 50 nm). Excess $MgAl_2O_4$ and CeO_2 were included to facilitate the reaction given by Eq. (5.1) for the in-situ formation of $CeMgAl_{11}O_{19}$ (Ce-magnetoplumbite).

$$9Al_2O_3 + 2MgAl_2O_4 + 2CeO_2 \rightarrow 2CeMgAl_{11}O_{19} \quad (5.1)$$

Powders were attrition-milled for 8 hours with 5 mm zirconia balls (Tosoh, Tokyo, Japan) in isopropanol, dried for 12 hours at 393 K (120°C), crushed with an agate mortar and pestle, and sieved through an 80μm mesh. Cylindrical samples were fabricated for microstructural characterization by cold isostatic pressing at 380 MPa for 5 minutes, followed by a sintering at 1873 K (1600°C) for 3 hours in air. This reaction occurs due to the Ce valence change from 4+ to 3+, which facilitates the formation of the magntoplumbite structure. Magneoplumbite has been proposed for nuclear waste host applications [128], and the unusual grain morphology provides an opportunity to study an asymmetric three phase material system.

Four-phase ceramic composites with the composition 3Y-TZP–Al_2O_3–$MgAl_2O_4$–$LaPO_4$ (abbreviated: 3Y-ASM) were created by using starting powders of 3 mol.% yttria tetragonal zirconia polycrystals (3Y-TZP, Tosoh, Japan, crystallite size of 50 nm), α-Al_2O_3 (same as above), $MgAl_2O_4$ (same as above), and $LaPO_4$ (lab made [54], crystallite size of 200-400 nm). Equal volume fractions of each phase were used. Powder processing steps and sintering was the same as above.

Relative density was measured using the Archimedes displacement method in accordance with ASTM B962-08 [129]. Distilled water was used as the immersion fluid, and the measurements were made using a beaker support positioned above the balance pan. Table 5.1 gives the compositional breakdown of each system.

Table 5.1 Volume fraction of each phase in respective composite systems, and single phase density taken from star quality powder diffraction file cards.

	Volume Fraction (%)	Density (g/cm^3)	Density Reference*
3-phase composite		4.988	
CeO_2	30	7.215	JCPDS no. 34-0394
$MgAl_2O_4$	25	3.579	JCPDS no. 21-1152
$CeMgAl_{11}O_{19}$	45	4.287	**
4-phase composite		4.751	
3Y-TZP	27	6.242	JCPDS no. 60-0503
Al_2O_3	25	3.984	JCPDS no. 46-1212
$MgAl_2O_4$	25	3.579	JCPDS no. 21-1152
$LaPO_4$	23	5.111	JCPDS no. 84-0600

*Joint Committee on Powder Diffraction Standards (JCPDS), **Calculated value.

X-ray diffraction (XRD) analysis was conducted with a Smart Lab X-ray Diffractometer (Rigaku, Tokyo, Japan) using Cu-k_α radiation (wavelength 0.15406 nm) to verify phases and compositions. Scans consisted of 0.05° steps from 20° to 90° using Bragg-Brentano optical conFigureuration. Scanning electron microscopy (SEM) was performed using a FEI XL 30 FEG (FEI, Eindhoven, The Netherlands). To prevent electrical charging during SEM analysis, a thin film of iridium was deposited onto the sample surface using an IBS/e Ion Beam Sputter Deposition System (South Bay Technology, San Clemente, CA). Chemical compositions were identified by energy-dispersive x-ray spectroscopy (EDS) performed with a $50mm^2$ detector (Oxford Instruments).

5.3.2 Thermal Measurements

The thermal conductivity, $\kappa(t)$, for each composite is calculated using the relationship:

$$\kappa(t) = \alpha(t) \cdot c_p(t) \cdot \rho(t) \quad (5.2)$$

where $\alpha(t)$ is thermal diffusivity, $c_p(t)$ is specific heat capacity and $\rho(t)$ is density. Each parameter is determined separately over the temperature range of 373-1273 K (100-1000˚C). Thermal diffusivity of the sintered samples was measured under ultra-high purity Ar using a laser flash apparatus (Netzsch 457 LFA, Germany). Prior to measurement, both the top and the bottom surfaces of each sample were coated with a thin layer of colloidal graphite to enhance the absorption of the laser. The specific heat capacity of each sample as a function of temperature was measured using differential scanning calorimeter (Netzsch 404 F1 DSC, Germany). Samples were analyzed in ultra-high purity Ar at a heating rate of 20°C/min in an alumina-lined Pt crucible. Heat capacity was calculated during dynamic heating using the ratio method with sapphire as the reference. The temperature dependent linear thermal expansion and density of each sample were measured using push-rod dilatometery (Netzsch 402 CD, Germany). Samples were tested under ultra-high purity Ar at a heating rate of 5°C/min using an alumina reference standard.

5.3.3 OOF2 Simulations

Object-oriented finite-element analysis version 2 (OOF2) [60-61], an open access software developed at the National Institute of Standards and Technology (NIST), is used for these simulations due to its capability to account for size, shape, and distribution of each phase within the microstructure. Two-dimensional SEM micrographs were converted to multi-color images in post-processing. Each phase, identified by backscattered phase contract and EDS, was represented by a single color in order to create finite-element meshes adapted to the microstructure of the material, and were assigned their appropriate single phase material

property. Input values for the thermal conductivity as a function of temperature for each component were taken from experimental results on single-phase materials, as shown in Figure 5.1.

A thermal gradient was simulated in the vertical direction of the image by assigning a 10 degree difference between the top and bottom boundaries, and keeping the sides adiabatic. The heat equation was solved by the conjugate gradient method and each node of the mesh was assigned an x and y heat flux component. By setting the out-of-plane (z) heat flux components to zero, OOF2 removed the third dimension from the problem; this is analogous to plane-stress analysis used in fracture mechanics. The resulting 2D heat flux was integrated along a boundary of the image and used to determine the effective thermal conductivity:

$$k_{eff} = \frac{L_y Q}{L_x\left(T_{bottom} - T_{top}\right)} \tag{5.3}$$

where k_{eff} is the effective thermal conductivity of the composite, Q (watts per meter of thickness in z) is the OOF2 heat flux integrated across the bottom boundary, L_y and L_x are the image dimensions, and T_{bottom} and T_{top} are the temperature values assigned to the bottom and top boundaries. The effective thermal conductivity of the composite was determined by simulating a thermal gradient across an image at various temperatures ranging from 373-1273 K (100-1000˚C). Three representative SEM micrographs were used for each composition, and the typical variability between each simulation of the same composition was less than 1%.

5.4 Results and Discussion

5.4.1 Phase and Microstructure Characterization

Figure 5.2 shows the x-ray diffraction (XRD) patterns of both 3-phase (C-SMp) and 4-phase (3Y-ASM) composites. Overlapping of peaks was minimal for the C-SMp system (Figure 5.2a), allowing for each phase to be easily indexed. CeO_2 and $MgAl_2O_4$ were indexed using JCPDS no. 34-0394 and 21-1152 respectively, while $CeMgAl_{11}O_{19}$ was indexed using the $LaMgAl_{11}O_{19}$ pattern, JCPDS no. 70-6968, since there is currently no star quality mark pattern for $CeMgAl_{11}O_{19}$ in the International Centre for Diffraction Data (ICDD) database. Numerous overlapping peaks in the 3Y-ASM system (Figure 5.2b) resulted in the indexing of only the major peaks for each phase. The existence of monoclinic ZrO_2 (m-ZrO_2) can be seen in the 3Y-ASM x-ray diffraction pattern due to partial transformation from tetragonal ZrO_2 (3Y-TZP) to the monoclinic structure. Al_2O_3, $LaPO_4$, m-ZrO_2 and 3Y-TZP were indexed using JCPDS no. 46-1212, 84-0600, 37-1484 and 60-0503 respectively.

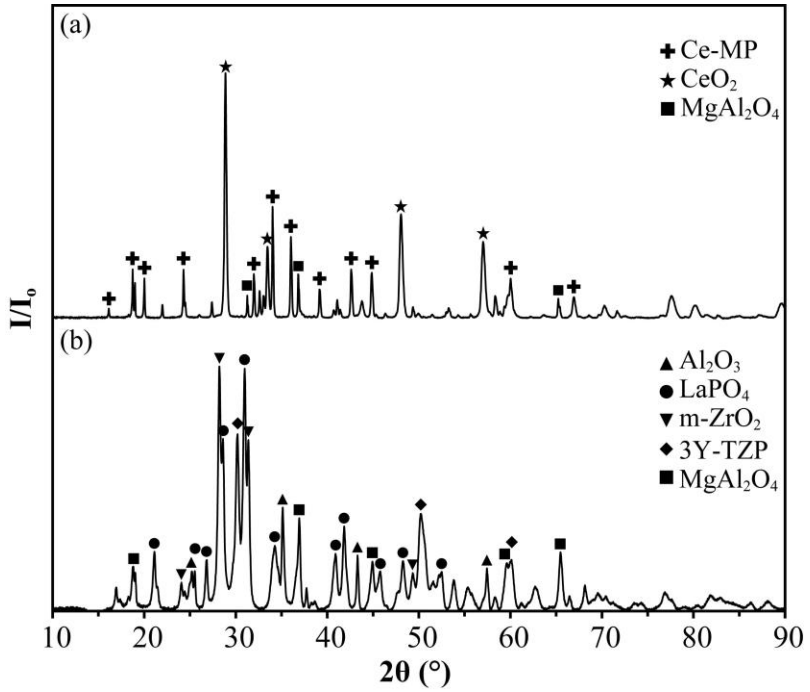

Figure 5.2 X-ray diffraction spectrum of (a) C-SMp and (b) 3Y-ASM composites. The presence of both 3Y-TZP and monoclinic zirconia (m-ZrO_2) was seen in 3Y-ASM.

The surface morphology of each composite observed by SEM is shown in Figure 5.3 for representative microstructures of the C-SMp and 3Y-ASM samples. In Figure 5.3a, the dark phase corresponds to $MgAl_2O_4$ spinel, the light phase is CeO_2, and the elongated acicular grains are $CeMgAl_{11}O_{19}$. This asymmetrical grain growth seen in $CeMgAl_{11}O_{19}$ is due to the anisotropic tetragonal crystal system with a **c** direction lattice parameter that is more than twice as large as the **a** direction lattice parameter, as well as the preferred growth occurring in the **c** direction. Figure 5.3b shows a representative microstructure of the 3Y-ASM composite. The dark phases are Al_2O_3 or $MgAl_2O_4$, the gray phase is $LaPO_4$ and the light phase is 3Y-TZP. The similar density of Al_2O_3 and $MgAl_2O_4$ make phase identification through phase contrast alone difficult. For this reason, energy-dispersive x-ray spectroscopy (EDS) was performed on each grain in the image to determine its chemical composition (EDS analysis was also performed on the C-SMp composite to ensure correct phase identification). Although the presence of some m-ZrO_2 was observed in the XRD pattern for the 3Y-ASM composite, identification between the zirconia polymorphs proved unreliable by EDS and zirconia grains were assumed to be 3Y-TZP during computationally analysis (reasoning for this is discussed below).

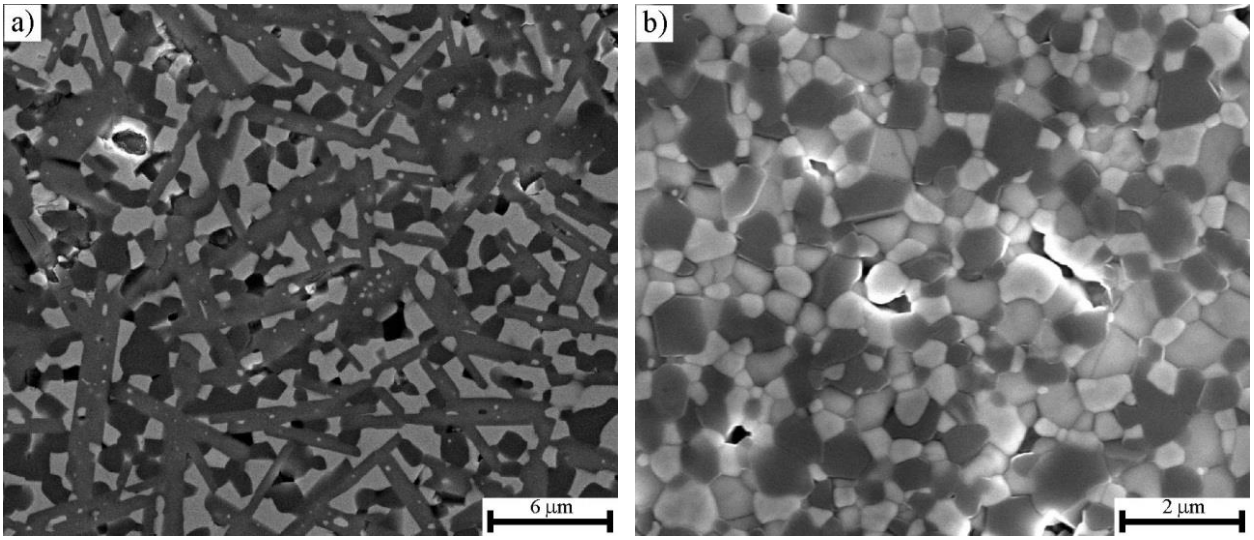

Figure 5.3 Scanning electron microscope image in backscatter electron mode of a) 3-phase composite where Mg-spinel is the dark phase, Ce-MP is the gray phase and CeO_2 is the light phase, and b) 4-phase composite where Mg-spinel and Al_2O_3 are the dark phases, $LaPO_4$ is the gray phase and 3Y-TZP the light phase. Energy-dispersive x-ray spectroscopy is used to differentiate each phase.

5.4.2 Thermal Measurements

The technical coefficient of thermal expansion (CTE) and density of C-SMp and 3Y-ASM composites, measured as a function of temperatures ranging from 373-1273 K (100-1000˚C), are shown in Figure 5.4. Data collected near room temperature suffered from high errors due to temperature gradients that developed during initial heating of the sample and were discarded. Typical monotonic behavior for both the CTE and density as temperature increased was observed for C-SMp. In the 3Y-ASM composite, a discontinuity occurred in both the CTE and density within the temperature range of 923-973 K (650-700˚C). This sudden jump in the CTE and density is usually an indication of a phase change. Upon cooling, the tetragonal to monoclinic phase transformation occurs at 1443 K (1170°C) for pure ZrO_2. Lower temperature transformations can occurs due to yttria doping and mechanical constraints of the stiff matrix formed by the composite. Figure 5.4b shows this sudden increase in density at the discontinuity, which coincides with the transformation of any included monoclinic (ρ=5.817 g/cm^3) to

tetragonal (ρ=6.343 g/cm^3) zirconia. The presence of both zirconia polymorphs is seen in the XRD data of Figure 5.2, suggesting that some of the 3Y-TZP transforms to monoclinic upon cooling after the sintering process and transformed back to tetragonal 3Y-TZP upon re-heating.

Figure 5.5 shows the thermal diffusivity and heat capacity for each composite system. For both compositions, the thermal diffusivity decreases monotonically as temperatures increase up to 1273 K (1000˚C), reaching values of 0.87 mm^2/s and 0.84 mm^2/s for C-SMp and 3Y-ASM, respectively. Similar to Figure 5.4b, a discontinuity in the heat capacity of 3Y-ASM was observed within the temperature range of 923-973 K (650-700˚C), which is an artifact due to the zirconia phase transformation. No discontinuity was seen for the thermal diffusivity of 3Y-ASM. These discontinuities can be explained by the monoclinic to tetragonal phase transformation, where the continuous decrease in the thermal diffusivity is likely due to thermal transport being limited by the monazite, which is the most insulating phase.

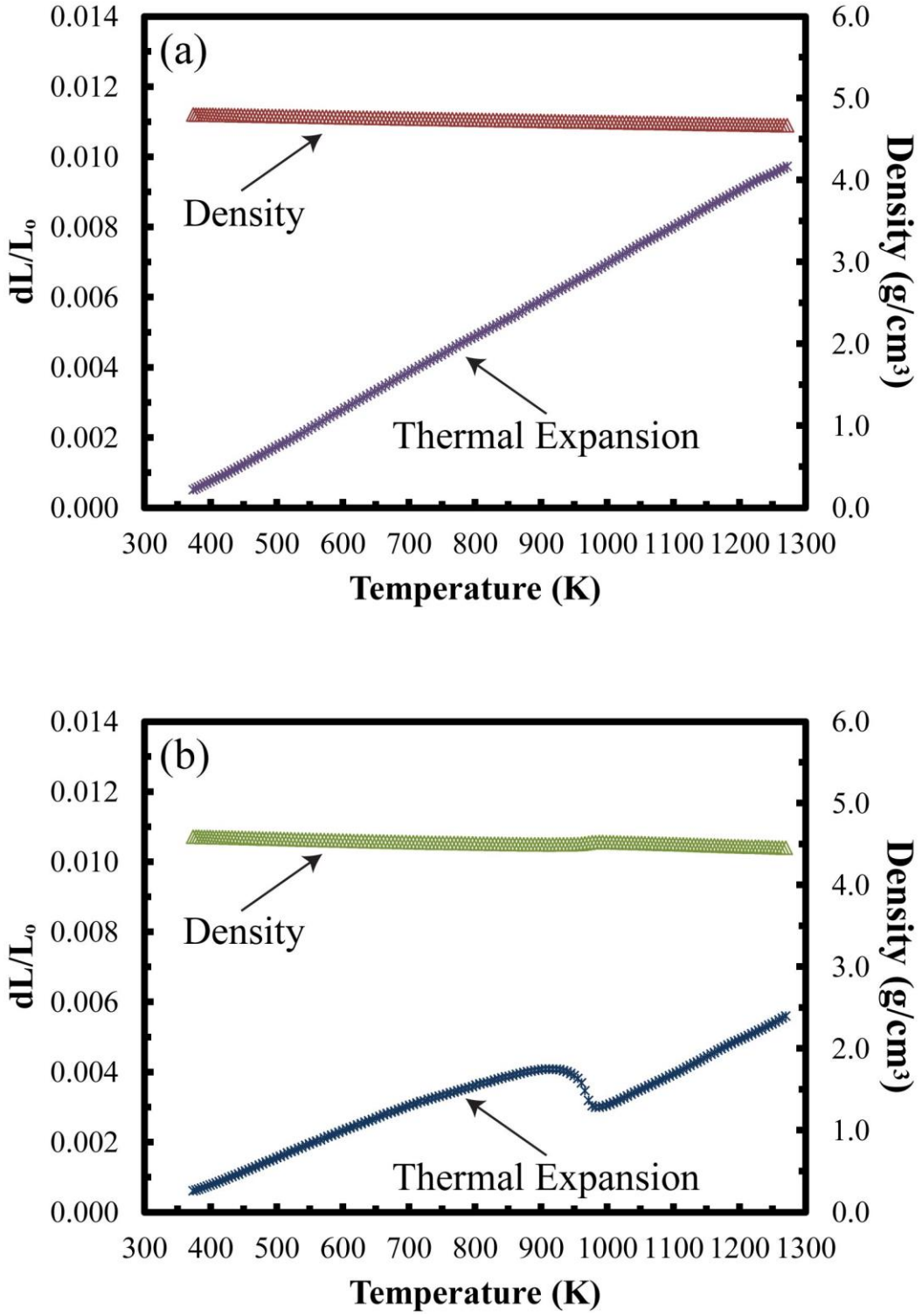

Figure 5.4 Density (left axis) and coefficient of thermal expansion (right axis) measured over a temperature range of 373-1273 K (100-1000˚C) for (a) C-SMp and (b) 3Y-ASM.

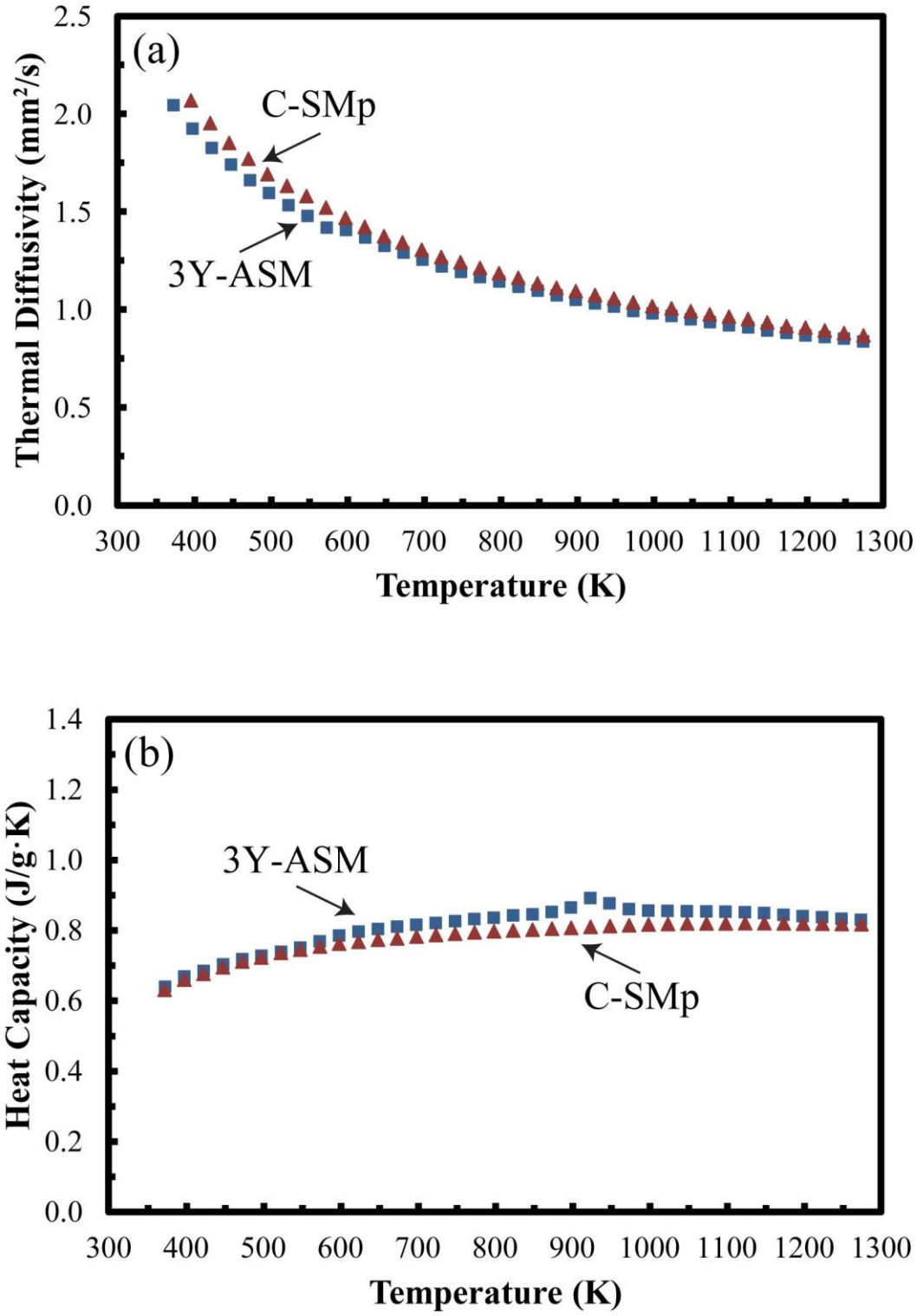

Figure 5.5 (a) Thermal diffusivity and (b) heat capacity measured over a temperature range of 373-1273 K (100-1000˚C) for C-SMp and 3Y-ASM.

The thermal conductivity as a function of temperature for C-SMp and 3Y-ASM composite systems is shown in Figure 5.6. For both systems, the thermal conductivity decreases as temperature decreases. 3Y-ASM has a higher thermal conductivity at lower temperatures than the C-SMp system (25% higher at 373 K (100˚C)), but begins to converge with C-SMp as temperature increases (only a 5% greater thermal conductivity at 1273 K (1000˚C), falling within the 5% error of the measurement). This effect is primarily due to the Al_2O_3 phase in 3Y-ASM sharply decreasing in thermal conductivity. The discontiunites observed in the density and specific heat capacity from 923-973 K (650-700˚C) for 3Y-ASM does not affect the thermal conducivity calculated by Eq. (5.2). This indicates that the large decrease in thermal diffusivity is the dominant factor controlling the lower thermal conductivity with increasing temperature.

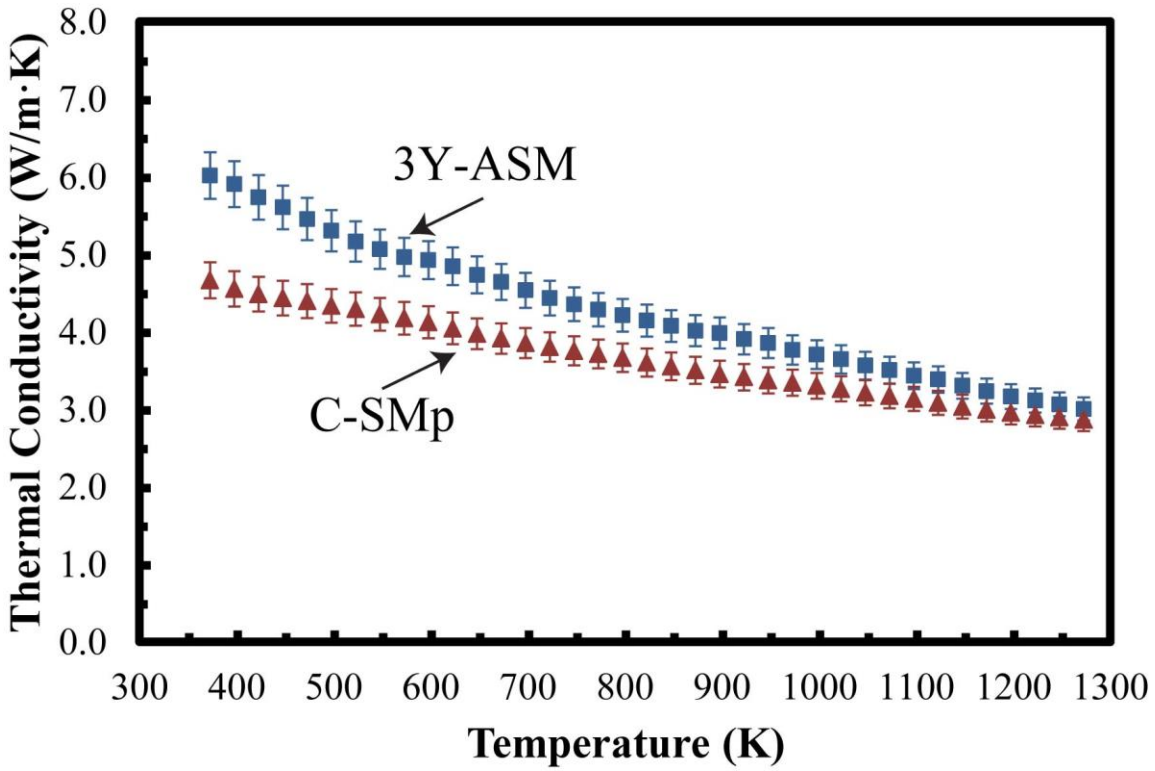

Figure 5.6 Thermal conductivity of C-SMp and 3Y-ASM calculated by the laser flash method over a temperature range of 373-1273 K (100-1000˚C).

5.4.3 OOF2 Simulations

Single phase temperature-dependent thermal conductivity values, taken from Figure 5.1, were inputted into OOF2 software along with a solid color representation of a SEM micrograph in order to approximate the effective thermal conductivity for each composite system. Figure 5.7a shows the color representation of the original SEM image of C-SMp from Figure 5.3a. An adaptive mesh was fitted to the grain boundary interface of each phase (Figure 5.7b), where a finer mesh and higher node density can be seen along the phase interface. After the simulation, a heat flux map was generated (Figure 5.7c), showing regions of high and low heat flux. Aside from the porosity, $CeMgAl_{11}O_{19}$ appears to be the phase with the lowest heat flux, which is expected due to its low thermal conductivity. The temperature-dependent thermal conductivity of air, which ranges from 0.023 W/m·K at 300 K to 0.083 W/m·K at 1300 K [130], was used for the thermal conductivity of porosity. Considering that porosity makes up <2% of the composite, it can be assumed to have a negligible contribution to the overall heat conduction.

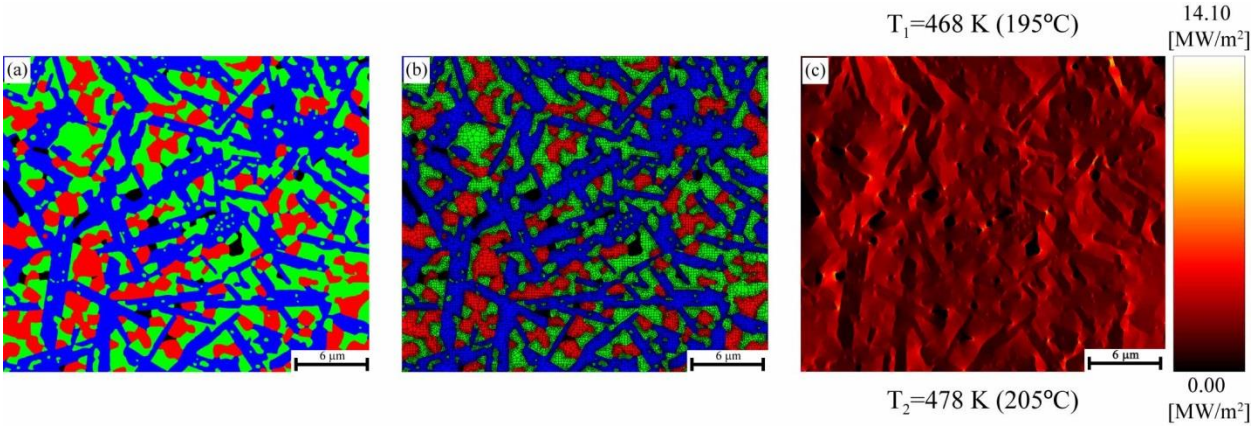

Figure 5.7 OOF2 images of the C-SMp composite shown in Figure 5.3a (a) color representation of the microstructure, (b) finite element meshing, and (c) heat flux map generated by the simulation. Al_2O_3 is represented by red, $CeMgAl_{11}O_{19}$ blue, CeO_2 green and porosity black.

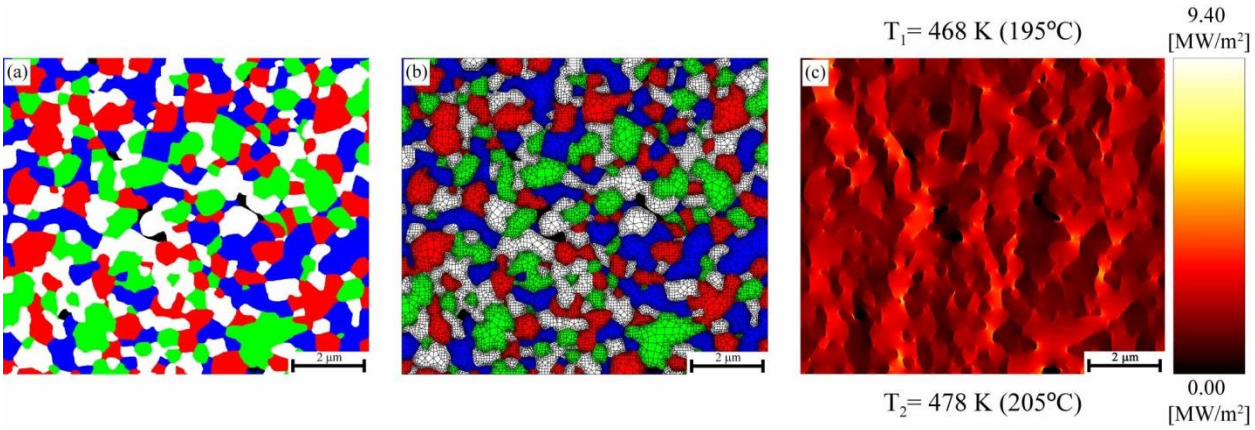

Figure 5.8 OOF2 images of 3Y-ASM composite shown in Figure 5.3b (a) color representation of the microstructure, (b) finite element meshing, and (c) heat flux map generated by the simulation. $MgAl_2O_4$ is represented by red, $LaPO_4$ blue, Al_2O_3 green, 3Y-TZP white and porosity black.

Figure 5.8 depicts a similar set of images as Figure 5.7 for the 3Y-ASM composite system. Blocking of heat flux pathways are observed in Figure 5.7c due to the irregular acicular elongated particle morphology of the $CeMgAl_{11}O_{19}$ phase. This magnetoplumbite phase is the lowest thermal conductivity phase in this system, and this particle morphology prevents the higher thermal conductivity phase of alumina from forming an interconnected network. Although each phase is above the percolation limit, and interconnected pathways are not present in the 2D representation of the microstructure, that does not rule out the existence of percolation pathways in 3D.

In contrast, Figure 5.8c clearly shows heat flow pathways formed between the higher thermal conductivity phases, i.e. Al_2O_3 and $MgAl_2O_4$. These pathways are a result of all phases being above the percolation limit, an even distribution of each phase, and a uniform grain morphology seen in the microstructure. Figure 5.9 shows how Al_2O_3 and $MgAl_2O_4$ grains, along with small regions of 3Y-TZP, create a pathway for heat flow from the bottom of the image to the top. This contiguity of highly conducting phases allows the composite to maintain an overall high thermal

conductivity despite having 25 vol % $LaPO_4$, which is well known for its extremely low thermal conductivity.

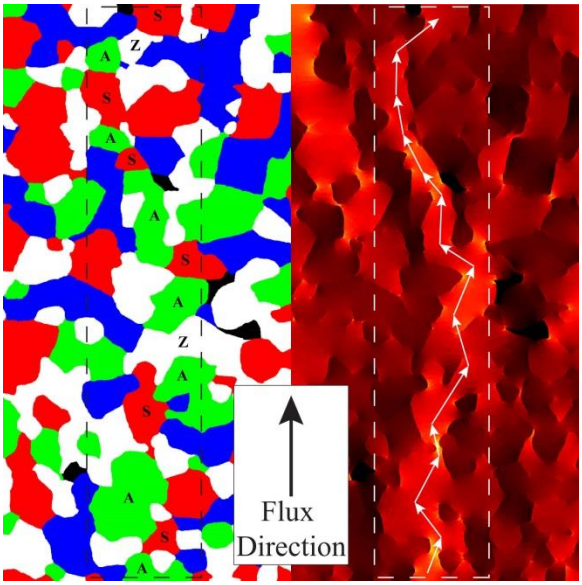

Figure 5.9 Heat flux pathway formed by network of highly conducting Al_2O_3 (A) and $MgAl_2O_4$ (S) grains, along with small regions of 3Y-TZP (Z) gains.

5.4.4 Surrogate Comparison

The simulated thermal conductivity of C-SMp and 3Y-ASM via OOF2 was compared to the experimentally determined thermal conductivity (from Figure 5.6) and are shown in Figure 5.10. A discrepancy between the experimental and simulated thermal conductivities for C-SMp is observed at the low temperature range 373-673 K (100-400°C), while above 673 K (400°C) the two data sets are convergent. Similarly, a low temperature discrepancy is observed in 3Y-ASM. For the C-SMp composite, a difference of 9.1% at 373 K (100°C) and 1.1% at 1273 K (1000°C) was measured between the laser flash method (LFM) and OOF2. In comparison, the 3Y-ASM composite showed a difference of 17.6% at 373 K (100°C) and 0.3% at 1273 K (1000°C). One aspect that may contribute to the greater deviation of the 3Y-TZP compared to C-SMp at low temperatures is the approximation that was made in the simulation that the 3Y-TZP is completely

tetragonal zirconia. Above 673 K (400°C), the percent difference between LFM and OOF2 is <3% for both composite systems, which falls with the standard 5% error of the measurement.

However, the disagreement between the experimental and computational results at low temperatures for both systems could be partially due to the Kapitza interfacial resistance between two phases, which was not taken into consideration in the OOF2 simulations. This would affect the models in two ways. First, the Kapitza resistance is higher at lower temperatures, which could contribute to the low temperature discrepancy. Second, the Kapitza is also typically higher for interfaces between dissimilar phases [131]. Work is currently underway incorporate grain boundary and interface effects into the OOF2 simulations.

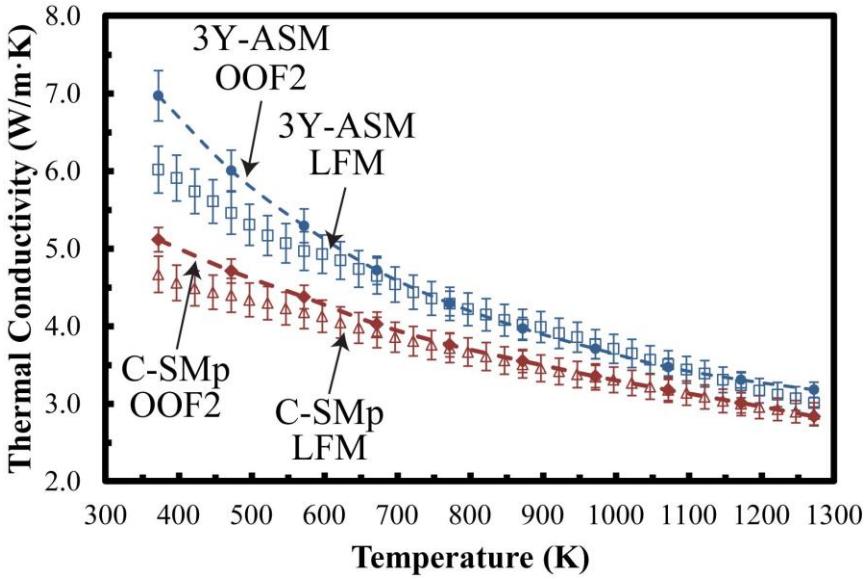

Figure 5.10 Thermal conductivities simulated by OOF2 and measured through the laser flash method (LFM) for C-SMp and 3Y-ASM. A good agreement between both methods is observed at temperatures above 400°C.

Hypothetical composites, labeled U-SMp and U-ASM for the 3-phase and 4-phase compositions, respectively, were simulated. The UO_2 single phase thermal conductivity values replaced CeO_2 in the C-SMp composite, and 3Y-TZP in the 3Y-ASM composite. The thermal conductivity over the temperature range 373-1273 K (100-1000˚C) for the two hypothetical composites was determined by OOF2 using the same procedures described above. Figure 5.11

shows the results of the OOF2 simulations and includes the thermal conductivity of single phase UO_2 for comparison. U-SMp had an even lower thermal conductivity than single phase UO_2 from 373-973 K (100-700˚C), and less than a 6% increase in thermal conductivity compared to pure uranium oxide above 973 K (700°C). The non-uniform morphology and low thermal conductivity of $CeMgAl_{11}O_{19}$ is clearly detrimental to overall thermal conductivity of the composite system. In contrast, the composite UO_2-Al_2O_3-$MgAl_2O_4$-$LaPO_4$ had a 12-16% increase in thermal conductivity from 673-1273 K (400-1000˚C) compared to single phase UO_2. Even in this case, the use of the extremely low thermal conductivity $LaPO_4$ phase limits the magnitude of the increase in conductivity, and therefore a composition with alternate phases to monazite is currently being evaluated.

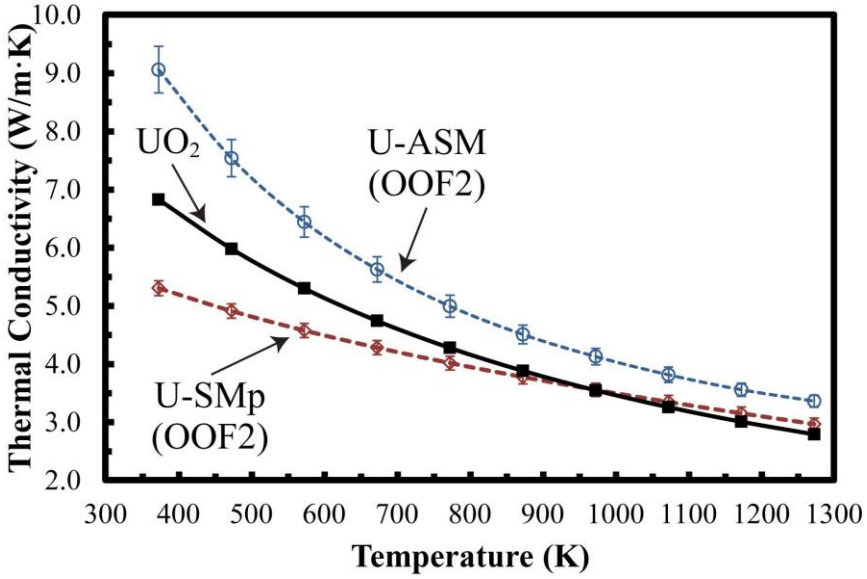

Figure 5.11 OOF2 simulated composites where UO_2 is substituted for CeO_2 in C-SMp (U-SMp) and 3Y-TZP in 3Y-ASM (U-ASM). A single phase thermal conductivity of UO_2 is shown for comparison.

5.5 Conclusions

In this paper, inert matrix 3-phase and 4-phase ceramic composites to be used as surrogate nuclear fuels were prepared and characterized using CeO_2 or 3Y-TZP as surrogate phases for UO_2. Thermal properties such as temperature dependent density, thermal expansion coefficient, specific heat capacity, thermal diffusivity and thermal conductivity were reported for each system. Computational simulations using OOF2 were used to calculate the effective thermal conductivity and showed good agreement with experimental methods within the error of the experimental technique at temperatures above 673 K (400°C) for both composite systems. The ability to predict the thermal behavior of UO_2 incorporated nuclear fuel composites, without the need for synthesis of a diverse set of sample compositions, makes this approach valuable to screen non-fissile material candidates and to construct various microstructural designs.

5.6 Specific Acknowledgments

Co-authors of this work include: Andrew T. Nelson from Los Alamos National Laboratory, and Danju Men and Martha L. Mecartney from the University of California, Irvine. This research is supported by the U.S. Department of Energy funding under grant DE-NE0000711. Some of the materials were developed under an NSF DMR 0606063 grant. The views and opinions of authors expressed herein do not necessarily state or reflect those of the United States Government or any agency thereof.

Chapter 6: Water Vapor Enhanced Diffusion in Alumina

6.1 Abstract

Experimental results indicate effective faster diffusion of oxygen in alumina exposed to water vapor at high temperatures. Polycrystalline α-Al_2O_3 containing Ni metal particles was exposed to either dry air or humid environments at 1573 K (1300°C) for up to 20 hours. Oxidation of Ni in α-Al_2O_3 to form $NiAl_2O_4$ was used to determine oxygen diffusion depth from the surface. The apparent kinetic rate-constant for oxygen diffusion in the presence of water vapor was 79% higher compared to that of a dry atmosphere at 1573 K (1300°C) ($1.4x10^{-13}$ m^2/s for 0.2 atm P_{H_2O} versus $7.9x10^{-14}$ m^2/s for dry air). (OH^-) ions are smaller, have a lower charge than (O^{2-}), and are more polarizable, which would be expected to lead to faster diffusion. This effect may impact sintering, creep, corrosion, oxidation, and the performance of thermal barrier coatings (TBC).

6.2 Introduction

The controlling mechanism in many ceramic processes is grain-boundary diffusion, which in alumina is greatly diminished in the presence of certain cations, e.g. reducing creep rates [132] or slowing TBC bond coat oxidation [133]. One might wonder if there are *anion impurities* or the equivalent which actually enhance grain boundary diffusion; (OH^-), which can be up to 20% smaller than (O^{2-}) [52], comes naturally to mind. It is well known that oxide surfaces easily adsorb water, forming superficial (OH^-). There are numerous reports of accelerated reaction kinetics, more rapid coarsening/grain growth, and faster densification for ceramic oxides in the presence of high temperature water vapor [41; 43-44; 46; 134].

Herein we offer an experiment to test if water vapor has an effect on grain boundary diffusion of oxygen in a technologically relevant ceramic, viz. α-Al_2O_3. Alumina is used for many high temperature structural applications and is produced as a thermally-grown oxide (TGO) at metallic bond coats for thermal barrier coatings on Ni-based turbine blades. Most experiments on α-Al_2O_3 show oxygen is the slower diffusing ion compared to aluminum [135]. In this experiment, Ni-particles are embedded in a dense α-Al_2O_3 matrix [36; 136-137] and subsequently exposed to an oxidizing environment. The oxidation of Ni via formation of $NiAl_2O_4$ is measured in dry and humid oxidizing environments at elevated temperatures, and correlated to oxygen diffusion values.

6.3 Experimental Procedures

High-purity α-alumina powder (Baikowski Inter. Corp., Charlotte, NC) and nickel oxide powder (Alfar Aesar, Ward Hill, MA) were milled, dried, sieved, then heated at 973 K (700°C) for 5 hours in 4% H_2-Ar at a flow rate of 50 cm^3/min to reduce NiO to elemental Ni. Cylindrical specimens were cold isostatic pressed at 380 MPa and sintered at 1773 K (1500°C) for 3 hours in a reducing environment of 4% H_2-Ar. Density was measured by Archimedes method. Sintered samples were polished to a 0.1 μm finish. Oxidation at 1573 K (1300°C) was conducted for 5, 10, 15 or 20 hours. Ultra-pure zero grade dry air was used for dry oxidation, while bubbling dry air through a water bath created water vapor, with a flow rate for both of 50 cm^3/min. By adjusting the temperature of the water bath, the water vapor partial pressure was varied from 0.2 atm P_{H2O} to 0.83 atm P_{H2O}.

X-ray diffraction (XRD) analysis with a SmartLab X-ray Diffractometer (Rigaku, Tokyo, Japan) used Cu-k_α radiation and scans steps of 0.05° from 20° to 90°. Scanning electron microscopy (SEM) and energy dispersive spectroscopy (EDS) was performed on a Magellan 400 (FEI, Eindhoven, The Netherlands). Grain size was measured using ImageJ (NIH, Bethesda, Maryland). Backscatter electron imaging was used to differentiate between nickel aluminate spinel ($NiAl_2O_4$) and unreacted Ni and to measure the oxidation depth *x*. To obtain an average depth of oxidation value for each sample, at least 1 mm parallel to the surface was imaged and measured in increments of 100 μm along the surface with a depth of 150 μm.

6.4 Results and Discussion

While α-Al_2O_3 and NiO are the only phases in the initial powder, Ni is formed and NiO peaks disappear after reduction (Figure 6.1). The sintered compacts retain Ni metal but subsequent oxidation forms $NiAl_2O_4$ (Figure 6.1(d)) in regions near the surface probed by XRD. The d-spacings for α-Al_2O_3 do not change, correlating with limited solid solubility of Ni in bulk alumina [138].

Density of the sintered α-Al_2O_3/0.5 vol% Ni was 97-98% theoretical density (4.07 g/cm^3). The average alumina grain size is 1.2 ± 0.5 μm. There is a reasonably homogeneous distribution of Ni particles throughout the α-Al_2O_3 matrix prior to oxidation (Figure 6.2(a)), with submicron Ni particles typically located at α-Al_2O_3 grain boundaries (Figure 6.2(b)).

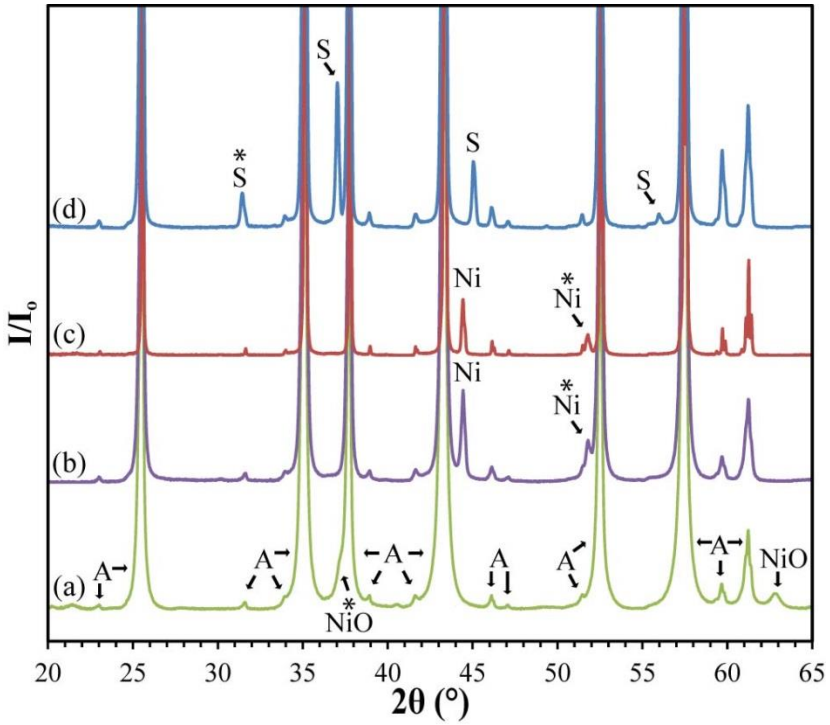

Figure 6.1 XRD pattern of (a) milled Al_2O_3 + NiO powder before reduction, (b) Al_2O_3 + 0.5 vol% Ni powder after reduction, (c) sintered Al_2O_3 + 0.5 vol% Ni sample and (d) a sample exposed to dry oxidation for 20 hours at 1573 K. (**A**=Al_2O_3, **S**=$NiAl_2O_4$ spinel and * signifies an overlap with Al_2O_3)

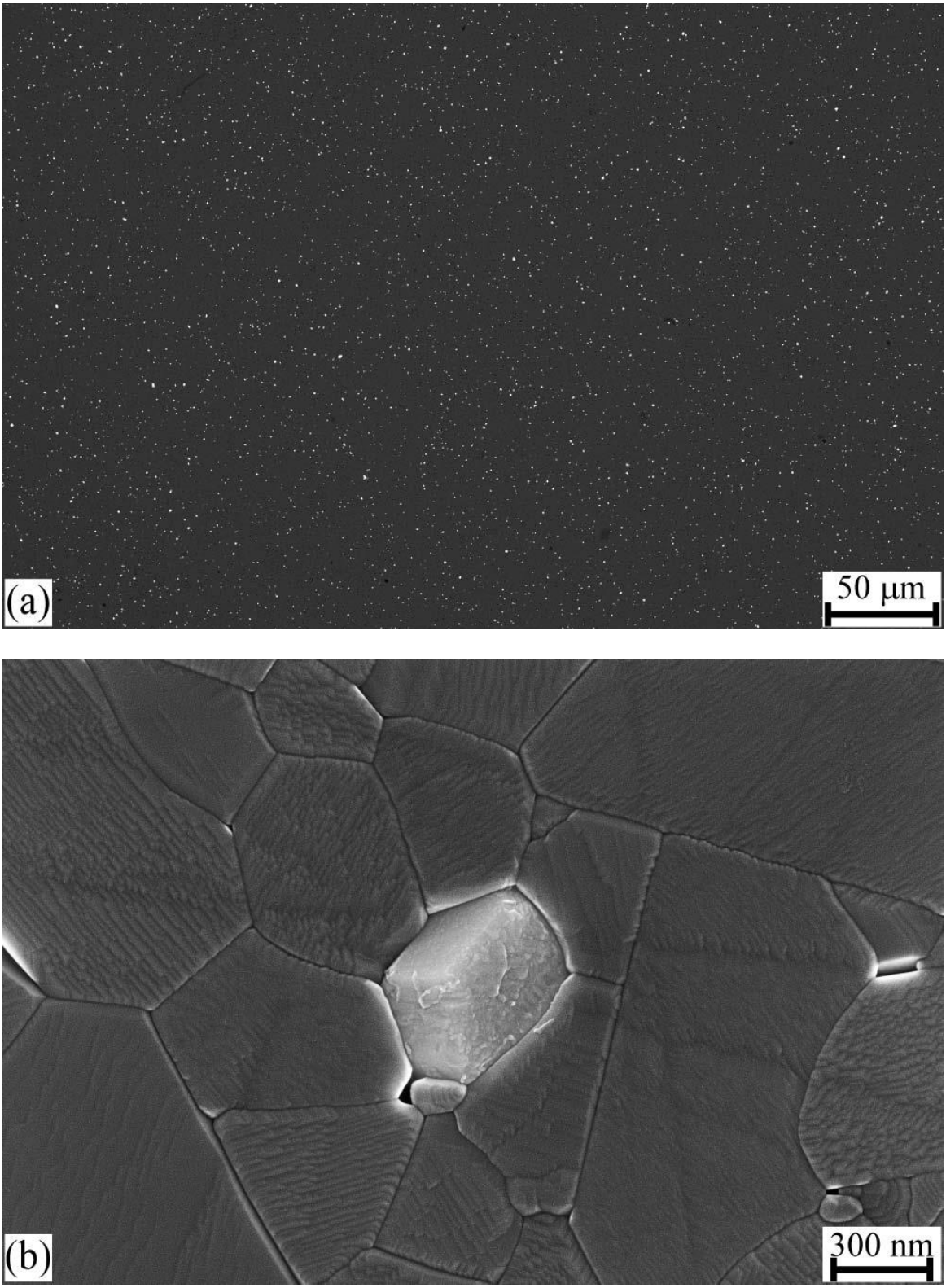

Figure 6.2 SEM (a) backscattered electron image at low magnification showing random distribution of Ni particles and (b) secondary image showing a Ni particle in Al_2O_3.

Figureure 6.3 compares oxidation depths in dry and humid environments. The difference in oxygen chemical potential between the surface and the interior drives oxygen inward and oxidizes the Ni, producing $NiAl_2O_4$. The depth of Ni-spinel formation acts as a measurement of oxygen grain boundary diffusion. When water vapor is present, there is a significant increase in oxidation depth for Ni-spinel formation for the same time and temperature (Figure 6.3). For example, after 5 hours at 1573 K (1300°C), the oxidation depth is 43% greater for humid oxidation (0.2 atm P_{H_2O}) versus dry air.

A depleted zone between the Ni and $NiAl_2O_4$ zones (Figure 6.3(a)) was often observed and these regions had a lower overall Ni concentration determined by EDS, while oxidized regions with spinel formation had higher concentrations of Ni than in the bulk. The depletion zone is irregular and more obvious in dry air samples. The presence of this depleted zone implies faster outward diffusion of Ni than inward diffusion of oxygen, as also documented by researchers studying Ni diffusion through TGO alumina in TBCs [139].

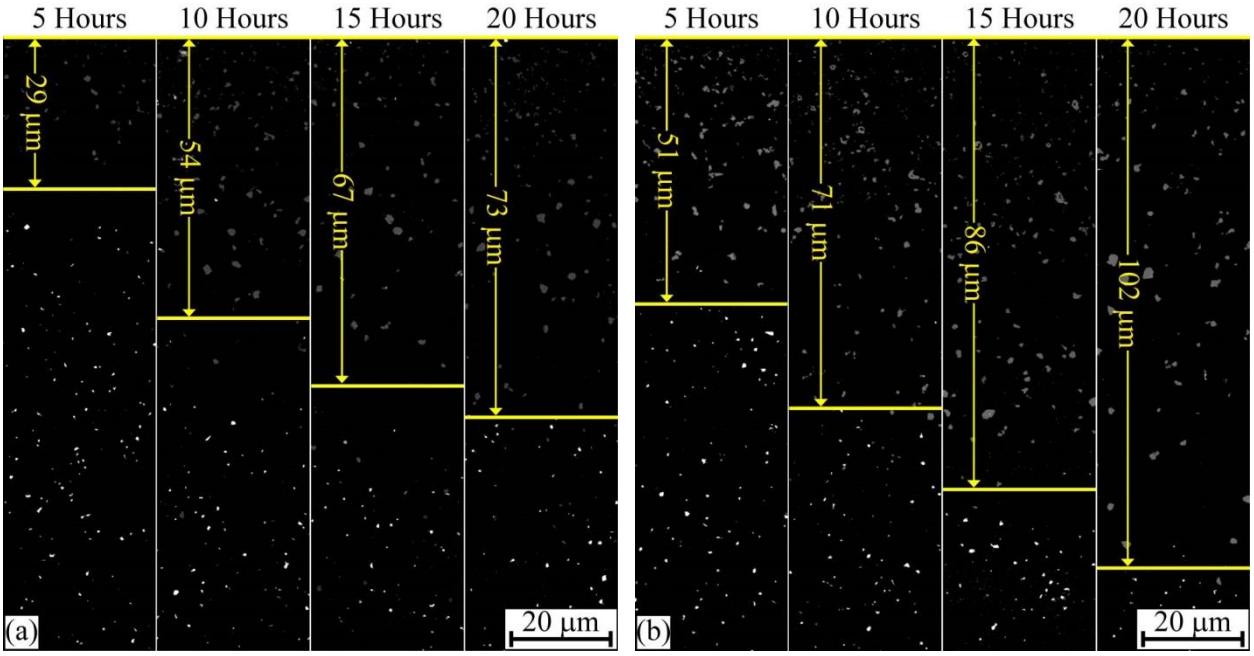

Figure 6.3 Average depth of oxidation *x* from top free surface for the time lengths of 5, 10, 15 and 20 hours at 1300°C under (a) dry and (b) humid (0.2 atm P_{H_2O}) atmospheres.

The square of the average oxidation depth is plotted against annealing time in Figure 6.4. The depth of oxidation is an averaged value between the end depth for formation of $NiAl_2O_4$ particles and the beginning depth for residual unoxidized Ni particles. A parabolic rate law is used to model the diffusion-controlled reaction processes to form spinel in order to determine oxidation kinetics. The kinetic rate constants are calculated by determining the slope of each line. The rate constant for dry oxidation at 1573 K (1300°C) was $k_{dry}= 7.93x10^{-14}$ m^2/s, within 8% of the value reported previously at that temperature for oxidation of Ni in alumina forming spinel in air [36]. The rate constant for each level of humidity was $k_{0.2\ atm\ PH2O} = 1.42x10^{-13}$ m^2/s and $k_{0.83\ atm\ PH2O} = 1.46x10^{-13}$ m^2/s. The negligible difference in oxidation depth for 0.2 atm P_{H2O} and 0.83 atm P_{H2O} suggests that 0.2 atm P_{H2O} is close to the saturation point for incorporation of hydroxyl ions. Such saturation has also been observed for TBC lifetime reduction in humid environments [139]. The rate constant at 1573 K (1300°C) for humid oxidation is 79% higher than dry oxidation. The presence of water vapor significantly accelerates inward oxygen diffusion and subsequent oxidation of the Ni particles forming Ni-spinel.

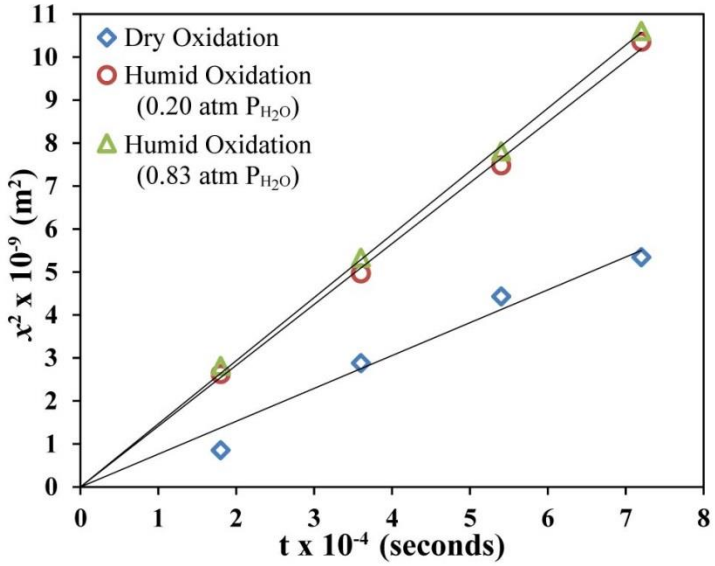

Figure 6.4 Square of the average oxidation depth versus annealing time for dry oxidation and humid oxidation at 0.2 atm P_{H2O} and 0.83 atm P_{H2O} environments at 1573 K. (Trend line fitted using least squares regression.)

The enhanced oxygen mobility likely can be attributed to the smaller size and lower valence of the hydroxyl ion; perhaps slightly counterintuitive is that the size of an (O^{2-}) anion in an oxide lattice shrinks by approximately 20% when a proton is within it (forming (OH^-)). The repulsions in the p-electron cloud of the oxygen ion are decreased due to the embedded proton [140]. In addition the hydroxyl ion can be more easily polarized [51], resulting in an ion that could more easily squeeze through interstitial sites. A simplistic, albeit straightforward, consequence would be that oxygen ions with associated protons (forming hydroxyl ions) can diffuse more readily due to their smaller size, decreased charge, and flexible shape. Surface diffusion of hydroxyl ions is known to be significantly faster than oxygen ion diffusion for alumina [141], so it should come as no surprise that the same would be true for hydroxyl ions diffusing along grain boundaries. (OH^-) is not likely to enter the bulk alumina lattice due to valence imbalance, while grain boundaries are more accommodating.

Protons are strongly bonded within oxygen anions in alumina [142], so coupled diffusion as hydroxide is reasonable. Proton hopping from oxygen to oxygen ion and tunneling also occurs [143]. This would increase oxygen transport via proton-assisted accelerated diffusion of one mobile oxygen ion and then another. Each time a proton hops and forms a bond within an oxygen ion, the anion becomes smaller, diffusing more easily. Enhanced diffusion of hydroxide ions has also been proposed as a reason for faster oxidation of metals that form oxide scales in the presence of water vapor at high temperatures [144]. During the oxidation of metals, researchers have suggested that water vapor can easily be incorporated in oxide films as (OH^-) with faster diffusion via proton hopping and an increase in cation vacancies [145].

There are several caveats to this simple interpretation. Eutectic liquid films formed by impurities can enhance diffusion at grain boundaries. It is conceivable that (OH^-) could produce

thin liquid films at grain boundaries by the interaction with impurities already present. It is also known that high temperature water vapor may remove diffusion-inhibiting anion impurities (such as Cl^- [146]) from grain boundaries. The impurity anion concentration is not known. (OH^-) additionally provides a charge compensating mechanism for the presence of Ni^{2+} replacing Al^{3+} in the grain boundaries as nickel diffuses outward. Charge compensation will affect diffusion values.

This result of accelerated diffusion in the presence of water vapor at high temperatures has significance for alumina films and coatings (especially thermal barrier coatings), as this predicts enhanced penetration of oxygen under such conditions. This effect may also be related to the enhancement of creep rates in alumina in the presence of water vapor [50; 147]. More extensive studies are in progress, including with a range of temperatures to determine activation energies, a range of grain sizes, and the deuterium effect.

6.5 Conclusions

The incorporation of hydroxyl groups from water vapor at high temperatures is believed to enhance grain boundary oxygen diffusion in aluminum oxide, as evidenced by oxidation of marker Ni metal particles in α-Al_2O_3 to form $NiAl_2O_4$. This result certainly implies that other diffusional phenomena relating to (OH^-) incorporation, such as sintering, creep, and corrosion, are anticipated to be affected.

6.6 Specific Acknowledgments

Co-authors of this work include: Peter E. D. Morgan and Martha L. Mecartney from the University of California, Irvine. This research is supported by National Science Foundation Division of Materials Research Grant 1243898. The opinions expressed are those of the authors alone and do not reflect endorsement by NSF.

Chapter 7: Conclusions and Future Work

7.1 Summary and Conclusions

The objective of this research was to explore the potential use of ceramic composite systems as replacements for the single phase components found in solid-state oxygen sensors and nuclear fuel rods. This was achieved by utilizing a combination of experimental and computational techniques. Each of the above studies evaluated the advantages and disadvantages characteristic of their proposed composite systems, and provided a quantitative analysis for the assessment of each system's performance. Additionally, a novel ceramic/metal composite was used to study the grain boundary diffusion of oxygen as a function of oxidation environment. A brief summary and the significant results of each study are presented below.

In Chapter 3, the addition of 20 vol% alumina had the greatest effect on the thermal shock resistance of 8YSZ, achieving an increase of 55%, over single phase 8YSZ. This increase was correlated to the increase in thermal conductivity of the composite, suggesting that the addition of higher thermal conductivity second phases has a greater effect on the thermal shock resistance than the material properties included in the thermal shock resistance parameter alone. Electrochemical impedance measurements showed that the specific grain boundaries in 8YSZ with alumina additions (10 and 20 vol%) were as conductive as pure 8YSZ, suggesting that the reduction (54% for 20 vol%) in the total conductivity was a result of the decrease in grain size of 8YSZ, which created a higher density of grain boundaries. Given these results, a trade-off between the increase in the thermal shock resistance and the decrease in the ionic conductivity must be considered and understood before a complete evaluation of these composite systems can be made.

In Chapter 4, a comparison between analytical models, computational simulations, and experimental techniques was considered in the evaluation of the thermal conductivity of four ceramic composite systems. The experimental evaluation of the thermal conductivity for each composite system, as well as a single-phase control system, was performed by the 3ω method, which was used as the baseline for comparison. The linear Rule of Mixtures model exceeded 100% error in some cases, while the other two analytical models were within 8% (Maxwell Garnett) and 2.5% (Bruggeman) error of the 3ω measurements. OOF2 simulations provided a good approximation of only 1.5 % error. Dimensionless sensitivity analysis was performed to better understand the sensitivity to variations each method had in the evaluations of the thermal conductivity in 2-phase composite systems. Additionally, the Maxwell Garnett model, Bruggeman model, and OOF2 simulations all showed that S_{k_2} decreases with increasing k_2. Indicating that a composite with a high thermally conducting second (k_2) phase will be less sensitive to small perturbations in k_2 when trying to calculate the effective thermal conductivity of the composite. The above comparison of each model, coupled with the sensitivity analysis, allows for greater confidence when predicating the effective thermal conductivity of 2-phase composite systems, and further indicates that OOF2 will provide the most accurate approximation when microstructural information is available.

In Chapter 5, 3-phase and 4-phase ceramic composites were examined as potential replacements for materials currently being used as nuclear fuel. Surrogate phases (CeO_2 or 3Y-TZP) were used as stand-ins for UO_2. The thermal behavior, specifically the temperature dependent thermal conductivity, was determined for each system. Computational simulations, via OOF2, were performed to calculate the thermal conductivity of each system. A comparison of the experimental and computational elevation of the thermal conductivity was performed and

showed the two methods to be in good agreement, having less than a 3% deviation above 673 K (400°C). The incorporation of UO_2 into OOF2 allowed for the simulation of a hypothetical composite fuel system. This four-phase composite showed a 12-16% increase in thermal conductivity, compared to single phase UO_2. The results of this study offer an approach for screening non-fissile material candidates without the need of sample fabrication during the development stages of composite nuclear fuel design.

In Chapter 6, a ceramic/metal composite system was used to explore the effects that water vapor, specifically (OH)- ions, have on the grain boundary diffusion of oxygen. A test platform where Ni-particles are imbedded in a dense Al_2O_3 matrix was fabricated for this purpose. This system takes advantage of a unique reaction where the oxidation of Ni in the presence of Al forms $NiAl_2O_4$, which acts as a marker for determining the penetration depth (i.e. diffusion) of oxygen. Exposing the ceramic/metal composite system to different oxidizing environments (e.g. dry and humidified air) allowed for the reaction kinetics of each environment to be studied. Keeping the oxidation temperature constant at 1573 K (1300°C) and varying only oxidation time, the kinetic rate-constant for oxygen diffusion in the presence of dry air was determined to be 7.9×10^{-14} m^2/s. In the presence of water vapor and keeping all other parameters constant, the kinetic rate-constant for oxygen diffusion was determined to be 1.4×10^{-13} m^2/s, a 79% increase over the dry air condition. This increase in kinetics for the humid oxidizing condition, which is related to the inward diffusion of oxygen, is believed to be due to the (OH)- ions 1) being smaller, 2) having a lower charge than (O^{2-}), and 3) being more polarizable.

7.2 Future Work

Suggested future work to compliment the above research is as follows:

Chapter 3

- Determine what decrease in conductivity is acceptable, if any, in exchange for an increase in thermal shock resistance.
- Explore different material systems with better single phase material properties (e.g. the use of 10YSZ for the matrix phase or ZnO as the particulate phase) relative to the shock resistance parameter.

Chapter 4

- Expand the materials systems evaluated to include 30, 40 and 50 vol% Al_2O_3 to better understand how the different models predict composite systems when the second phase is above the percolation limit.
- Derive the Maxwell Garnett and Bruggeman equations for 3 and 4-phase composite systems (this may already be in the literature), and derive their accompanying sensitivity equations to evaluate how the addition of more phases could alter the systems' response to perturbations.

Chapter 5

- Create hypothetical or "ideal" microstructures for 3 and 4-phase composite systems, evaluate their temperature dependent thermal conductivities via OOF2, compare them to SEM based microstructure and 3ω method, and evaluate their accuracy.
- Use current 4-phase composite microstructure model to screen non-fissile material candidates to determine which composition of phases will yield desired results.

Chapter 6

- Determine the kinetic rate-constant for 1400°C and 1500°C for both dry and humid conditions so that the activation energies of oxygen diffusion can be calculated.
- Replace the pure water used to create the humid environment with D_2O. This will allow for the protonic transport mechanism (i.e. hopping or tunneling) to be studied.
- Perform oxidation test at lower temperatures to determine if the enhanced diffusion rates seen by the water vapor environment is temperature dependent.

References

[1] W. D. Kingery, "Introduction to ceramics," pp. 781 p. Wiley: New York, (1960).

[2] S. Widjaja and D. Singh, "Advanced Ceramic Coatings and Materials for Extreme Environments A Collection of Papers Presented at the 35th International Conference on Advanced Ceramics and Composites January 23-28, 2011 Daytona Beach, Florida Introduction," *Advanced Ceramic Coatings and Materials for Extreme Environments*, 32 Xi-Xiii (2011).

[3] J. P. Angle, Z. J. Wang, C. Dames, and M. L. Mecartney, "Comparison of Two-Phase Thermal Conductivity Models with Experiments on Dilute Ceramic Composites," *Journal of the American Ceramic Society*, 96[**9**] 2935-42 (2013).

[4] A. G. Evans, "Perspective on the Development of High-Toughness Ceramics," *Journal of the American Ceramic Society*, 73[**2**] 187-206 (1990).

[5] P. F. Becher, "Microstructural Design of Toughened Ceramics," *Journal of the American Ceramic Society*, 74[**2**] 255-69 (1991).

[6] N. Claussen, "Fracture Toughness of Al-2 O-3 with an Unstabilized Zro-2 Dispersed Phase," *Journal of the American Ceramic Society*, 59[**1-2**] 49-51 (1976).

[7] T. Hansson, R. Warren, and J. Wasen, "Fracture-Toughness Anisotropy and Toughening Mechanisms of a Hot-Pressed Alumina Reinforced with Silicon-Carbide Whiskers," *Journal of the American Ceramic Society*, 76[**4**] 841-48 (1993).

[8] J. Lalande, S. Scheppokat, R. Janssen, and N. Claussen, "Toughening of alumina /zirconia ceramic composites with silver particles," *Journal of the European Ceramic Society*, 22[**13**] 2165-71 (2002).

[9] W. H. Tuan, "Toughening alumina with nickel aluminide inclusions," *Journal of the European Ceramic Society*, 20[**7**] 895-99 (2000).

[10] W. A. Curtin, "Theory of Mechanical-Properties of Ceramic-Matrix Composites," *Journal of the American Ceramic Society*, 74[**11**] 2837-45 (1991).

[11] D. B. Marshall and A. G. Evans, "Failure Mechanisms in Ceramic-Fiber Ceramic-Matrix Composites," *Journal of the American Ceramic Society*, 68[**5**] 225-31 (1985).

[12] A. A. Buchheit, G. E. Hilmas, W. G. Fahrenholtz, and D. M. Deason, "Thermal Shock Resistance of an AlN-BN-SiC Ceramic," *Journal of the American Ceramic Society*, 92[**6**] 1358-61 (2009).

[13] J. C. Han, C. Q. Hong, X. H. Zhang, and B. L. Wang, "Thermal shock resistance of TiB2-Cu interpenetrating phase composites," *Composites Science and Technology*, 65[**11-12**] 1711-18 (2005).

[14] J. Liang, Y. Wang, G. D. Fang, and J. C. Han, "Research on thermal shock resistance of ZrB2-SiC-AlN ceramics using an indentation-quench method," *Journal of Alloys and Compounds*, 493[**1-2**] 695-98 (2010).

[15] F. Ye, L. M. Liu, H. J. Zhang, and B. S. Wen, "Thermal shock behavior of 30 wt%BAS/Si3N4 self-reinforced composite," *Journal of Alloys and Compounds*, 493[**1-2**] 272-75 (2010).

[16] C. K. Yoon and I. W. Chen, "Superplastic Flow of 2-Phase Ceramics Containing Rigid Inclusions-Zirconia Mullite Composites," *Journal of the American Ceramic Society*, 73[**6**] 1555-65 (1990).

[17] D. Men and M. L. Mecartney, "Superplasticity and machinability in a four-phase ceramic," *Materials Research Bulletin*, 47[**8**] 1925-31 (2012).

[18] A. A. Sharif and M. L. Mecartney, "Superplasticity in cubic yttria stabilized zirconia with 10 wt.% alumina," *Journal of the European Ceramic Society*, 24[**7**] 2041-47 (2004).

[19] T. Chen and M. L. Mecartney, "A high-strain-rate alumina-based ceramic composite," *Journal of the American Ceramic Society*, 88[**4**] 1004-06 (2005).

[20] T. Chen, F. A. Mohamed, and M. L. Mecartney, "Threshold stress superplastic behavior and dislocation activity in a three-phase alumina-zirconia-mullite composite," *Acta Materialia*, 54[**17**] 4415-26 (2006).

[21] T. D. Chen and M. L. Mecartney, "Superplastic compression, microstructural analysis and mechanical properties of a fine grain three-phase alumina-zirconia-mullite ceramic composite," *Materials Science and Engineering a-Structural Materials Properties Microstructure and Processing*, 410 134-39 (2005).

[22] R. P. Dillon, D. K. Kim, J. E. Trujillo, W. M. Kriven, and M. L. Mecartney, "Creep characteristics of alumina, nickel aluminate spinel, zirconia composites," *Journal of Materials Research*, 23[**2**] 556-64 (2008).

[23] V. Dusastre and J. A. Kilner, "Optimisation of composite cathodes for intermediate temperature SOFC applications," *Solid State Ionics*, 126[**1-2**] 163-74 (1999).

[24] A. A. E. Hassan, N. H. Menzler, G. Blass, M. E. Ali, H. P. Buchkremer, and D. Stover, "Influence of alumina dopant on the properties of yttria-stabilized zirconia for SOFC applications," *Journal of Materials Science*, 37[**16**] 3467-75 (2002).

[25] A. J. Feighery and J. T. S. Irvine, "Effect of alumina additions upon electrical properties of 8 mol.% yttria-stabilised zirconia," *Solid State Ionics*, 121[**1-4**] 209-16 (1999).

[26] M. C. Martin and M. L. Mecartney, "Grain boundary ionic conductivity of yttrium stabilized zirconia as a function of silica content and grain size," *Solid State Ionics*, 161[**1-2**] 67-79 (2003).

[27] M. Ghatee, M. H. Shariat, and J. T. S. Irvine, "Investigation of electrical and mechanical properties of 3YSZ/8YSZ composite electrolytes," *Solid State Ionics*, 180[**1**] 57-62 (2009).

[28] M. Leverkoehne, V. S. R. Murthy, R. Janssen, and N. Claussen, "Electrical resistivity of Cr-Al2O3 a interpenetrating and ZrxAly-Al2O3 composites with microstructure," *Journal of the European Ceramic Society*, 22[**13**] 2149-53 (2002).

[29] M. Wada, T. Sekino, T. Kusunose, T. Nakayama, Y. H. Choa, and K. Niihara, "Effects of fine alumina dispersion on ionic conductivity and mechanical properties of ytterbia stabilized cubic zirconia," *Materials Research Innovations*, 8[**2**] 115-20 (2004).

[30] B. Zhu, "Proton and oxygen ion-mixed-conducting ceramic composites and fuel cells," *Solid State Ionics*, 145[**1-4**] 371-80 (2001).

[31] N. P. Bansal and D. M. Zhu, "Thermal conductivity of zirconia-alumina composites," *Ceramics International*, 31[**7**] 911-16 (2005).

[32] L. C. Davis and B. E. Artz, "Thermal-Conductivity of Metal-Matrix Composites," *Journal of Applied Physics*, 77[**10**] 4954-60 (1995).

[33] W. D. Kingery, "Thermal Conductivity .14. Conductivity of Multicomponent Systems," *Journal of the American Ceramic Society*, 42[**12**] 617-27 (1959).

[34] H. A. Bale, A. Haboub, A. A. MacDowell, J. R. Nasiatka, D. Y. Parkinson, B. N. Cox, D. B. Marshall, and R. O. Ritchie, "Real-time quantitative imaging of failure events in materials under load at temperatures above 1,600 degrees C," *Nature Materials*, 12[**1**] 40-46 (2013).

[35] I. Ahmad, H. Z. Cao, H. H. Chen, H. Zhao, A. Kennedy, and Y. Q. Zhu, "Carbon nanotube toughened aluminium oxide nanocomposite," *Journal of the European Ceramic Society*, 30[**4**] 865-73 (2010).

[36] H. K. Cheng, S. J. Dillon, H. S. Caram, J. M. Rickman, H. M. Chan, and M. P. Harmer, "The Effect of Yttrium on Oxygen Grain-Boundary Transport in Polycrystalline Alumina Measured Using Ni Marker Particles," *Journal of the American Ceramic Society*, 91[**6**] 2002-08 (2008).

[37] J. K. Fink, "Thermophysical properties of uranium dioxide," *Journal of Nuclear Materials*, 279[**1**] 1-18 (2000).

[38] K. Nogita and K. Une, "Radiation-Induced Microstructural Change in High Burnup Uo2 Fuel Pellets," *Nuclear Instruments & Methods in Physics Research Section B-Beam Interactions with Materials and Atoms*, 91[**1-4**] 301-06 (1994).

[39] J. A. Valdez, I. O. Usov, J. Won, M. Tang, R. M. Dickerson, G. D. Jarvinen, and K. E. Sickafus, "10 MeV Au ion irradiation effects in an MgO-HfO2 ceramic-ceramic (CERCER) composite," *Journal of Nuclear Materials*, 393[**1**] 126-33 (2009).

[40] X. M. Bai, A. F. Voter, R. G. Hoagland, M. Nastasi, and B. P. Uberuaga, "Efficient Annealing of Radiation Damage Near Grain Boundaries via Interstitial Emission," *Science*, 327[**5973**] 1631-34 (2010).

[41] R. B. Bagwell and G. L. Messing, "Effect of Seeding and Water Vapor on the Nucleation and Growth of α-Al2O3 from γ-Al2O3," *Journal of the American Ceramic Society*, 82[**4**] 825-32 (1999).

[42] Z. Hrabe, J. Majling, S. Svetik, and P. Znasik, "Sintering of silica fume in furnace atmospheres with controlled water vapour partial pressure," *Journal of Thermal Analysis and Calorimetry*, 46[**2**] 535-38 (1996).

[43] T. Kozawa, K. Yanagisawa, and Y. Suzuki, "Water Vapor-Assisted Solid-State Reaction for the Synthesis of Nanocrystalline BaZrO3 Powder," *Journal of the Ceramic Society of Japan*, 121[**1411**] 308-12 (2013).

[44] P. J. Anderson and P. L. Morgan, "Effects of Water Vapour on Sintering of MgO," *Transactions of the Faraday Society*, 60[**4975**] 930-& (1964).

[45] T. Ito, M. Fujita, M. Watanabe, and T. Tokuda, "The Initial Sintering of Alkaline-Earth Oxides in Water-Vapor and Hydrogen Gas," *Bulletin of the Chemical Society of Japan*, 54[**8**] 2412-19 (1981).

[46] R. O. Petersen and I. B. Cutler, "Effects of Water Vapor on Initial Sintering of Calcia," *Journal of the American Ceramic Society*, 51[**1**] 21-& (1968).

[47] P. F. Eastman and I. B. Cutler, "Effect of Water Vapor on Initial Sintering of Magnesia," *Journal of the American Ceramic Society*, 49[**10**] 526-& (1966).

[48] Y. Murase and E. Kato, "Role of Water-Vapor in Crystallite Growth and Tetragonal-Monoclinic Phase-Transformation of Zro2," *Journal of the American Ceramic Society*, 66[**3**] 196-200 (1983).

[49] M. A. V. Garcia, M. C. T. Fernandez, and C. O. Arean, "Effect of Water-Vapor on the Thermal Evolution of the Metastable Phases of Zirconium Dioxide," *Thermochimica Acta*, 126 33-41 (1988).

[50] C. J. Armani, M. B. Ruggles-Wrenn, G. E. Fair, and R. S. Hay, "Creep of Nextel (TM) 610 Fiber at 1100°C in Air and in Steam," *International Journal of Applied Ceramic Technology*, 10[**2**] 276-84 (2013).

[51] R. D. Shannon and R. X. Fischer, "Empirical Electronic Polarizabilities in Oxides, Hydroxides, Oxyfluorides, and Oxychlorides," *Physical Review B*, 73[**23**] (2006).

[52] R. D. Shannon, "Revised Effective Ionic-Radii and Systematic Studies of Interatomic Distances in Halides and Chalcogenides," *Acta Crystallographica Section A*, 32[**Sep1**] 751-67 (1976).

[53] M. Nanko, "High-temperature oxidation of ceramic matrix composites dispersed with metallic particles," *Science and Technology of Advanced Materials*, 6[**2**] 129-34 (2005).

[54] M. T. Schatzmann, M. L. Mecartney, and P. E. D. Morgan, "Synthesis of monoclinic monazite, LaPO4, by direct precipitation," *Journal of Materials Chemistry*, 19[**32**] 5720-22 (2009).

[55] R. G. Munro, "Evaluated material properties for a sintered alpha-alumina," *Journal of the American Ceramic Society*, 80[**8**] 1919-28 (1997).

[56] A. W. Thompson, "Calculation of true volume grain diameter," *Metallography*, 5[**4**] 366-369369 (1972).

[57] Z. Li, A. Ghosh, A. S. Kobayashi, and R. C. Bradt, "Indentation Fracture-Toughness of Sintered Silicon-Carbide in the Palmqvist Crack Regime," *Journal of the American Ceramic Society*, 72[**6**] 904-11 (1989).

[58] M. J. Verkerk, B. J. Middelhuis, and A. J. Burggraaf, "Effect of Grain-Boundaries on the Conductivity of High-Purity Zro2-Y2o3 Ceramics," *Solid State Ionics*, 6[**2**] 159-70 (1982).

[59] W. C. Chueh, C. K. Yang, C. M. Garland, W. Lai, and S. M. Haile, "Unusual decrease in conductivity upon hydration in acceptor doped, microcrystalline ceria," *Physical Chemistry Chemical Physics*, 13[**14**] 6442-51 (2011).

[60] A. C. E. Reid, S. A. Langer, R. C. Lua, V. R. Coffman, S. I. Haan, and R. E. Garcia, "Image-based finite element mesh construction for material microstructures," *Computational Materials Science*, 43[**4**] 989-99 (2008).

[61] A. C. E. Reid, R. C. Lua, R. E. Garcia, V. R. Coffman, and S. A. Langer, "Modelling Microstructures with OOF2," *International Journal of Materials & Product Technology*, 35[**3-4**] 361-73 (2009).

[62] D. S. Mclachlan, M. Blaszkiewicz, and R. E. Newnham, "Electrical-Resistivity of Composites," *Journal of the American Ceramic Society*, 73[**8**] 2187-203 (1990).

[63] J. D. Wang and R. Raj, "Activation-Energy for the Sintering of 2-Phase Alumina Zirconia Ceramics," *Journal of the American Ceramic Society*, 74[**8**] 1959-63 (1991).

[64] R. Ramamoorthy, P. K. Dutta, and S. A. Akbar, "Oxygen sensors: Materials, methods, designs and applications," *Journal of Materials Science*, 38[**21**] 4271-82 (2003).

[65] M. Ishitsuka, T. Sato, T. Endo, and M. Shimada, "Thermal-Shock Fracture-Behavior of Zro2 Based Ceramics," *Journal of Materials Science*, 24[**11**] 4057-61 (1989).

[66] M. Mori, T. Abe, H. Itoh, O. Yamamoto, Y. Takeda, and T. Kawahara, "Cubic-Stabilized Zirconia and Alumina Composites as Electrolytes in Planar Type Solid Oxide Fuel-Cells," *Solid State Ionics*, 74[**3-4**] 157-64 (1994).

[67] D. P. H. Hasselma, "Unified Theory of Thermal Shock Fracture Initiation and Crack Propagation in Brittle Ceramics," *Journal of the American Ceramic Society*, 52[**11**] 600-04 (1969).

[68] A. Selcuk and A. Atkinson, "Elastic properties of ceramic oxides used in solid oxide fuel cells (SOFC)," *Journal of the European Ceramic Society*, 17[**12**] 1523-32 (1997).

[69] D. P. H. Hasselman, L. F. Johnson, L. D. Bentsen, R. Syed, H. L. Lee, and M. V. Swain, "Thermal-Diffusivity and Conductivity of Dense Polycrystalline Zro2 Ceramics - a Survey," *American Ceramic Society Bulletin*, 66[**5**] 799-806 (1987).

[70] S. Raghavan, H. Wang, R. B. Dinwiddie, W. D. Porter, and M. J. Mayo, "The effect of grain size, porosity and yttria content on the thermal conductivity of nanocrystalline zirconia," *Scripta Materialia*, 39[**8**] 1119-25 (1998).

[71] K. W. Schlichting, N. P. Padture, and P. G. Klemens, "Thermal conductivity of dense and porous yttria-stabilized zirconia," *Journal of Materials Science*, 36[**12**] 3003-10 (2001).

[72] H. Hayashi, T. Saitou, N. Maruyama, H. Inaba, K. Kawamura, and M. Mori, "Thermal expansion coefficient of yttria stabilized zirconia for various yttria contents," *Solid State Ionics*, 176[**5-6**] 613-19 (2005).

[73] M. Hamidouche, N. Bouaouadja, C. Olagnon, and G. Fantozzi, "Thermal shock behaviour of mullite ceramic," *Ceramics International*, 29[**6**] 599-609 (2003).

[74] H. Schneider, J. Schreuer, and B. Hildmann, "Structure and properties of mullite - A review," *Journal of the European Ceramic Society*, 28[**2**] 329-44 (2008).

[75] U. Kolitsch, H. J. Seifert, T. Ludwig, and F. Aldinger, "Phase equilibria and crystal chemistry in the Y2O3-Al2O3-SiO2 system," *Journal of Materials Research*, 14[**2**] 447-55 (1999).

[76] Y. J. Lin, P. Angelini, and M. L. Mecartney, "Microstructural and Chemical Influences of Silicate Grain-Boundary Phases in Yttria-Stabilized Zirconia," *Journal of the American Ceramic Society*, 73[**9**] 2728-35 (1990).

[77] L. Donzel and S. G. Roberts, "Microstructure and mechanical properties of cubic zirconia (8YSZ)/SiC nanocomposites," *Journal of the European Ceramic Society*, 20[**14-15**] 2457-62 (2000).

[78] N. H. Kwon, G. H. Kim, H. S. Song, and H. L. Lee, "Synthesis and properties of cubic zirconia-alumina composite by mechanical alloying," *Materials Science and Engineering a-Structural Materials Properties Microstructure and Processing*, 299[**1-2**] 185-94 (2001).

[79] D. K. Kim and W. M. Kriven, "Processing and characterization of multiphase ceramic composites part III: Strong, hard and tough, high temperature-stable quadruplex and quintuplex composites," *Journal of the American Ceramic Society*, 91[**3**] 799-805 (2008).

[80] D. P. H. Hasselma, "Thermal Stress Resistance Parameters for Brittle Refractory Ceramics - a Compendium," *American Ceramic Society Bulletin*, 49[**12**] 1033-37 (1970).

[81] W. D. Kingery, "Factors Affecting Thermal Stress Resistance of Ceramic Materials," *Journal of the American Ceramic Society*, 38[**1**] 3-15 (1955).

[82] X. H. Zhang, Z. Wang, C. Q. Hong, P. Hu, and W. B. Han, "Modification and validation of the thermal shock parameter for ceramic matrix composites under water quenching condition," *Materials & Design*, 30[**10**] 4552-56 (2009).

[83] J. E. Bauerle, "Study of Solid Electrolyte Polarization by a Complex Admittance Method," *Journal of Physics and Chemistry of Solids*, 30[**12**] 2657-& (1969).

[84] S. Rajendran, J. Drennan, and S. P. S. Badwal, "Effect of Alumina Additions on the Grain-Boundary and Volume Resistivity of Tetragonal Zirconia Polycrystals," *Journal of Materials Science Letters*, 6[**12**] 1431-34 (1987).

[85] E. P. Butler and J. Drennan, "Microstructural Analysis of Sintered High-Conductivity Zirconia with Al2o3 Additions," *Journal of the American Ceramic Society*, 65[**10**] 474-78 (1982).

[86] Y. Ji, J. Liu, Z. Lu, X. Zhao, T. M. He, and W. H. Su, "Study on the properties of Al2O3-doped (ZrO2)(0.92)(Y2O3)(0.08) electrolyte," *Solid State Ionics*, 126[**3-4**] 277-83 (1999).

[87] M. Aoki, Y. M. Chiang, I. Kosacki, I. J. R. Lee, H. Tuller, and Y. P. Liu, "Solute segregation and grain-boundary impedance in high-purity stabilized zirconia," *Journal of the American Ceramic Society*, 79[**5**] 1169-80 (1996).

[88] X. Guo and J. Maier, "Grain boundary blocking effect in zirconia: A Schottky barrier analysis," *Journal of the Electrochemical Society*, 148[**3**] E121-E26 (2001).

[89] M. J. Verkerk, A. J. A. Winnubst, and A. J. Burggraaf, "Effect of Impurities on Sintering and Conductivity of Yttria-Stabilized Zirconia," *Journal of Materials Science*, 17[**11**] 3113-22 (1982).

[90] D. R. Clarke, "Interpenetrating Phase Composites," *Journal of the American Ceramic Society*, 75[**4**] 739-59 (1992).

[91] J. Hostasa, W. Pabst, and J. Matejicek, "Thermal Conductivity of Al2O3-ZrO2 Composite Ceramics," *Journal of the American Ceramic Society*, 94[**12**] 4404-09 (2011).

[92] M. R. Winter and D. R. Clarke, "Oxide materials with low thermal conductivity," *Journal of the American Ceramic Society*, 90[**2**] 533-40 (2007).

[93] C. Dames and G. Chen, "1 omega, 2 omega, and 3 omega methods for measurements of thermal properties," *Review of Scientific Instruments*, 76[**12**] (2005).

[94] D. G. Cahill, "Thermal conductivity measurement from 30 to 750 K: The 3 omega method (vol 61, pg 802, 1990)," *Review of Scientific Instruments*, 73[**10**] 3701-01 (2002).

[95] Z. J. Wang, J. E. Alaniz, W. Y. Jang, J. E. Garay, and C. Dames, "Thermal Conductivity of Nanocrystalline Silicon: Importance of Grain Size and Frequency-Dependent Mean Free Paths," *Nano Letters*, 11[**6**] 2206-13 (2011).

[96] Z. Wang, A. Kulkarni, S. Deshpande, T. Nakamura, and H. Herman, "Effects of pores and interfaces on effective properties of plasma sprayed zirconia coatings," *Acta Materialia*, 51[**18**] 5319-34 (2003).

[97] K. E. Pappacena, M. T. Johnson, H. Wang, W. D. Porter, and K. T. Faber, "Thermal properties of wood-derived copper-silicon carbide composites fabricated via electrodeposition," *Composites Science and Technology*, 70[**3**] 478-84 (2010).

[98] R. Landauer, "The Electrical Resistance of Binary Metallic Mixtures," *Journal of Applied Physics*, 23[**7**] 779-84 (1952).

[99] A. G. Every, Y. Tzou, D. P. H. Hasselman, and R. Raj, "The Effect of Particle-Size on the Thermal-Conductivity of Zns Diamond Composites," *Acta Metallurgica Et Materialia*, 40[**1**] 123-29 (1992).

[100] N. J. Kidner, N. H. Perry, T. O. Mason, and E. J. Garboczi, "The brick layer model revisited: introducing the nano-grain composite model," *Journal of the American Ceramic Society*, 91[**6**] 1733-46 (2008).

[101] G. A. Niklasson, C. G. Granqvist, and O. Hunderi, "Effective Medium Models for the Optical-Properties of Inhomogeneous Materials," *Applied Optics*, 20[**1**] 26-30 (1981).

[102] D. A. G. Bruggeman, "Calculation of various physics constants in heterogenous substances I Dielectricity constants and conductivity of mixed bodies from isotropic substances," *Annalen Der Physik*, 24[**7**] 636-64 (1935).

[103] A. Bjorneklett, L. Haukeland, J. Wigren, and H. Kristiansen, "Effective-Medium Theory and the Thermal-Conductivity of Plasma-Sprayed Ceramic Coatings," *Journal of Materials Science*, 29[**15**] 4043-50 (1994).

[104] Z. M. He, C. Stiewe, D. Platzek, G. Karpinski, E. Muller, S. H. Li, M. Toprak, and M. Muhammed, "Effect of ceramic dispersion on thermoelectric properties of nano-ZrO2/CoSb3 composites," *Journal of Applied Physics*, 101[**4**] (2007).

[105] R. F. Hill and P. H. Supancic, "Thermal conductivity of platelet-filled polymer composites," *Journal of the American Ceramic Society*, 85[**4**] 851-57 (2002).

[106] N. Nitani, T. Yamashita, T. Matsuda, S. Kobayashi, and T. Ohmichi, "Thermophysical properties of rock-like oxide fuel with spinel-yttria stabilized zirconia system," *Journal of Nuclear Materials*, 274[**1-2**] 15-22 (1999).

[107] J. Y. Oh, Y. H. Koo, B. H. Lee, and Y. W. Tahk, "Evaluation of the effective thermal conductivity of UO2 fuel by combining Potts model and finite difference method," *Journal of Nuclear Materials*, 414[**2**] 320-23 (2011).

[108] N. Tessier-Doyen, X. Grenier, M. Huger, D. S. Smith, D. Fournier, and J. P. Roger, "Thermal conductivity of alumina inclusion/glass matrix composite materials: local and macroscopic scales," *Journal of the European Ceramic Society*, 27[**7**] 2635-40 (2007).

[109] D. P. H. Hasselman and L. F. Johnson, "Effective Thermal-Conductivity of Composites with Interfacial Thermal Barrier Resistance," *Journal of Composite Materials*, 21[**6**] 508-15 (1987).

[110] R. S. Lima and B. R. Marple, "Nanostructured YSZ thermal barrier coatings engineered to counteract sintering effects," *Materials Science and Engineering a-Structural Materials Properties Microstructure and Processing*, 485[**1-2**] 182-93 (2008).

[111] C. Amaya, J. C. Caicedo, J. M. Yanez-Limon, R. A. Vargas, G. Zambrano, M. E. Gomez, and P. Prieto, "A non-destructive method for determination of thermal conductivity of YSZ coatings deposited on Si substrates," *Materials Chemistry and Physics*, 136[**2-3**] 917-24 (2012).

[112] B. Hildmann and H. Schneider, "Thermal conductivity of 2/1-mullite single crystals," *Journal of the American Ceramic Society*, 88[**10**] 2879-82 (2005).

[113] W. D. Kingery, J. Francl, R. L. Coble, and T. Vasilos, "Thermal Conductivity .10. Data for Several Pure Oxide Materials Corrected to Zero Porosity," *Journal of the American Ceramic Society*, 37[**2**] 107-10 (1954).

[114] P. G. Klemens and M. Gell, "Thermal conductivity of thermal barrier coatings," *Materials Science and Engineering a-Structural Materials Properties Microstructure and Processing*, 245[**2**] 143-49 (1998).

[115] R. Landauer, "Electrical conductivity in inhomogeneous media," *AIP Conference Proceedings*[**40**] 2-4545 (1978).

[116] H. G. Elrod, "Two simple theorems for establishing bounds on the total heat flow in steady-state heat-conduction problems with convective boundary conditions," *Transactions of the ASME. Series C, Journal of Heat Transfer*, 96[**1**] 65-7070 (1974).

[117] P. G. Klemens, "Thermal Conductivity of Inhomogeneous Media," *High temperatures - high pressures*, 23 241 -48 (1991).

[118] K. Yamada, K. Kurosaki, M. Uno, and S. Yamanaka, "Evaluation of thermal properties of uranium dioxide by molecular dynamics," *Journal of Alloys and Compounds*, 307 10-16 (2000).

[119] J. H. Kittel, B. R. T. Frost, J. P. Mustelier, K. Q. Bagley, G. C. Crittenden, and J. Vandievoet, "History of Fast-Reactor Fuel Development," *Journal of Nuclear Materials*, 204 1-13 (1993).

[120] A. T. Nelson, M. M. Giachino, J. C. Nino, and K. J. McClellan, "Effect of composition on thermal conductivity of MgO-Nd2Zr2O7 composites for inert matrix materials," *Journal of Nuclear Materials*, 444[**1-3**] 385-92 (2014).

[121] N. Nitani, H. Yokoi, T. Yamashita, T. Ohmichi, T. Matsui, and T. Muromura, "Phase relations and distribution of fission products in the Pu rock-like fuels with fluorite, spinel and corundum phases," *Journal of Nuclear Materials*, 247 59-62 (1997).

[122] K. Kuramoto, T. Yamashita, and T. Shiratori, "Post-irradiation examination of uranium-doped rock-like oxide fuels," *Progress in Nuclear Energy*, 38[**3-4**] 423-26 (2001).

[123] T. Yamashita, K. Kuramoto, N. Nitani, Y. Nakano, H. Akie, H. Nagashima, Y. Kimura, and T. Ohmichi, "Irradiation behavior of rock-like oxide fuels," *Journal of Nuclear Materials*, 320[**1-2**] 126-32 (2003).

[124] D. Men, M. K. Patel, I. O. Usov, M. Toiammou, I. Monnet, J. C. Pivin, J. R. Porter, and M. L. Mecartney, "Radiation damage in multiphase ceramics," *Journal of Nuclear Materials*, 443[**1–3**] 120-27 (2013).

[125] P. E. D. Morgan, R. M. Housley, J. B. Davis, and M. L. DeHaan, "Chemical and Ceramic Methods Toward Safe Storage of Actinides," pp. Medium: ED. in**.**, 2005.

[126] K. R. Wilkerson, J. D. Smith, T. P. Sander, and J. G. Hemrick, "Solid Solution Effects on the Thermal Properties in the MgAl2O4-MgGa2O4 System," *Journal of the American Ceramic Society*, 96[**3**] 859-66 (2013).

[127] B. Jiang, M. H. Fang, Z. H. Huang, Y. G. Liu, P. Peng, and J. Zhang, "Mechanical and thermal properties of LaMgAl11O19," *Materials Research Bulletin*, 45[**10**] 1506-08 (2010).

[128] P. E. D. Morgan and E. H. Cirlin, "The Magnetoplumbite Crystal-Structure as a Radwaste Host," *Journal of the American Ceramic Society*, 65[**7**] C114-C15 (1982).

[129]Standard test method for density of compacted or sintered powder metallurgy (PM) products using archimedes' principle, ASTM International, West Conshohocken, PA, B962-08 2008.

[130] K. Kadoya, N. Matsunaga, and A. Nagashima, "Viscosity and Thermal-Conductivity of Dry Air in the Gaseous-Phase," *Journal of Physical and Chemical Reference Data*, 14[**4**] 947-70 (1985).

[131] C. W. Nan, R. Birringer, D. R. Clarke, and H. Gleiter, "Effective thermal conductivity of particulate composites with interfacial thermal resistance," *Journal of Applied Physics*, 81[**10**] 6692-99 (1997).

[132] J. Cho, C. M. Wang, H. M. Chan, J. M. Rickman, and M. P. Harmer, "Role of Segregating Dopants on the Improved Creep Resistance of Aluminum Oxide," *Acta Materialia*, 47[**15-16**] 4197-207 (1999).

[133] J. A. Nychka and D. R. Clarke, "Quantification of Aluminum Outward Diffusion During Oxidation of FeCrAl Alloys," *Oxidation of Metals*, 63[**5-6**] 325-52 (2005).

[134] J. Barbier-Jr and D. Duprez, "Steam Effects in 3-Way Catalysis," *Applied Catalysis B-Environmental*, 4[**2-3**] 105-40 (1994).

[135] A. H. Heuer, "Oxygen and Aluminum Diffusion in α-Al2O3: How Much do we Really Understand?," *Journal of the European Ceramic Society*, 28[**7**] 1495-507 (2008).

[136] M. Nanko, N. D. Thuy, K. Matsumaru, and K. Ishizaki, "High Temperature Oxidation of Al2O3-Based Composites with Ni Particle Dispersion," *Journal of Ceramic Processing Research*, 3[**3**] 132-35 (2002).

[137] T. C. Wang, R. Z. Chen, and W. H. Tuan, "Oxidation Resistance of Ni-Toughened Al2O3," *Journal of the European Ceramic Society*, 23[**6**] 927-34 (2003).

[138] F. A. Elrefaie and W. W. Smeltzer, "Phase-Equilibria in the Subsolidus Region of the NiO-α-Al2O3 System between 1000 and 1920°C," *Oxidation of Metals*, 15[**5-6**] 495-500 (1981).

[139] J. A. Haynes, K. A. Unocic, and B. A. Pint, "Effect of Water Vapor on the 1100°C Oxidation Behavior of Plasma-Sprayed TBCs with HVOF NiCoCrAlX Bond Coatings," *Surface and Coatings Technology*, 215[**0**] 39-45 (2013).

[140] T. Norby, "Proton Conduction in Oxides," *Solid State Ionics*, 40-1 857-62 (1990).

[141] M. Pijolat, M. Dauzat, and M. Soustelle, "Influence of Water-Vapor and Additives on the Surface-Area Stability of γ-Al2O3," *Solid State Ionics*, 50[**1-2**] 31-39 (1992).

[142] A. K. Kronenberg, J. Castaing, T. E. Mitchell, and S. H. Kirby, "Hydrogen Defects in α-Al2O3 and Water Weakening of Sapphire and Alumina Ceramics Between 600 and 1000°C -I. Infrared Characterization of Defects," *Acta Materialia*, 48[**7**] 1481-94 (2000).

[143] T. Norby and Y. Larring, "Concentration and Transport of Protons in Oxides," *Current Opinion in Solid State & Materials Science*, 2[**5**] 593-99 (1997).

[144] S. Basu, N. Obando, A. Gowdy, I. Karaman, and M. Radovic, "Long-Term Oxidation of Ti2AlC in Air and Water Vapor at 1000-1300 degrees C Temperature Range (vol 159, pg C90, 2012)," *Journal of the Electrochemical Society*, 159[**5**] S9-S9 (2012).

[145] S. R. J. Saunders, M. Monteiro, and F. Rizzo, "The Oxidation Behaviour of Metals and Alloys at High Temperatures in Atmospheres Containing Water Vapour: A Review," *Progress in Materials Science*, 53[**5**] 775-837 (2008).

[146] S. Balcon, S. Mary, C. Kappenstein, and E. Gengembre, "Monopropellant Decomposition Catalysts II. Sintering Studies on Ir/Al2O3 Catalysts, Influence of Chloride Anions," *Applied Catalysis a-General*, 196[**2**] 179-90 (2000).

[147] J. Castaing, A. K. Kronenberg, S. H. Kirby, and T. E. Mitchell, "Hydrogen Defects in α-Al2O3 and Water Weakening of Sapphire and Alumina Ceramics Between 600 and 1000°C -II. Mechanical Properties," *Acta Materialia*, 48[**7**] 1495-504 (2000).

Appendices

Appendix A: Sample OOF2 Code

This code was developed to determine the thermal conductivity of the multiphase ceramic composites described in Chapter 5. The below script is meant to be loaded into the terminal feature of OOF2. More information on how to run OOF2 in text mode can be found at http://www.ctcms.nist.gov/oof/oof2/

```
OOF.Microstructure.Create_From_ImageFile(filename='/data/users/jangle/3Y-ASM.png',
microstructure_name='3Y-ASM.png', height=automatic, width=automatic)
OOF.Image.AutoGroup(image='3Y-ASM.png:3Y-ASM.png', name_template='%c')
OOF.PixelGroup.Rename(microstructure='3Y-ASM.png', group='#0000ff', new_name='Monazite')
OOF.PixelGroup.Rename(microstructure='3Y-ASM.png', group='#ffffff', new_name='Zirconia')
OOF.PixelGroup.Rename(microstructure='3Y-ASM.png', group='#ff0000', new_name='Spinel')
OOF.PixelGroup.Rename(microstructure='3Y-ASM.png', group='#00ff00', new_name='Alumina')
OOF.PixelGroup.Rename(microstructure='3Y-ASM.png', group='#000000', new_name='Porosity')
OOF.Material.New(name='Monazite_Material', material_type='bulk')
OOF.Material.New(name='Spinel_Material', material_type='bulk')
OOF.Material.New(name='Alumina_Material', material_type='bulk')
OOF.Material.New(name='Zirconia_Material', material_type='bulk')
OOF.Material.New(name='Porosity_Material', material_type='bulk')
OOF.Property.Copy(property='Thermal:Conductivity:Isotropic', new_name='Alumina_Therm')
OOF.Property.Copy(property='Thermal:Conductivity:Isotropic:Alumina_Therm', new_name='Monazite_Therm')
OOF.Property.Copy(property='Thermal:Conductivity:Isotropic:Monazite_Therm', new_name='Spinel_Therm')
OOF.Property.Copy(property='Thermal:Conductivity:Isotropic:Spinel_Therm', new_name='Zirconia_Therm')
OOF.Property.Copy(property='Thermal:Conductivity:Isotropic:Zirconia_Therm', new_name='Porosity_Therm')
OOF.Property.Parametrize.Thermal.Conductivity.Isotropic.Alumina_Therm(kappa=26.2651044923341)
OOF.Property.Parametrize.Thermal.Conductivity.Isotropic.Monazite_Therm(kappa=2.49358974358974)
OOF.Property.Parametrize.Thermal.Conductivity.Isotropic.Spinel_Therm(kappa=14.7353082465973)
OOF.Property.Parametrize.Thermal.Conductivity.Isotropic.Zirconia_Therm(kappa=3.125)
OOF.Property.Parametrize.Thermal.Conductivity.Isotropic.Porosity_Therm(kappa=0.025700000000000001)
OOF.Material.Add_property(name='Zirconia_Material',
property='Thermal:Conductivity:Isotropic:Zirconia_Therm')
OOF.Material.Assign(material='Zirconia_Material', microstructure='3Y-ASM.png', pixels='Zirconia')
OOF.Material.Add_property(name='Spinel_Material', property='Thermal:Conductivity:Isotropic:Spinel_Therm')
OOF.Material.Assign(material='Spinel_Material', microstructure='3Y-ASM.png', pixels='Spinel')
OOF.Material.Add_property(name='Monazite_Material',
property='Thermal:Conductivity:Isotropic:Monazite_Therm')
OOF.Material.Assign(material='Monazite_Material', microstructure='3Y-ASM.png', pixels='Monazite')
OOF.Material.Add_property(name='Alumina_Material',
property='Thermal:Conductivity:Isotropic:Alumina_Therm')
OOF.Material.Assign(material='Alumina_Material', microstructure='3Y-ASM.png', pixels='Alumina')
OOF.Material.Add_property(name='Porosity_Material', property='Thermal:Conductivity:Isotropic:Porosity_Therm')
OOF.Material.Assign(material='Porosity_Material', microstructure='3Y-ASM.png', pixels='Porosity')
OOF.Skeleton.New(name='skeleton', microstructure='3Y-ASM.png', x_elements=46, y_elements=40,
skeleton_geometry=QuadSkeleton(left_right_periodicity=False,top_bottom_periodicity=False))
OOF.Skeleton.Modify(skeleton='3Y-ASM.png:skeleton',
modifier=Refine(targets=CheckHomogeneity(threshold=0.96999999999999997),criterion=Unconditionally(),degree
=Trisection(rule_set='conservative'),alpha=0.5))
OOF.Skeleton.Modify(skeleton='3Y-ASM.png:skeleton',
modifier=Refine(targets=CheckHomogeneity(threshold=0.93000000000000002),criterion=Unconditionally(),degree
=Trisection(rule_set='conservative'),alpha=0.5))
```

```
OOF.Skeleton.Modify(skeleton='3Y-ASM.png:skeleton',
modifier=Refine(targets=CheckHomogeneity(threshold=0.90000000000000002),criterion=Unconditionally(),degree
=Trisection(rule_set='conservative'),alpha=0.5))
OOF.Skeleton.Modify(skeleton='3Y-ASM.png:skeleton',
modifier=SnapNodes(targets=SnapHeterogenous(threshold=0.90000000000000002),criterion=AverageEnergy(alph
a=1)))
OOF.Skeleton.Modify(skeleton='3Y-ASM.png:skeleton',
modifier=SnapNodes(targets=SnapHeterogenous(threshold=0.90000000000000002),criterion=AverageEnergy(alph
a=1)))
OOF.Skeleton.Modify(skeleton='3Y-ASM.png:skeleton',
modifier=Rationalize(targets=AllElements(),criterion=AverageEnergy(alpha=0.90000000000000002),method=Auto
maticRationalization()))
OOF.ElementSelection.Select_by_Homogeneity(skeleton='3Y-ASM.png:skeleton',
threshold=0.90000000000000002)
OOF.Skeleton.Modify(skeleton='3Y-ASM.png:skeleton',
modifier=Anneal(targets=FiddleSelectedElements(),criterion=AverageEnergy(alpha=0.90000000000000002),T=0.0
,delta=1.0,iteration=ConditionalIteration(condition=AcceptanceRate(acceptance_rate=5),extra=15,maximum=50)))
OOF.Skeleton.Modify(skeleton='3Y-ASM.png:skeleton',
modifier=Rationalize(targets=AllElements(),criterion=AverageEnergy(alpha=0.90000000000000002),method=Auto
maticRationalization()))
OOF.ElementSelection.Clear(skeleton='3Y-ASM.png:skeleton')
OOF.Skeleton.PinNodes.Pin_Internal_Boundary_Nodes(skeleton='3Y-ASM.png:skeleton')
OOF.Skeleton.Modify(skeleton='3Y-ASM.png:skeleton',
modifier=Rationalize(targets=AllElements(),criterion=AverageEnergy(alpha=0.80000000000000004),method=Auto
maticRationalization()))
OOF.Skeleton.Modify(skeleton='3Y-ASM.png:skeleton',
modifier=MergeTriangles(targets=AllElements(),criterion=LimitedUnconditional(alpha=0.5,homogeneity=0.90000
000000000002,shape_energy=0.5)))
OOF.Skeleton.Modify(skeleton='3Y-ASM.png:skeleton',
modifier=Smooth(targets=AllNodes(),criterion=AverageEnergy(alpha=0.59999999999999998),T=0.0,iteration=Con
ditionalIteration(condition=AcceptanceRate(acceptance_rate=30),extra=15,maximum=50)))
OOF.Skeleton.PinNodes.UnpinAll(skeleton='3Y-ASM.png:skeleton')
OOF.Mesh.New(name='mesh', skeleton='3Y-ASM.png:skeleton', element_types={'D2_2', 'T3_3', 'Q4_4'])
OOF.Subproblem.Field.Define(subproblem='3Y-ASM.png:skeleton:mesh:default', field=Temperature)
OOF.Subproblem.Field.Activate(subproblem='3Y-ASM.png:skeleton:mesh:default', field=Temperature)
OOF.Subproblem.Equation.Activate(subproblem='3Y-ASM.png:skeleton:mesh:default', equation=Heat_Eqn)
OOF.Subproblem.Equation.Activate(subproblem='3Y-ASM.png:skeleton:mesh:default',
equation=Plane_Heat_Flux)
OOF.Mesh.Boundary_Conditions.New(name='bc', mesh='3Y-ASM.png:skeleton:mesh',
condition=DirichletBC(field=Temperature,field_component='',equation=Heat_Eqn,eqn_component='',profile=Const
antProfile(value=95.0),boundary='top'))
OOF.Mesh.Boundary_Conditions.New(name='bc<2>', mesh='3Y-ASM.png:skeleton:mesh',
condition=DirichletBC(field=Temperature,field_component='',equation=Heat_Eqn,eqn_component='',profile=Const
antProfile(value=105.0),boundary='bottom'))
OOF.Mesh.Boundary_Conditions.New(name='bc<3>', mesh='3Y-ASM.png:skeleton:mesh',
condition=NeumannBC(flux=Heat_Flux,profile=ConstantProfile(value=0.0),boundary='right',normal=False))
OOF.Mesh.Boundary_Conditions.New(name='bc<4>', mesh='3Y-ASM.png:skeleton:mesh',
condition=NeumannBC(flux=Heat_Flux,profile=ConstantProfile(value=0.0),boundary='left',normal=False))
OOF.Subproblem.Set_Solver(subproblem='3Y-ASM.png:skeleton:mesh:default',
solver_mode=BasicSolverMode(time_stepper=BasicStaticDriver(),matrix_method=BasicIterative(tolerance=1e-
10,max_iterations=100000)))
OOF.Mesh.Solve(mesh='3Y-ASM.png:skeleton:mesh', endtime=0.0)
OOF.Mesh.Analyze.Integral(mesh='3Y-ASM.png:skeleton:mesh', time=latest,
data=getOutput('Flux:Invariant',invariant=Magnitude(),flux=Heat_Flux),
domain=SkeletonEdgeBoundaryDomain(boundary='top',side='LEFT'),
```

```
sampling=StatElementSegmentSampleSet(n_points=25),
destination=OutputStream(filename='/data/users/jangle/3Y-ASM_Z_1_inter_100C',mode='w'))
OOF.Material.Remove_property(name='Alumina_Material',
property='Thermal:Conductivity:Isotropic:Alumina_Therm')
OOF.Property.Parametrize.Thermal.Conductivity.Isotropic.Alumina_Therm(kappa=20.2300501495914)
OOF.Material.Add_property(name='Alumina_Material',
property='Thermal:Conductivity:Isotropic:Alumina_Therm')
OOF.Material.Remove_property(name='Spinel_Material',
property='Thermal:Conductivity:Isotropic:Spinel_Therm')
OOF.Property.Parametrize.Thermal.Conductivity.Isotropic.Spinel_Therm(kappa=12.2221628838451)
OOF.Material.Add_property(name='Spinel_Material', property='Thermal:Conductivity:Isotropic:Spinel_Therm')
OOF.Material.Remove_property(name='Zirconia_Material',
property='Thermal:Conductivity:Isotropic:Zirconia_Therm')
OOF.Property.Parametrize.Thermal.Conductivity.Isotropic.Zirconia_Therm(kappa=3.03333333333333)
OOF.Material.Add_property(name='Zirconia_Material',
property='Thermal:Conductivity:Isotropic:Zirconia_Therm')
OOF.Material.Remove_property(name='Monazite_Material',
property='Thermal:Conductivity:Isotropic:Monazite_Therm')
OOF.Property.Parametrize.Thermal.Conductivity.Isotropic.Monazite_Therm(kappa=2.09090909090909)
OOF.Material.Add_property(name='Monazite_Material',
property='Thermal:Conductivity:Isotropic:Monazite_Therm')
OOF.Mesh.Boundary_Conditions.Edit(name='bc', mesh='3Y-ASM.png:skeleton:mesh',
condition=DirichletBC(field=Temperature,field_component='',equation=Heat_Eqn,eqn_component='',profile=Const
antProfile(value=195.0),boundary='top'))
OOF.Mesh.Boundary_Conditions.Edit(name='bc<2>', mesh='3Y-ASM.png:skeleton:mesh',
condition=DirichletBC(field=Temperature,field_component='',equation=Heat_Eqn,eqn_component='',profile=Const
antProfile(value=205.0),boundary='bottom'))
OOF.Mesh.Solve(mesh='3Y-ASM.png:skeleton:mesh', endtime=0.0)
OOF.Mesh.Analyze.Integral(mesh='3Y-ASM.png:skeleton:mesh', time=latest,
data=getOutput('Flux:Invariant',invariant=Magnitude(),flux=Heat_Flux),
domain=SkeletonEdgeBoundaryDomain(boundary='top',side='LEFT'),
sampling=StatElementSegmentSampleSet(n_points=25),
destination=OutputStream(filename='/data/users/jangle/3Y-ASM_Z_1_inter_200C',mode='w'))
OOF.Material.Remove_property(name='Alumina_Material',
property='Thermal:Conductivity:Isotropic:Alumina_Therm')
OOF.Property.Parametrize.Thermal.Conductivity.Isotropic.Alumina_Therm(kappa=16.1805719735346)
OOF.Material.Add_property(name='Alumina_Material',
property='Thermal:Conductivity:Isotropic:Alumina_Therm')
OOF.Material.Remove_property(name='Spinel_Material',
property='Thermal:Conductivity:Isotropic:Spinel_Therm')
OOF.Property.Parametrize.Thermal.Conductivity.Isotropic.Spinel_Therm(kappa=10.425414997138)
OOF.Material.Add_property(name='Spinel_Material', property='Thermal:Conductivity:Isotropic:Spinel_Therm')
OOF.Material.Remove_property(name='Zirconia_Material',
property='Thermal:Conductivity:Isotropic:Zirconia_Therm')
OOF.Property.Parametrize.Thermal.Conductivity.Isotropic.Zirconia_Therm(kappa=2.94166666666666)
OOF.Material.Add_property(name='Zirconia_Material',
property='Thermal:Conductivity:Isotropic:Zirconia_Therm')
OOF.Material.Remove_property(name='Monazite_Material',
property='Thermal:Conductivity:Isotropic:Monazite_Therm')
OOF.Property.Parametrize.Thermal.Conductivity.Isotropic.Monazite_Therm(kappa=1.82467532467532)
OOF.Material.Add_property(name='Monazite_Material',
property='Thermal:Conductivity:Isotropic:Monazite_Therm')
OOF.Mesh.Boundary_Conditions.Edit(name='bc', mesh='3Y-ASM.png:skeleton:mesh',
condition=DirichletBC(field=Temperature,field_component='',equation=Heat_Eqn,eqn_component='',profile=Const
antProfile(value=295.0),boundary='top'))
```

```
OOF.Mesh.Boundary_Conditions.Edit(name='bc<2>', mesh='3Y-ASM.png:skeleton:mesh',
condition=DirichletBC(field=Temperature,field_component='',equation=Heat_Eqn,eqn_component='',profile=Const
antProfile(value=305.0),boundary='bottom'))
OOF.Mesh.Solve(mesh='3Y-ASM.png:skeleton:mesh', endtime=0.0)
OOF.Mesh.Analyze.Integral(mesh='3Y-ASM.png:skeleton:mesh', time=latest,
data=getOutput('Flux:Invariant',invariant=Magnitude(),flux=Heat_Flux),
domain=SkeletonEdgeBoundaryDomain(boundary='top',side='LEFT'),
sampling=StatElementSegmentSampleSet(n_points=25),
destination=OutputStream(filename='/data/users/jangle/3Y-ASM_Z_1_inter_300C',mode='w'))
OOF.Material.Remove_property(name='Alumina_Material',
property='Thermal:Conductivity:Isotropic:Alumina_Therm')
OOF.Property.Parametrize.Thermal.Conductivity.Isotropic.Alumina_Therm(kappa=13.384599223625)
OOF.Material.Add_property(name='Alumina_Material',
property='Thermal:Conductivity:Isotropic:Alumina_Therm')
OOF.Material.Remove_property(name='Spinel_Material',
property='Thermal:Conductivity:Isotropic:Spinel_Therm')
OOF.Property.Parametrize.Thermal.Conductivity.Isotropic.Spinel_Therm(kappa=9.07695390781563)
OOF.Material.Add_property(name='Spinel_Material', property='Thermal:Conductivity:Isotropic:Spinel_Therm')
OOF.Material.Remove_property(name='Zirconia_Material',
property='Thermal:Conductivity:Isotropic:Zirconia_Therm')
OOF.Property.Parametrize.Thermal.Conductivity.Isotropic.Zirconia_Therm(kappa=2.79166666666666)
OOF.Material.Add_property(name='Zirconia_Material',
property='Thermal:Conductivity:Isotropic:Zirconia_Therm')
OOF.Material.Remove_property(name='Monazite_Material',
property='Thermal:Conductivity:Isotropic:Monazite_Therm')
OOF.Property.Parametrize.Thermal.Conductivity.Isotropic.Monazite_Therm(kappa=1.64285714285714)
OOF.Material.Add_property(name='Monazite_Material',
property='Thermal:Conductivity:Isotropic:Monazite_Therm')
OOF.Mesh.Boundary_Conditions.Edit(name='bc', mesh='3Y-ASM.png:skeleton:mesh',
condition=DirichletBC(field=Temperature,field_component='',equation=Heat_Eqn,eqn_component='',profile=Const
antProfile(value=395.0),boundary='top'))
OOF.Mesh.Boundary_Conditions.Edit(name='bc<2>', mesh='3Y-ASM.png:skeleton:mesh',
condition=DirichletBC(field=Temperature,field_component='',equation=Heat_Eqn,eqn_component='',profile=Const
antProfile(value=405.0),boundary='bottom'))
OOF.Mesh.Solve(mesh='3Y-ASM.png:skeleton:mesh', endtime=0.0)
OOF.Mesh.Analyze.Integral(mesh='3Y-ASM.png:skeleton:mesh', time=latest,
data=getOutput('Flux:Invariant',invariant=Magnitude(),flux=Heat_Flux),
domain=SkeletonEdgeBoundaryDomain(boundary='top',side='LEFT'),
sampling=StatElementSegmentSampleSet(n_points=25),
destination=OutputStream(filename='/data/users/jangle/3Y-ASM_Z_1_inter_400C',mode='w'))
OOF.Material.Remove_property(name='Alumina_Material',
property='Thermal:Conductivity:Isotropic:Alumina_Therm')
OOF.Property.Parametrize.Thermal.Conductivity.Isotropic.Alumina_Therm(kappa=11.411641945269)
OOF.Material.Add_property(name='Alumina_Material',
property='Thermal:Conductivity:Isotropic:Alumina_Therm')
OOF.Material.Remove_property(name='Spinel_Material',
property='Thermal:Conductivity:Isotropic:Spinel_Therm')
OOF.Property.Parametrize.Thermal.Conductivity.Isotropic.Spinel_Therm(kappa=8.02761692650334)
OOF.Material.Add_property(name='Spinel_Material', property='Thermal:Conductivity:Isotropic:Spinel_Therm')
OOF.Material.Remove_property(name='Zirconia_Material',
property='Thermal:Conductivity:Isotropic:Zirconia_Therm')
OOF.Property.Parametrize.Thermal.Conductivity.Isotropic.Zirconia_Therm(kappa=2.70833333333333)
OOF.Material.Add_property(name='Zirconia_Material',
property='Thermal:Conductivity:Isotropic:Zirconia_Therm')
OOF.Material.Remove_property(name='Monazite_Material',
property='Thermal:Conductivity:Isotropic:Monazite_Therm')
```

```
OOF.Property.Parametrize.Thermal.Conductivity.Isotropic.Monazite_Therm(kappa=1.5)
OOF.Material.Add_property(name='Monazite_Material',
property='Thermal:Conductivity:Isotropic:Monazite_Therm')
OOF.Mesh.Boundary_Conditions.Edit(name='bc', mesh='3Y-ASM.png:skeleton:mesh',
condition=DirichletBC(field=Temperature,field_component='',equation=Heat_Eqn,eqn_component='',profile=Const
antProfile(value=495.0),boundary='top'))
OOF.Mesh.Boundary_Conditions.Edit(name='bc<2>', mesh='3Y-ASM.png:skeleton:mesh',
condition=DirichletBC(field=Temperature,field_component='',equation=Heat_Eqn,eqn_component='',profile=Const
antProfile(value=505.0),boundary='bottom'))
OOF.Mesh.Solve(mesh='3Y-ASM.png:skeleton:mesh', endtime=0.0)
OOF.Mesh.Analyze.Integral(mesh='3Y-ASM.png:skeleton:mesh', time=latest,
data=getOutput('Flux:Invariant',invariant=Magnitude(),flux=Heat_Flux),
domain=SkeletonEdgeBoundaryDomain(boundary='top',side='LEFT'),
sampling=StatElementSegmentSampleSet(n_points=25),
destination=OutputStream(filename='/data/users/jangle/3Y-ASM_Z_1_inter_500C',mode='w'))
OOF.Material.Remove_property(name='Alumina_Material',
property='Thermal:Conductivity:Isotropic:Alumina_Therm')
OOF.Property.Parametrize.Thermal.Conductivity.Isotropic.Alumina_Therm(kappa=9.99546872309267)
OOF.Material.Add_property(name='Alumina_Material',
property='Thermal:Conductivity:Isotropic:Alumina_Therm')
OOF.Material.Remove_property(name='Spinel_Material',
property='Thermal:Conductivity:Isotropic:Spinel_Therm')
OOF.Property.Parametrize.Thermal.Conductivity.Isotropic.Spinel_Therm(kappa=7.1878107457899)
OOF.Material.Add_property(name='Spinel_Material', property='Thermal:Conductivity:Isotropic:Spinel_Therm')
OOF.Material.Remove_property(name='Zirconia_Material',
property='Thermal:Conductivity:Isotropic:Zirconia_Therm')
OOF.Property.Parametrize.Thermal.Conductivity.Isotropic.Zirconia_Therm(kappa=2.64166666666666)
OOF.Material.Add_property(name='Zirconia_Material',
property='Thermal:Conductivity:Isotropic:Zirconia_Therm')
OOF.Material.Remove_property(name='Monazite_Material',
property='Thermal:Conductivity:Isotropic:Monazite_Therm')
OOF.Property.Parametrize.Thermal.Conductivity.Isotropic.Monazite_Therm(kappa=1.4090909090909)
OOF.Material.Add_property(name='Monazite_Material',
property='Thermal:Conductivity:Isotropic:Monazite_Therm')
OOF.Mesh.Boundary_Conditions.Edit(name='bc', mesh='3Y-ASM.png:skeleton:mesh',
condition=DirichletBC(field=Temperature,field_component='',equation=Heat_Eqn,eqn_component='',profile=Const
antProfile(value=595.0),boundary='top'))
OOF.Mesh.Boundary_Conditions.Edit(name='bc<2>', mesh='3Y-ASM.png:skeleton:mesh',
condition=DirichletBC(field=Temperature,field_component='',equation=Heat_Eqn,eqn_component='',profile=Const
antProfile(value=605.0),boundary='bottom'))
OOF.Mesh.Solve(mesh='3Y-ASM.png:skeleton:mesh', endtime=0.0)
OOF.Mesh.Analyze.Integral(mesh='3Y-ASM.png:skeleton:mesh', time=latest,
data=getOutput('Flux:Invariant',invariant=Magnitude(),flux=Heat_Flux),
domain=SkeletonEdgeBoundaryDomain(boundary='top',side='LEFT'),
sampling=StatElementSegmentSampleSet(n_points=25),
destination=OutputStream(filename='/data/users/jangle/3Y-ASM_Z_1_inter_600C',mode='w'))
OOF.Material.Remove_property(name='Alumina_Material',
property='Thermal:Conductivity:Isotropic:Alumina_Therm')
OOF.Property.Parametrize.Thermal.Conductivity.Isotropic.Alumina_Therm(kappa=8.96490901820976)
OOF.Material.Add_property(name='Alumina_Material',
property='Thermal:Conductivity:Isotropic:Alumina_Therm')
OOF.Material.Remove_property(name='Spinel_Material',
property='Thermal:Conductivity:Isotropic:Spinel_Therm')
OOF.Property.Parametrize.Thermal.Conductivity.Isotropic.Spinel_Therm(kappa=6.50047393364929)
OOF.Material.Add_property(name='Spinel_Material', property='Thermal:Conductivity:Isotropic:Spinel_Therm')
```

```
OOF.Material.Remove_property(name='Zirconia_Material',
property='Thermal:Conductivity:Isotropic:Zirconia_Therm')
OOF.Property.Parametrize.Thermal.Conductivity.Isotropic.Zirconia_Therm(kappa=2.55833333333333)
OOF.Material.Add_property(name='Zirconia_Material',
property='Thermal:Conductivity:Isotropic:Zirconia_Therm')
OOF.Material.Remove_property(name='Monazite_Material',
property='Thermal:Conductivity:Isotropic:Monazite_Therm')
OOF.Property.Parametrize.Thermal.Conductivity.Isotropic.Monazite_Therm(kappa=1.35064935064935)
OOF.Material.Add_property(name='Monazite_Material',
property='Thermal:Conductivity:Isotropic:Monazite_Therm')
OOF.Mesh.Boundary_Conditions.Edit(name='bc', mesh='3Y-ASM.png:skeleton:mesh',
condition=DirichletBC(field=Temperature,field_component='',equation=Heat_Eqn,eqn_component='',profile=Const
antProfile(value=695.0),boundary='top'))
OOF.Mesh.Boundary_Conditions.Edit(name='bc<2>', mesh='3Y-ASM.png:skeleton:mesh',
condition=DirichletBC(field=Temperature,field_component='',equation=Heat_Eqn,eqn_component='',profile=Const
antProfile(value=705.0),boundary='bottom'))
OOF.Mesh.Solve(mesh='3Y-ASM.png:skeleton:mesh', endtime=0.0)
OOF.Mesh.Analyze.Integral(mesh='3Y-ASM.png:skeleton:mesh', time=latest,
data=getOutput('Flux:Invariant',invariant=Magnitude(),flux=Heat_Flux),
domain=SkeletonEdgeBoundaryDomain(boundary='top',side='LEFT'),
sampling=StatElementSegmentSampleSet(n_points=25),
destination=OutputStream(filename='/data/users/jangle/3Y-ASM_Z_1_inter_700C',mode='w'))
OOF.Material.Remove_property(name='Alumina_Material',
property='Thermal:Conductivity:Isotropic:Alumina_Therm')
OOF.Property.Parametrize.Thermal.Conductivity.Isotropic.Alumina_Therm(kappa=8.20648215531756)
OOF.Material.Add_property(name='Alumina_Material',
property='Thermal:Conductivity:Isotropic:Alumina_Therm')
OOF.Material.Remove_property(name='Spinel_Material',
property='Thermal:Conductivity:Isotropic:Spinel_Therm')
OOF.Property.Parametrize.Thermal.Conductivity.Isotropic.Spinel_Therm(kappa=5.92754010695187)
OOF.Material.Add_property(name='Spinel_Material', property='Thermal:Conductivity:Isotropic:Spinel_Therm')
OOF.Material.Remove_property(name='Zirconia_Material',
property='Thermal:Conductivity:Isotropic:Zirconia_Therm')
OOF.Property.Parametrize.Thermal.Conductivity.Isotropic.Zirconia_Therm(kappa=2.44166666666666)
OOF.Material.Add_property(name='Zirconia_Material',
property='Thermal:Conductivity:Isotropic:Zirconia_Therm')
OOF.Material.Remove_property(name='Monazite_Material',
property='Thermal:Conductivity:Isotropic:Monazite_Therm')
OOF.Property.Parametrize.Thermal.Conductivity.Isotropic.Monazite_Therm(kappa=1.29870129870129)
OOF.Material.Add_property(name='Monazite_Material',
property='Thermal:Conductivity:Isotropic:Monazite_Therm')
OOF.Mesh.Boundary_Conditions.Edit(name='bc', mesh='3Y-ASM.png:skeleton:mesh',
condition=DirichletBC(field=Temperature,field_component='',equation=Heat_Eqn,eqn_component='',profile=Const
antProfile(value=795.0),boundary='top'))
OOF.Mesh.Boundary_Conditions.Edit(name='bc<2>', mesh='3Y-ASM.png:skeleton:mesh',
condition=DirichletBC(field=Temperature,field_component='',equation=Heat_Eqn,eqn_component='',profile=Const
antProfile(value=805.0),boundary='bottom'))
OOF.Mesh.Solve(mesh='3Y-ASM.png:skeleton:mesh', endtime=0.0)
OOF.Mesh.Analyze.Integral(mesh='3Y-ASM.png:skeleton:mesh', time=latest,
data=getOutput('Flux:Invariant',invariant=Magnitude(),flux=Heat_Flux),
domain=SkeletonEdgeBoundaryDomain(boundary='top',side='LEFT'),
sampling=StatElementSegmentSampleSet(n_points=25),
destination=OutputStream(filename='/data/users/jangle/3Y-ASM_Z_1_inter_800C',mode='w'))
OOF.Material.Remove_property(name='Alumina_Material',
property='Thermal:Conductivity:Isotropic:Alumina_Therm')
OOF.Property.Parametrize.Thermal.Conductivity.Isotropic.Alumina_Therm(kappa=7.64307268579348)
```

```
OOF.Material.Add_property(name='Alumina_Material',
property='Thermal:Conductivity:Isotropic:Alumina_Therm')
OOF.Material.Remove_property(name='Spinel_Material',
property='Thermal:Conductivity:Isotropic:Spinel_Therm')
OOF.Property.Parametrize.Thermal.Conductivity.Isotropic.Spinel_Therm(kappa=5.44264116013576)
OOF.Material.Add_property(name='Spinel_Material', property='Thermal:Conductivity:Isotropic:Spinel_Therm')
OOF.Material.Remove_property(name='Zirconia_Material',
property='Thermal:Conductivity:Isotropic:Zirconia_Therm')
OOF.Property.Parametrize.Thermal.Conductivity.Isotropic.Zirconia_Therm(kappa=2.40833333333333)
OOF.Material.Add_property(name='Zirconia_Material',
property='Thermal:Conductivity:Isotropic:Zirconia_Therm')
OOF.Material.Remove_property(name='Monazite_Material',
property='Thermal:Conductivity:Isotropic:Monazite_Therm')
OOF.Property.Parametrize.Thermal.Conductivity.Isotropic.Monazite_Therm(kappa=1.25974025974025)
OOF.Material.Add_property(name='Monazite_Material',
property='Thermal:Conductivity:Isotropic:Monazite_Therm')
OOF.Mesh.Boundary_Conditions.Edit(name='bc', mesh='3Y-ASM.png:skeleton:mesh',
condition=DirichletBC(field=Temperature,field_component='',equation=Heat_Eqn,eqn_component='',profile=Const
antProfile(value=895.0),boundary='top'))
OOF.Mesh.Boundary_Conditions.Edit(name='bc<2>', mesh='3Y-ASM.png:skeleton:mesh',
condition=DirichletBC(field=Temperature,field_component='',equation=Heat_Eqn,eqn_component='',profile=Const
antProfile(value=905.0),boundary='bottom'))
OOF.Mesh.Solve(mesh='3Y-ASM.png:skeleton:mesh', endtime=0.0)
OOF.Mesh.Analyze.Integral(mesh='3Y-ASM.png:skeleton:mesh', time=latest,
data=getOutput('Flux:Invariant',invariant=Magnitude(),flux=Heat_Flux),
domain=SkeletonEdgeBoundaryDomain(boundary='top',side='LEFT'),
sampling=StatElementSegmentSampleSet(n_points=25),
destination=OutputStream(filename='/data/users/jangle/3Y-ASM_Z_1_inter_900C',mode='w'))
OOF.Material.Remove_property(name='Alumina_Material',
property='Thermal:Conductivity:Isotropic:Alumina_Therm')
OOF.Property.Parametrize.Thermal.Conductivity.Isotropic.Alumina_Therm(kappa=7.22120709136832)
OOF.Material.Add_property(name='Alumina_Material',
property='Thermal:Conductivity:Isotropic:Alumina_Therm')
OOF.Material.Remove_property(name='Spinel_Material',
property='Thermal:Conductivity:Isotropic:Spinel_Therm')
OOF.Property.Parametrize.Thermal.Conductivity.Isotropic.Spinel_Therm(kappa=5.0269340974212)
OOF.Material.Add_property(name='Spinel_Material', property='Thermal:Conductivity:Isotropic:Spinel_Therm')
OOF.Material.Remove_property(name='Zirconia_Material',
property='Thermal:Conductivity:Isotropic:Zirconia_Therm')
OOF.Property.Parametrize.Thermal.Conductivity.Isotropic.Zirconia_Therm(kappa=2.35833333333333)
OOF.Material.Add_property(name='Zirconia_Material',
property='Thermal:Conductivity:Isotropic:Zirconia_Therm')
OOF.Material.Remove_property(name='Monazite_Material',
property='Thermal:Conductivity:Isotropic:Monazite_Therm')
OOF.Property.Parametrize.Thermal.Conductivity.Isotropic.Monazite_Therm(kappa=1.25974025974025)
OOF.Material.Add_property(name='Monazite_Material',
property='Thermal:Conductivity:Isotropic:Monazite_Therm')
OOF.Mesh.Boundary_Conditions.Edit(name='bc', mesh='3Y-ASM.png:skeleton:mesh',
condition=DirichletBC(field=Temperature,field_component='',equation=Heat_Eqn,eqn_component='',profile=Const
antProfile(value=995.0),boundary='top'))
OOF.Mesh.Boundary_Conditions.Edit(name='bc<2>', mesh='3Y-ASM.png:skeleton:mesh',
condition=DirichletBC(field=Temperature,field_component='',equation=Heat_Eqn,eqn_component='',profile=Const
antProfile(value=1005.0),boundary='bottom'))
OOF.Mesh.Solve(mesh='3Y-ASM.png:skeleton:mesh', endtime=0.0)
OOF.Mesh.Analyze.Integral(mesh='3Y-ASM.png:skeleton:mesh', time=latest,
data=getOutput('Flux:Invariant',invariant=Magnitude(),flux=Heat_Flux),
```

```
domain=SkeletonEdgeBoundaryDomain(boundary='top',side='LEFT'),
sampling=StatElementSegmentSampleSet(n_points=25),
destination=OutputStream(filename='/data/users/jangle/3Y-ASM_Z_1_inter_1000C',mode='w'))
```